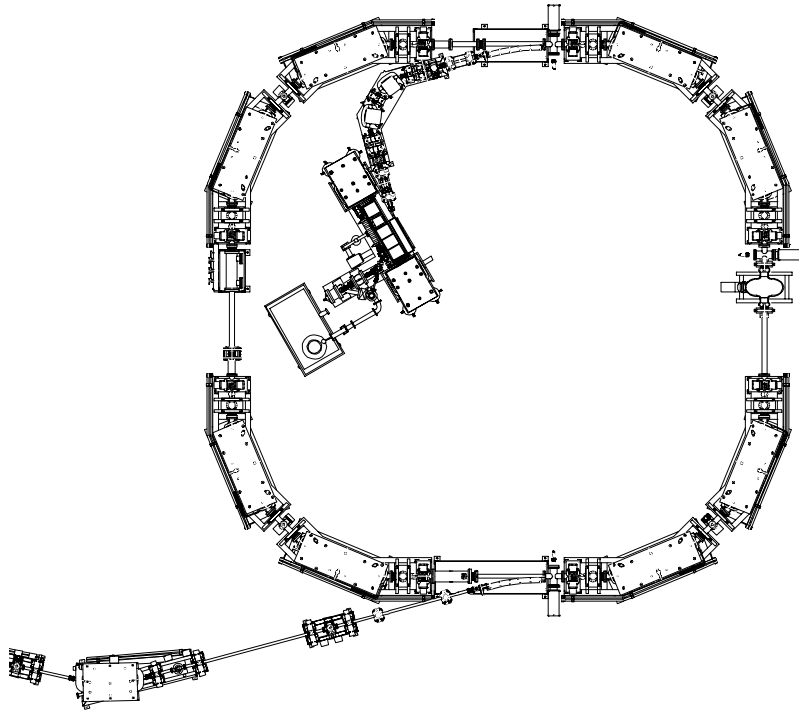


Investigations of the ANKA Injector: Lattice, Beam Properties and Performance



Lars Præstegaard

Danfysik A/S
Jyllinge, Denmark

Institute for Storage Ring Facilities
University of Aarhus, Denmark

April 2001

Preface

This thesis is submitted to the Faculty of Science at the University of Aarhus, Denmark to fulfill the requirements for the Ph.D. degree. The thesis is the product of a joint industrial Ph.D. project between the company Danfysik A/S and the Institute for Storage Ring Facilities at the University of Aarhus (ISA) concerning the design and characterization of the injector for the Ångström Karlsruhe (ANKA) synchrotron radiation source at Forschungszentrum Karlsruhe, Germany. The injector consists of a 500-MeV booster synchrotron, a 53-MeV racetrack microtron, and associated transfer lines.

The first chapter of the thesis puts the ANKA injector into the context of the significant development in the application of synchrotron radiation in the last decade, which has initiated the construction of numerous synchrotron radiation sources world-wide. In chapter 2, the racetrack microtron is described theoretically with emphasis on longitudinal dynamics, transverse dynamics, and the interaction between the beam and the accelerating structure. Chapter 3 provides a theoretical account of the booster synchrotron, in particular, the injection process of the racetrack microtron beam in the booster synchrotron and the subsequent capture of the beam by the rf system. In chapter 4, the experimental investigation of the racetrack microtron is presented with the main focus on a characterization of the output beam because the quality of the output beam is essential for the multi-turn injection efficiency of the booster synchrotron. In addition, the observed properties of the output beam are compared with the results of the theoretical discussion in chapter 2 and the beam properties of other racetrack microtrons and linear accelerators. Finally, chapter 5 is devoted to a detailed experimental investigation of the booster synchrotron. The chapter begins with a study of the lattice parameters of the booster synchrotron, providing information about the deviations from the ideal lattice. Next, the beam properties of the circulating beam are characterized throughout the entire one-second cycle of the injector and compared with both the theoretical investigation in chapter 3 and the performance of other booster synchrotrons. In addition, the injection and extraction processes are examined in detail. These experimental results are used to examine where and why beam loss do occur, providing valuable information about how to improve the performance of the injector.

Throughout the Ph.D. project, I have received excellent support from my two supervisors Søren Pape Møller and Bjarne Roger Nielsen. Søren has been a great assistance during my training in accelerator physics, and has been a pleasant working partner during the commissioning of both the racetrack microtron and the booster synchrotron. Bjarne has been helpful with information about Danfysik relating to the commercial aspects of the Ph.D. project. I also appreciate the competent assistance of the employees of Danfysik and ISA during the commissioning of the ANKA injector, in particular, Niels Hertel, Jørgen S. Nielsen, and Povl Abrahamsen. Besides, I would like to thank Ulrik Vindelev Pedersen for his pleasant company in our office, and for his and Jørgen's proofreading of this thesis. A

Preface

sincere thanks also goes to the staff at Forschungszentrum Karlsruhe, in particular, Montse Pont, Francisco Pérez, Erhard Huttel, and Dieter Einfeld for their invaluable help during the commissioning of the ANKA injector and during the two and a half weeks in May-June 2000 when I performed all measurements presented in this thesis. Finally, I am deeply grateful for the support of my wife Betina, especially during the long stays in Karlsruhe.

During the Ph.D. project, I have contributed to the following scientific papers relating to the contents of the present thesis:

1. L. Præstegaard *et al.*, in Proc. European Part. Acc. Conf., Stockholm, 1998, p. 632
2. D. Einfeld *et al.*, in Proc. Part. Acc. Conf., New York, 1999, p. 2427
3. F. Pérez *et al.*, in Proc. European Part. Acc. Conf., Vienna, 2000, p. 1996
4. L. Præstegaard *et al.*, in Proc. European Part. Acc. Conf., Vienna, 2000, p. 678

Lars Præstegaard, April 2001

Contents

1. Introduction.....	1
2. The ANKA racetrack microtron	5
2.1 Introduction.....	5
2.2 The design of the ANKA racetrack microtron	6
2.2.1 General description of the racetrack microtron.....	6
2.2.2 Rf system	8
2.2.3 Diagnostics.....	9
2.3 Synchronous acceleration and phase stability	9
2.3.1 Theoretical description.....	9
2.3.2 Simulation of longitudinal dynamics	11
2.4 Transverse beam dynamics	14
2.5 Mechanisms limiting the beam current.....	17
2.5.1 Beam loading.....	17
2.5.2 Beam breakup.....	19
3. The ANKA booster synchrotron	21
3.1 Introduction.....	21
3.2 The design of the ANKA booster synchrotron	21
3.2.1 The booster synchrotron lattice.....	21
3.2.2 The rf system.....	25
3.2.3 Diagnostics.....	26
3.2.4 Closed orbit deviations.....	26
3.3 The multi-turn injection process	28
3.3.1 The injection transfer line.....	28
3.3.2 Simulations of the injection process	28
3.3.3 Capture efficiency of the rf system	33
3.3.4 Influence of beam loading on the injection process	35
3.4 Beam acceleration	38
3.4.1 The ramping scheme	38
3.4.2 Eddy current effects in the dipole magnet vacuum chamber	38
3.5 The extraction.....	40

Contents

3.5.1 The extraction process	40
3.5.2 The extraction transfer line	40
4. Experimental investigation of the ANKA racetrack microtron.....	43
4.1 Introduction	43
4.2 Beam current.....	43
4.2.1 Characterization of the current transformers.....	43
4.2.2 Beam current measurements	44
4.3 Momentum spread	46
4.4 Transverse emittances of electron beam	48
4.4.1 The extended variable quadrupole magnet method	48
4.4.2 Measurement of the transverse emittances by the extended variable quadrupole magnet method.....	49
4.4.3 Determination of the transverse emittances using synchrotron light	52
4.5 Investigation of the longitudinal dynamics.....	54
4.5.1 Dependence of the beam current on the generator power	54
4.5.2 Beam current oscillations.....	55
4.5.3 Variation of the momentum spread with the generator power	56
4.6 The performance of the ANKA racetrack microtron	58
4.6.1 Comparison with other racetrack microtrons	58
4.6.2 Comparison with the performance of linear accelerators.....	58
4.6.3 Improvements of the ANKA racetrack microtron.....	60
5. Experimental investigation of the ANKA booster synchrotron.....	63
5.1 Introduction	63
5.2 Investigation of the lattice of the booster synchrotron	63
5.2.1 Transverse tunes and lattice functions	63
5.2.2 Closed orbit deviations	67
5.2.3 Chromaticity	68
5.2.4 Momentum compaction factor	71
5.3 Properties of the electron beam	72
5.3.1 Beam current and lifetime.....	72
5.3.2 Bunch length	75
5.3.3 Momentum spread.....	77
5.3.4 Transverse emittances.....	78
5.4 The injection process.....	82
5.4.1 Investigation of the multi-turn injection scheme	82

Contents

5.4.2 Capture of the beam by the rf system.....	84
5.4.3 Analysis of large initial beam loss after injection	86
5.5 The extraction process.....	87
5.5.1 Investigation of the leak field of the extraction septum magnet	87
5.5.2 Beam behavior after the activation of the extraction kicker magnet	90
5.6 The properties of the extracted beam	92
5.6.1 Beam current and pulse length	92
5.6.2 Transverse emittances and momentum spread.....	93
5.7 Performance and improvements of the ANKA booster synchrotron.....	97
5.7.1 Comparison with other booster synchrotrons	97
5.7.2 Improvements of the lattice of the booster synchrotron	98
5.7.3 Improvements of the capture efficiency of the rf system	99
5.7.4 Improvements of the extraction process.....	101
6. Summary	103
Appendix A Detailed drawing of the ANKA injector	107
Appendix B Storage ring synchrotron radiation sources	109
Appendix C Lattice input files	113
C.1 Lattice input file of the ANKA racetrack microtron (OPTIM 2.0 format).....	113
C.2 Lattice input file of the ANKA booster synchrotron (OPTIM 2.0 format)	114
Appendix D Sextupole field of eddy currents in a rectangular vacuum chamber.....	117
D.1 Eddy current-induced field from top and bottom walls.....	117
D.2 Eddy current-induced field from sides of vacuum chamber	119
D.3 Sextupole strength of field produced by eddy currents	120
Appendix E Analysis of the synchrotron light imaging system.....	121
E.1 Waist of synchrotron light cone originating from a single electron.....	121
E.2 Blur of CCD image due to an extended source region	122

Chapter 1

Introduction

In the mid-1940s, it was discovered that a relativistic electron during deflection in a magnetic field emits intense broad band UV and X-ray radiation along the tangent of its trajectory, the so-called *synchrotron radiation*. For a modern electron accelerator, the intensity of the synchrotron radiation is many orders of magnitude more intense and much more directional than traditional x-ray sources. Therefore, synchrotron radiation has become an invaluable tool for diverse applications in surface physics, material science, chemistry, geophysics, molecular biology, medicine etc. For example, synchrotron radiation is the most important tool for identifying the structure and partly also the functioning of proteins on an atomic scale; a very active field of research owing to the recent decoding of the human genome.

Originally, the application of synchrotron radiation was a secondary activity at high-energy electron accelerators utilized for fundamental research in nuclear and particle physics. However, these machines are not optimized for the generation of synchrotron radiation. Therefore, owing to the increasing interest in the application of synchrotron radiation, research institutes all over the world have started to construct dedicated storage ring-based synchrotron radiation sources, fulfilling the specific requirements of a high quality synchrotron radiation beam. In particular, these accelerators have long straight sections allowing insertion of long periodic magnetic structures, called *undulators* or *wigglers*, which enhance the synchrotron radiation intensity per wavelength interval tremendously. With the excellent performance of these new highly specialized synchrotron radiation facilities, many new applications of synchrotron radiation have emerged, boosting the interest in synchrotron radiation even further. As a result, a large number of synchrotron radiation facilities are currently in the design phase or under construction world-wide, as shown in the table of storage ring synchrotron radiation sources in appendix B (18 sources are in the design phase and 13 sources are under construction in comparison with 45 sources already in operation).

The ANKA synchrotron radiation source which recently was brought into operation at Forschungszentrum Karlsruhe, Germany is a good example of the new generation of dedicated synchrotron radiation sources. The synchrotron radiation source includes a 2.5-GeV

storage ring synchrotron with a circumference of 110 m, in which intense synchrotron radiation is produced by a circulating electron beam, and tangential beam lines and monochromators for transport of the synchrotron radiation to the experimental setups [1]. The electrons in the storage ring are delivered by a 500-MeV electron injector, which is shown in figure 1.1. The main components of the injector are a 53-MeV racetrack microtron, a 500-MeV booster synchrotron, a transfer line between the racetrack microtron and the booster synchrotron, and a transfer line between the booster synchrotron and the storage ring [2].

In the autumn of 1997, the company Danfysik A/S was awarded the order for the complete ANKA injector. Although, Danfysik had a significant expertise of most of the single components of the injector, it was lacking knowledge of the design and the beam dynamics of a circular accelerator. Therefore, the company made an agreement with the Institute for Storage Ring Facilities, University of Aarhus (ISA) according to which ISA should provide Danfysik with the required know-how for the R&D and commissioning of the ANKA injector. An important part of the collaboration was the initiation of a joint industrial Ph.D. project concerning the design and characterization of the ANKA injector. The present thesis is the result of this Ph.D. project. The main objective of the thesis is to perform a detailed characterization of the lattices and the beam properties of the racetrack microtron and the booster synchrotron with emphasis on where and why beam loss occur. This information is used to propose how to improve the performance of the ANKA injector.

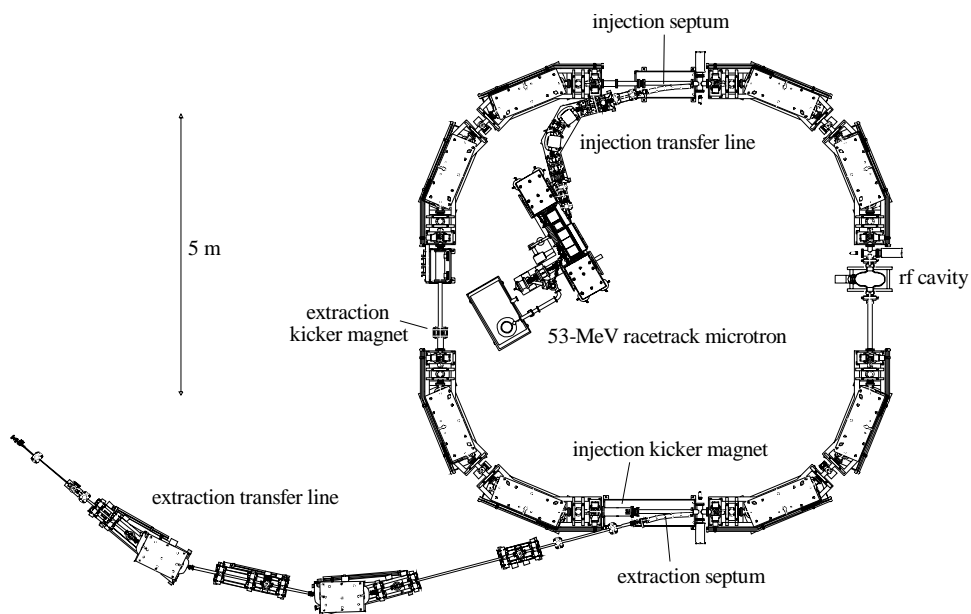


Figure 1.1: The ANKA injector (a detailed drawing of the injector is found in appendix A).

Introduction

References:

- [1] D. Einfeld *et al.*, in Proc. European Part. Acc. Conf., Barcelona, 1996, p. 641
- [2] L. Præstegaard *et al.*, in Proc. European Part. Acc. Conf., Stockholm, 1998, p. 632

Chapter 2

The ANKA racetrack microtron

2.1 Introduction

Since the 1970s, the nuclear physics community has strongly demanded high intensity electron beams in the range of 50 MeV to 2 GeV with high energy resolution because such beams are excellent electromagnetic probes of nuclear structure. Furthermore, nuclear physics researchers wish to perform coincidence measurements of the scattered electron and a possible fragment. To achieve this, a high duty factor electron beam is favorable since the number of unwanted accidental coincidences is proportional to the number of incident electrons squared while the number of real coincidences only is proportional to the number of incident electrons [1]. A synchrotron cannot provide the required beam properties as its injection-extraction cycle results in a rather low duty factor. Linacs are also not appropriate due to their poor energy resolution and their extensive size, even for electron energies well below 1 GeV.

Accelerator physicists have proposed two different schemes for obtaining the desired beam properties. The first is to employ the synchrotron as a pulse stretcher by extracting the beam at a constant rate between two successive injections from a low energy and low duty factor electron accelerator. The slow extraction is usually achieved by exciting the beam by means of a third order betatron resonance [2]. Secondly, and in this context more relevant, the demanded beam properties can be realized by recirculating the electron beam multiple times through the same linac via an external arrangement of magnets [3]. This is a much more economical scheme than the conventional linac because the size of the machine is much smaller and the same rf voltage accelerates the beam multiple times, making the conversion of rf power into beam power very efficient. Most recirculating accelerators are so-called *racetrack microtrons* which are defined as recirculating accelerators for which all recirculating orbits pass through the same arrangement of constant field magnets. The most popular racetrack microtron is the *two-magnet racetrack microtron* or *standard racetrack microtron* which consists of one linac and two 180° dipole magnets for recirculation of the

beam through the linac. This is a rather flexible design which offers considerable freedom for optimization of the accelerator for specific experimental requirements^a. In addition, the recirculation produces an electron beam with very high energy resolution. As a consequence, the racetrack microtron became a popular tool for nuclear physics research in the 1970s and 1980s [2,4]. Besides, owing to the high quality beam properties of the racetrack microtron, it has also found applications as an injector for electron synchrotrons^b, a generator for free-electron lasers [5,6], a generator of ultra-short x-ray pulses [7], and as a tool for radiation treatment [8,9]. For most of these more recent applications, the racetrack microtron is operated in a pulsed mode, yielding intense electron pulses with a typical duration of one microsecond.

Danfysik has chosen a pulsed 53-MeV racetrack microtron as injector for the 500-MeV ANKA booster synchrotron because the racetrack microtron is relatively cheap, compact, and offers beam characteristics which are ideal for injection into the booster synchrotron. In addition, the components of the racetrack microtron fit much better with the product range of Danfysik than the components of a linac. Finally, it has been important for the choice of injector that Danfysik collaborates with the Institute for Storage Ring Facilities, University of Aarhus which utilizes a 100-MeV racetrack microtron as injector for the storage ring ASTRID [10].

2.2 The design of the ANKA racetrack microtron

2.2.1 General description of the racetrack microtron

A schematic of the 53-MeV ANKA racetrack microtron is presented in figure 2.1 and its main parameters are listed in table 2.1. The accelerator is very similar to the 100-MeV racetrack microtron which was installed at the University of Aarhus in 1990 [10]. The only significant difference is the lower final energy of the ANKA racetrack microtron owing to fewer recirculations.

The electron gun of the ANKA racetrack microtron is of the standard spherical-pierce type with a BaO cathode, providing up to ~500 mA of electrons at 70 keV in a 4 μ s long pulse. After passing a 500-MHz electrostatic chopper, the electron beam is focused by two solenoids and subsequently deflected onto the linac axis by an achromatic bending, consisting of two 45° dipole magnets and a horizontally-focusing quadrupole magnet. Following the passage of an additional focusing solenoid at the entrance of the linac, the electrons pass

^aFor convenience, 'racetrack microtron' refers to the two-magnet racetrack microtron in the remainder of the thesis.

^bExamples of synchrotron light facilities which uses racetrack microtrons as injectors are found in table 5.1.

The ANKA racetrack microtron

through the linac with an energy gain of 5.3 MeV in both directions. Subsequently, the electron beam is recycled by two 180° solid core C-type dipole magnets with a field strength of

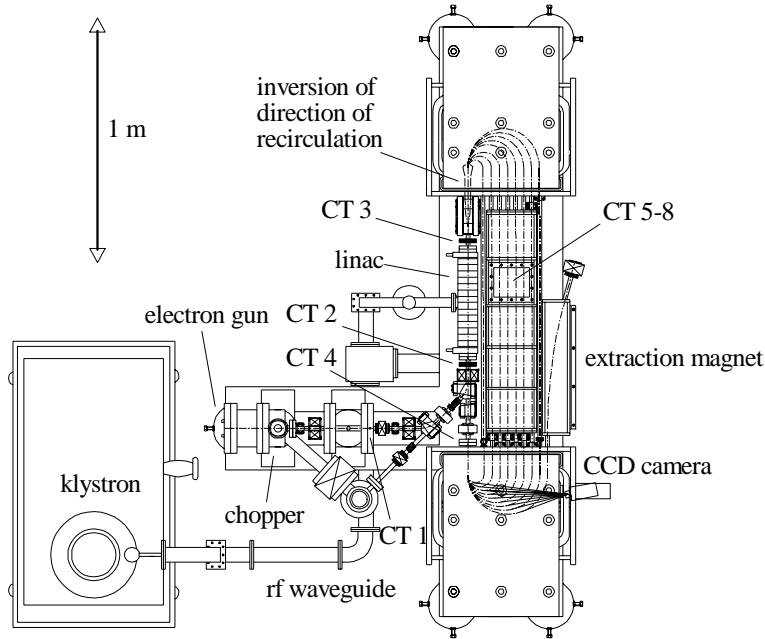


Figure 2.1: Schematic of the ANKA racetrack microtron.

Table 2.1: Design and achieved parameters of the ANKA racetrack microtron.

		Design	Achieved
180° dipole magnets	Field strength	1.12 T	1.12 T
Injection	Injection energy	70 keV	56 keV
	Electron gun current	~500 mA	~400 mA
Acceleration	Rf frequency	2.9986 GHz	2.9979 GHz
	Energy gain	5.3 MeV	5.3 MeV
	Number of linac passages	10	10
Output beam	Electron energy	53 MeV	53 MeV
	Average pulse current	10 mA	16 mA
	Pulse length	0.5-1 μ s	0-1.6 μ s
	Repetition rate	0-10 Hz	0-10 Hz
	Relative momentum spread	<0.003	0.0011 \pm 0.0001
	Horizontal emittance	0.2 mm mrad	0.21 \pm 0.08 mm
	Vertical emittance	0.2 mm mrad	0.21 \pm 0.05 mm

1.12 T, providing electron orbits with the characteristic racetrack geometry. In the fringe field of the dipole magnets, reverse field clamps in a Babic-Sedlacek configuration are introduced, and a 0.1-mm thick foil in the back of each dipole magnet produces a small field gradient of about 4 G/cm with decreasing field strength towards the back of the dipole magnets. Furthermore, a horizontally-focusing quadrupole magnet on the linac axis ensures horizontal beam stability and ten window frame x/y corrector magnets have been installed in the machine for correction of non-ideal alignment of magnets, imperfections in the magnet homogeneity and magnetic stray fields.

After the first passage of the linac, the electron speed differs from the speed of light by 0.5 percent. This is enough to induce a severe phase slip between the electrons and the linac field at the second passage of the linac if the electrons are recirculated in a racetrack orbit. The problem is solved by inverting the direction of recirculation after the first linac passage by means of the 180° dipole magnet and two small dipole magnets following the linac as indicated by the small loop of the beam trajectory in figure 2.1 [11]. With this modification, a proper adjustment of the linac position will eliminate the phase slip at the second linac passage without interfering with the synchronous conditions of the subsequent racetrack orbits. In addition, the change of the direction of recirculation has the advantage that the first real racetrack orbit is sufficiently far away from the linac axis to clear the linac. After two passages of the linac, the velocity of the electrons is sufficiently close to the speed of light that no further phase-slip correction is needed. Finally, after ten passages of the linac, the 53-MeV electron beam is extracted by a 15° bending magnet.

2.2.2 Rf system

The linac is of the Los Alamos side-coupled type with seven cavities, two half cavities in each end of the linac, and eight coupling cavities [12]. The half cavities improve the acceptance of the low energy electrons from the gun because the distance between the centers of the first two cavities is reduced. The acceleration is achieved by a $\pi/2$ standing wave mode with a resonant frequency of 2.9979 GHz, permitting acceleration in both directions with an energy gain of 5.3 MeV. The $\pi/2$ mode has been selected because its field profile is less sensitive to tuning errors than the other modes.

First, the rf wave is generated by a combined 3-GHz oscillator and amplifier which produce a 1-kW rf pulse with a duration of 0-10 μ s. After passing a variable attenuator, the rf pulse is amplified by a 6-MW klystron and transmitted to the linac via a rectangular waveguide. At the same time, a 10-Hz pulse-modulated 30-kV high-voltage supply generates a 4 μ s long pulse with an amplitude of -26.5 kV. The pulse is sent to a pulse transformer in an oil-filled tank below the klystron in which its amplitude is transformed up to -130 kV, and finally employed as acceleration voltage for the electron beam in the klystron. A separate bifilar winding of the pulse transformer supplies the electron gun with a 4 μ s long -56-kV high voltage pulse and filament power. Antennas in the waveguide makes it

possible to monitor the forward rf power from the klystron and the reflected rf power from the linac, whereas the rf power in the linac can be measured with an antenna in the linac.

2.2.3 Diagnostics

The eight beam current transformers are the most important diagnostic tools of the race-track microtron because they allow an absolute measurement of the temporal profile of the beam current throughout the entire recirculation (CT 1-8 in figure 2.1). Each current transformer has a very simple design consisting of a high permeability toroid with a copper winding (25 turns) and a bnc connector. In addition, three chromium-doped Al_2O_3 beam viewers monitoring the beam position, the beam profile, and the beam intensity are very helpful during the initial adjustment of the first few racetrack orbits. The image of each viewer is recorded by a CCD camera and the viewers can be moved in and out of the beam by pneumatically-operated actuators. Finally, the synchrotron light which is emitted from the beam in one of the 180° bends can be observed with a CCD camera (see figure 2.1). The image of the synchrotron light provides the relative orbit position, the beam intensity, and the beam profile.

2.3 Synchronous acceleration and phase stability

2.3.1 Theoretical description

Only electrons which have a certain phase, the *synchronous phase*, with respect to the crest of the rf field will acquire the nominal 5.3 MeV acceleration during the passage of the linac. All other electrons will gain different energies and will be lost during the following orbits. As a consequence, the beam will be divided into bunches with one rf wavelength separation. The synchronous energy gain of 5.3 MeV is therefore only obtained at a given linac passage if the duration of the previous recirculation is an integer number of rf periods. For the first racetrack orbit, this condition of synchronism is

$$\frac{2\pi R_2 + 2L}{\lambda_{rf} \beta_2} = \text{integer} , \quad (2.1)$$

where R_2 is the bending radius of the beam trajectory in the 180° dipole magnets after two linac passages, L is the distance between the 180° dipole magnets, λ_{rf} is the rf wavelength, and β_2 is the relativistic β parameter after two linac passages. In order to obtain synchronous acceleration in the following racetrack orbits, the recirculation period should be an integral number ν of rf periods longer than the previous orbit, resulting in the following condition of synchronism [3^{p. 59}]:

$$\frac{\Delta E}{m_0 c^2} \frac{B_c}{B_0} + \frac{2L}{\lambda_{rf}} \left(\frac{1}{\beta_{n+1}} - \frac{1}{\beta_n} \right) = \nu \quad , \quad 2 \leq n \leq 10 \quad . \quad (2.2)$$

Chapter 2

Here $\Delta E = \Delta E_0 \cos \phi_s$ is the synchronous energy gain of the linac, ϕ_s is the synchronous phase, $\Delta E_0/e$ is the amplitude of the linac voltage, m_0 is the rest mass of the electron, $B_c = 2\pi m_0 c / (e \lambda_{rf})$ is the cyclotron field, and B_0 is the field strength of the 180° dipole magnets. Denoting the electron energy after n passages of the linac, $E_n = \Delta E(n+i)$, where $i\Delta E$ is the injection energy, one obtains

$$\frac{2\pi R_n}{\lambda_{rf}} = \frac{E_n}{m_0 c^2} \frac{B_c}{B_0} = \nu(n+i) \quad , \quad 2 \leq n \leq 10 \quad , \quad (2.3)$$

where it has been employed that $\Delta E/m_0 c^2 \gg 1$. In case of the ANKA racetrack microtron, one has $E_{10} = 53$ MeV and $R_{10} = 160$ mm, yielding $B_0 = 1.12$ T and $\nu = 1$ according to (2.3). The parameter ν has been chosen to unity because this choice gives the best longitudinal stability (see equation (2.7) below), less stringent mechanical tolerances, the most compact linac structure, and a more convenient rf frequency in terms of the commercially available klystrons.

According to (2.3), an electron with an excess energy of δE follows a racetrack orbit with a longer path length, leading to an increase of the phase of the electron relative to a synchronous particle during the next passage of the linac. More precisely, it follows from (2.3) that the relationship between phase and energy excess of an electron with respect to a synchronous particle is

$$\delta \phi_{n+1} = \delta \phi_n + 2\pi \nu \frac{\delta E_n}{\Delta E} \quad (2.4)$$

$$\delta E_{n+1} = \delta E_n + \Delta E_0 \cos(\phi_s + \delta \phi_s) - \Delta E_0 \cos \phi_s \quad , \quad (2.5)$$

where $\delta \phi_n$ and δE_n are the phase and energy excess relative to a synchronous particle immediately after the n^{th} passage of the linac [3^{p. 117}]. Assuming $\delta \phi \ll \phi_s$, equation (2.4) and (2.5) can to first order in $\delta \phi_n$ and δE_n be summarized by the matrix equation [3^{p. 117}]:

$$\begin{pmatrix} \delta \phi_{n+1} \\ \delta E_{n+1} \end{pmatrix} = \begin{pmatrix} 1 & 2\pi \nu / \Delta E \\ -\Delta E \tan \phi_s & 1 - 2\pi \nu \tan \phi_s \end{pmatrix} \begin{pmatrix} \delta \phi_n \\ \delta E_n \end{pmatrix} \quad , \quad 2 \leq n \leq 9 \quad . \quad (2.6)$$

Hence, $\delta \phi_n$ and δE_n trace out an ellipse in $(\delta \phi, \delta E)$ space throughout the recirculation with a phase advance per racetrack orbit, χ , given by $\cos \chi = 1 - \pi \nu \tan \phi_s$ [3^{p. 118}]. Stability of the phase motion requires that the absolute value of the trace of the matrix in (2.6) is smaller than 2, resulting in the stability criteria

$$0 < \pi \nu \tan \phi_s < 2 \quad . \quad (2.7)$$

The beam of the ANKA racetrack microtron is thus performing stable phase motion for $0 < \phi_s < 32.48^\circ$. However, although ϕ_s is within the stable interval, the region of phase space

in which stable phase motion occurs is restricted due to non-linear perturbations and coupling between the longitudinal and the transverse motion in the real racetrack microtron lattice, resulting in unstable phase motion for large values of $\delta\phi_n$ and δE_n . From the rms value of $\delta\phi$, the relative energy spread of the electron beam at full energy can be estimated:

$$\frac{\delta E_{10,rms}}{E_{10}} \approx \left(\cos \phi_s - \cos(\delta\phi_s + \delta\phi_{10,rms}) \right) \frac{\Delta E_0}{E_{10}}, \quad (2.8)$$

where $\phi_{10,rms}$ and $\delta E_{10,rms}$ are the rms values of $\delta\phi_{10}$ and δE_{10} . Assuming $\phi_s=19^\circ$ and $\delta\phi_{10,rms} \sim 5^\circ$ for the ANKA racetrack microtron, one obtains a relative energy spread of ~ 0.003 at full energy. The inverse dependence of the relative energy spread on energy in (2.8) is a consequence of the fixed shape of a particular ellipse in $(\delta\phi, \delta E)$ space for all recirculations.

2.3.2 Simulation of longitudinal dynamics

In order to investigate the longitudinal dynamics in greater detail, the phase and energy excess of an electron (with respect to a synchronous particle) immediately after the last passage of the linac, $\delta\phi_{10}$ and δE_{10} , have been calculated for various initial values of $\delta\phi_2$ and δE_2 using (2.4) and (2.5) (the initial values cannot be chosen prior to the second pas-

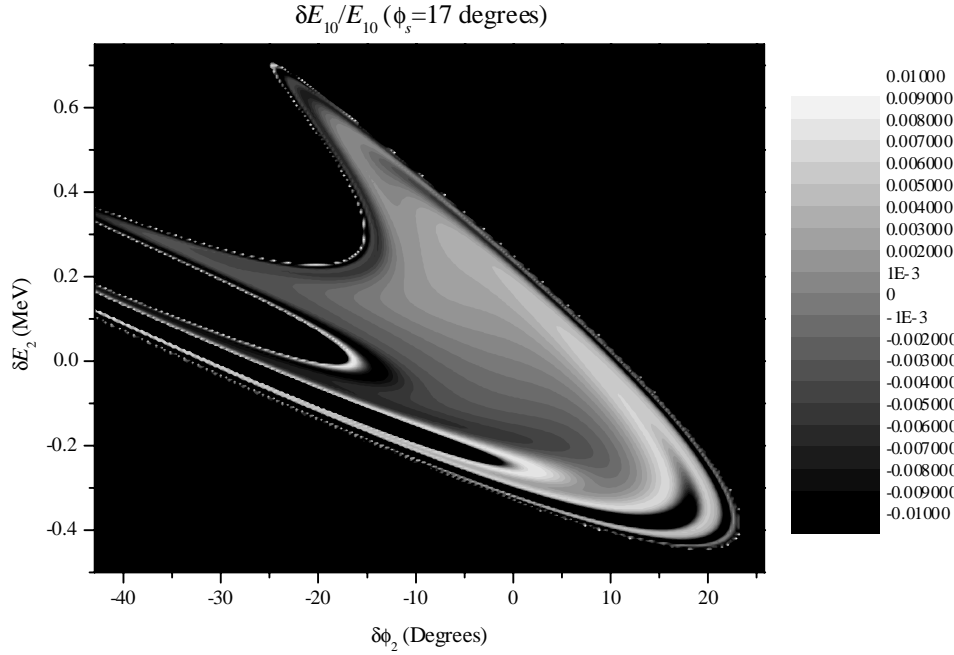


Figure 2.2: Relative energy excess with respect to the synchronous energy at full energy.

sage of the linac due to the change of the direction of circulation). For example, the relative electron energy excess, $\delta E_{10}/E_{10}$, for a wide range of $\delta\phi_2$ and δE_2 values is presented in figure 2.2 for a synchronous angle of 17° . The figure clearly demonstrates the rather complex dependence of the phase space variables at full energy on the initial phase space variables at low energy. It is observed that the energy spread of the electron beam is smallest for initial values of $\delta\phi_2$ and δE_2 near -5° and 0.05 MeV, respectively. In practice, the values of $\delta\phi_2$ and δE_2 can be optimized by changing the position of the linac.

In order to obtain a better understanding of the energy distribution of the output beam of the racetrack microtron, all the $\delta E_{10}/E_{10}$ values in figure 2.2 are projected into a histogram, revealing a narrow peak of electrons in the vicinity of the synchronous energy. The peak structure is attributed to those electrons which are caught in the longitudinal bucket. Assuming that all initial values associated with electrons in the peak are equally populated and no electrons in the peak are lost during the beam transport, the total number of electrons in the longitudinal bucket at full energy is proportional to the area of the peak. Hence, an evaluation of the area of the peak readily yields the variation of the output beam current as a function of the synchronous phase ϕ_s , which is plotted in figure 2.3. As expected, the beam current (or number of electrons in the longitudinal bucket) has a maximum for $\phi_s \approx 19^\circ$ in the middle of the interval which provides stable phase motion. On the contrary, the maxi-

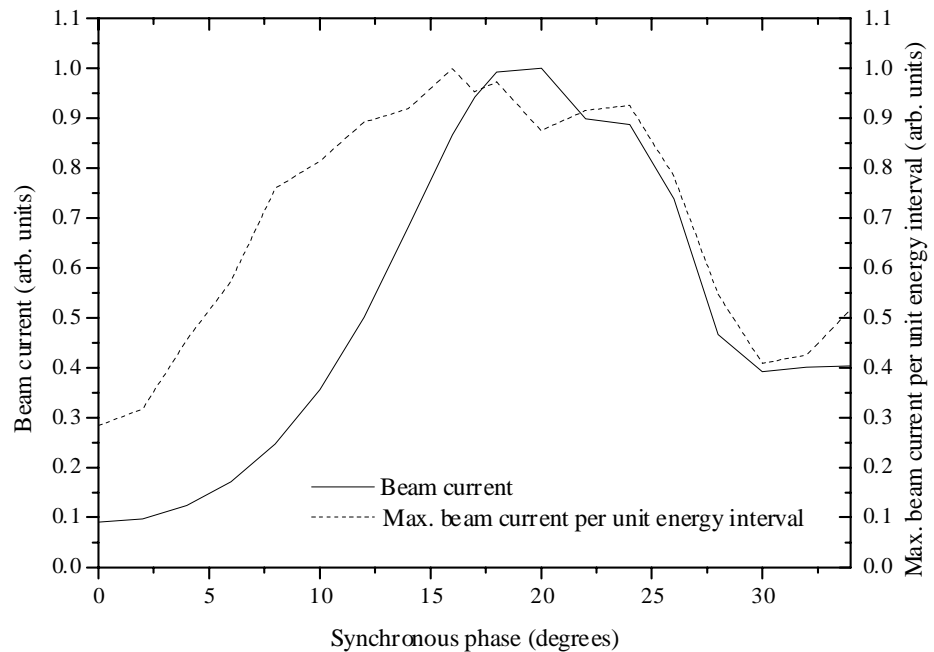


Figure 2.3: Beam current at full energy as a function of the synchronous phase. The graph also indicates the variation of the maximum beam current per unit energy interval at full energy.

imum beam current per unit energy interval almost is constant down to a synchronous phase of 10 degrees since the decline of the beam current is balanced by a decline of the energy spread.

The shape of the peak also provides the energy distribution of the electron beam at full energy (if the assumptions above are valid). The found relative energy spread as a function of ϕ_s is shown in figure 2.4, demonstrating a reasonable agreement with the result found above using (2.8). The observed increase of the relative energy spread as a function of ϕ_s is attributed to the fact that close to $\phi_s=0$ (the crest of the rf field), the increment of δE is constrained from above by

$$\Delta E_0(1 - \cos \phi_s) \approx \frac{1}{2} \Delta E_0 \phi_s^2 . \quad (2.9)$$

However, the relative energy spread increases slightly below $\phi_s=10^\circ$ due to a long tail of electrons to the low-energy side of the peak, associated with electrons which are not captured in the longitudinal bucket. Finally, the position of the peak also provides the change of the center electron energy as a function of ϕ_s presented in figure 2.4. It is noticed that the center electron energy has a rather modest dependence on the synchronous phase.

The discussion above provides a good qualitative insight into the longitudinal dyna-

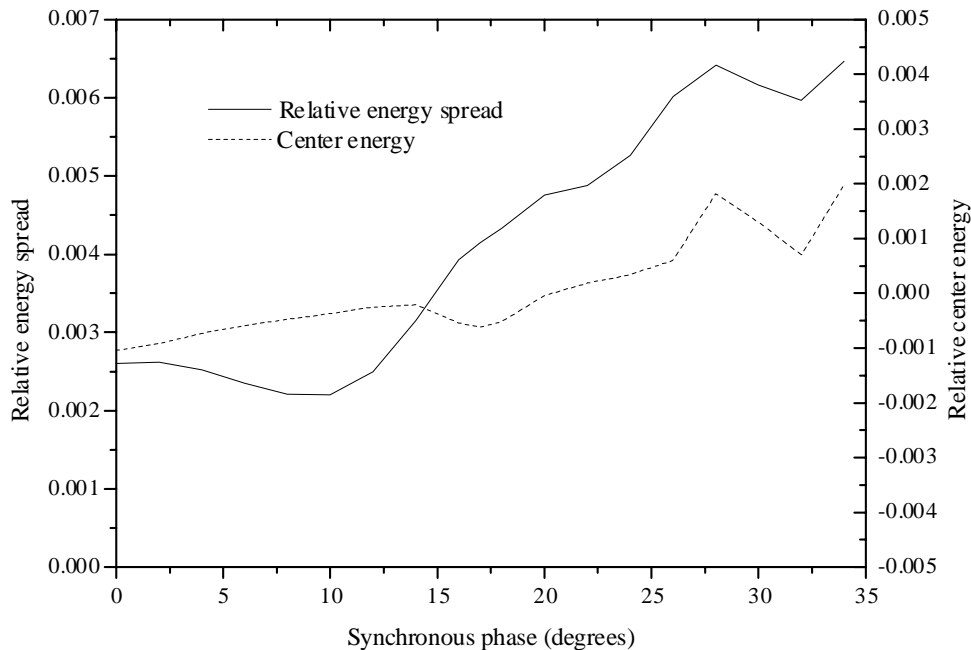


Figure 2.4: Relative energy spread (one standard deviation) and center energy of the electron beam at full energy versus the synchronous phase ϕ_s .

mics. However, an accurate quantitative knowledge of the longitudinal properties requires a detailed knowledge of the linac fields, a field mapping of the 180° dipole magnets, and a full tracking of the electrons in the accelerator, including both the longitudinal and transverse degrees of freedom.

2.4 Transverse beam dynamics

Originally, the most severe problem of the racetrack microtron design was the vertical defocusing due to the fringe fields of the 180° dipole magnets, having a focal length, $f_{y,fringe}$, given by

$$\frac{1}{f_{y,fringe}} = \frac{1}{R^2} \left[- \int_{fringe\ field} \frac{B}{B_0} \left(1 - \frac{B}{B_0} \right) ds + \int_{fringe\ field} \frac{2y^2}{3} \left(\frac{dB/ds}{B_0} \right)^2 ds + \dots \right], \quad (2.10)$$

where the integration is along the linac axis in the fringe field region, R is the bending radius of the beam trajectory in the homogeneous region of the 180° dipole magnets, B is the field strength of the 180° dipole magnets in the fringe field region, B_0 is the field strength of the 180° dipole magnets in the homogeneous region, and y is the vertical deviation from the median plane of the 180° dipole magnets [13]. It appears that especially for the first few orbits, the fringe field is a problem because the defocusing focal length is of the same magnitude as the bending radius. The difficulty was solved by Babic and Sedlacek in 1967 by introducing field clamps with a field direction opposite to that of the 180° dipole magnets in the fringe field region, canceling the first term in (2.10) for all energies [14]. In addition, this scheme results in racetrack orbits which resemble those of a hard edge field model, thus satisfying the conditions of synchronism. Due to the cancellation, the action of the fringe field is determined by the second term in (2.10) which provides vertical focusing of second order as the term is proportional to y squared. The focal strength of this term decreases unfortunately quadratically with energy, making it only effective at low energy. It cannot be allowed to increase the excitation of the reverse field for more vertical focusing at high energy since this would result in a too short focal length at low energy. Instead, vertical focusing at high energy is provided by a gradient of the dipole field (~ 4 G/cm) of the 180° dipole magnets (the field strength decreases towards the back of the dipole magnets), providing a vertically-focusing quadrupole field [15,16]. The gradient does not affect the horizontal focusing because a horizontal displacement of the beam at the entrance of the 180° dipole magnet simply yields a shift of the entire trajectory inside the dipole magnet. However, the gradient should be kept small since it gradually increases the synchronous phase. Assuming a hard edge model of the dipole field, the vertical focusing strength of the gradient corresponds to a lens with a focal length of

$$\frac{1}{f_{y,gradient}} = \frac{1}{B_0 R} \int_0^{\pi R} \frac{dB_y}{dx} ds = \frac{1}{B_0} \int_0^{\pi} g \sin \theta d\theta = \frac{2g}{B_0} = 14 \text{ m}^{-1}, \quad (2.11)$$

where g is the gradient of dipole field. Hence, the gradient focusing is ideally independent of energy and therefore dominates at high energy. At low energy, however, the electrons are bent in the fringe region of the 180° dipole magnets with a gradient of the opposite sign of that in the homogenous region, resulting in a defocusing effect for the first three racetrack orbits. Finally, the horizontal focusing is provided by a horizontally-focusing quadrupole magnet on the linac axis.

To avoid over-focusing at low energy, the focal length in both the horizontal and vertical planes are much longer than the race track orbit, at least at high energy. Hence, the behavior of the lattice functions can be understood qualitatively by representing a single racetrack orbit by a drift space, a thin lens, and a drift space. Both drift spaces have a length of half of the racetrack orbit and the thin lens represents the effective focusing of all focusing elements. Assuming that the lattice functions only vary slowly from one racetrack orbit to the next, a single racetrack orbit can be considered as a closed lattice, and the lattice functions can be determined by identifying the simple transfer matrix of the racetrack orbit with the Twiss parameter transfer matrix [17]:

$$\begin{pmatrix} 1 & C/2 \\ 0 & 1 \end{pmatrix} \begin{pmatrix} 1 & 0 \\ -1/f & 1 \end{pmatrix} \begin{pmatrix} 1 & C/2 \\ 0 & 1 \end{pmatrix} = \begin{pmatrix} 1-C/2 & C-C^2/4f \\ -1/f & 1-Cf/2 \end{pmatrix} = \begin{pmatrix} \cos \mu & \beta \sin \mu \\ \sin \mu/\beta & \cos \mu \end{pmatrix}, \quad (2.12)$$

where C is the circumference of the racetrack orbit, f is the focal length of the thin lens, β is the beta function, and μ is the phase advance of the racetrack orbit. Solving the equation for $f \gg C$, one obtains

$$\mu = \sqrt{C/f} \quad \text{and} \quad \beta = \sqrt{Cf}. \quad (2.13)$$

The focal strength of the horizontally-focusing quadrupole magnet decreases linearly with energy. The horizontal phase advance of the racetrack orbit is thus expected to decrease as $E^{-1/2}$ whereas the horizontal beta function is expected to increase as $E^{1/2}$, where E is the electron energy. In contrast, the vertical focusing is energy independent (at least at high energy), resulting in rather moderate changes of the vertical phase advance and beta function with energy.

An accurate calculation of the lattice functions requires a tracking of the individual electron trajectories which takes the actual fringe fields into account. However, assuming that the fringe field-induced reduction of the vertical focusing of the dipole field gradient is balanced by the fringe field focusing at low energy, the overall vertical focusing is given by the ideal focusing of the dipole field gradient (hard edge model). Thus, the vertical focusing can be approximated by three only vertically-focusing thin lenses in each of the 180° dipole

magnets at a deflection angle of 30° , 90° and 150° . Integrating the ideal dipole field gradient in a $\pm 30^\circ$ interval around each thin lens, the inverse vertical focal lengths of the three thin lenses are found to be $g/(2B_g)$, $g/(B_g)$, and $g/(2B_g)$, respectively. With this simplification, the lattice functions of the ANKA racetrack microtron can be determined by means of a traditional lattice program with hard edge dipole magnets. The resulting lattice functions are shown in figure 2.5 (the lattice input file is provided in appendix C), demonstrating a good overall agreement with the simple lattice calculation above. However, the characteristic narrow minima of the horizontal betatron functions in the center of the 180° dipole magnets due to geometrical focusing are not revealed by the simple calculation. The initial parameters of β_x , $d\beta_x/ds$, β_y , and $d\beta_y/ds$ in figure 2.5 have been chosen as those which give the smallest and most uniform envelope of β_x and β_y since this choice corresponds to a well-optimized racetrack microtron with a minimum of beam loss during the beam transport. Any other choice of initial parameters leads to larger and oscillating beta functions. Hence, the condition of a well-optimized racetrack microtron provides a unique set of initial parameters, just as periodicity yields a unique set of initial parameters in a closed lattice. Furthermore, the initial parameters for the horizontal dispersion are $D_x=0$ m and $dD_x/ds=0$ because this choice leads to zero dispersion on the linac axis, which is preferable because the accelerating field decreases for a large transverse displacement from the linac

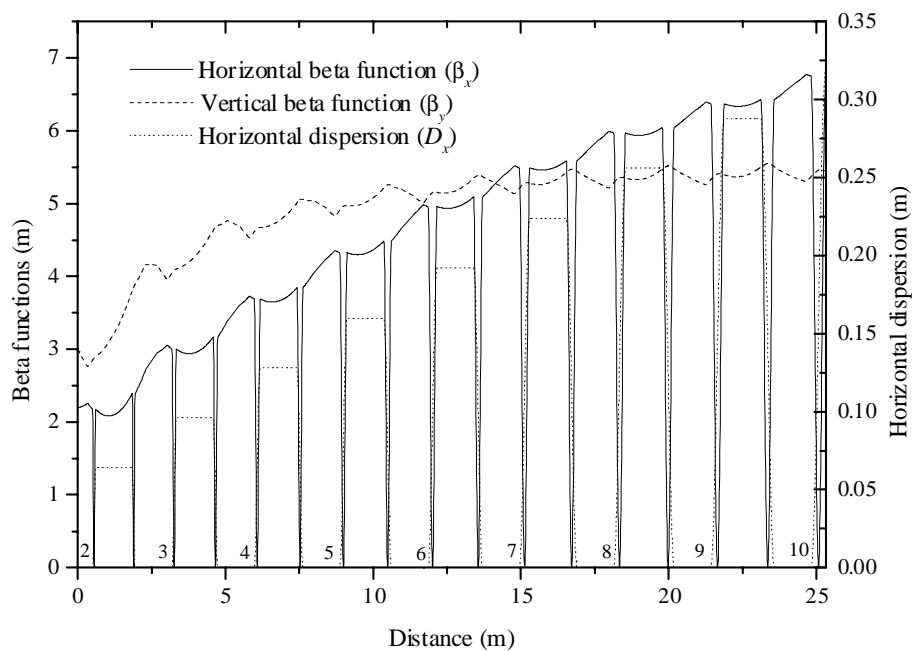


Figure 2.5: Lattice functions of the ANKA racetrack microtron after the second passage of the linac. The number of linac passages are indicated below the lattice functions.

axis.

The periodic form of the lattice functions in figure 2.5 and the slow variation of the envelope of the lattice functions suggest that each racetrack orbit to a good approximation can be considered as a closed lattice, confirming the assumption of the simple lattice calculation above. According to the lattice calculation in figure 2.5, the horizontal and vertical tunes of the of the racetrack orbit are $Q_x=0.171$, $Q_y=0.128$ and $Q_x=0.062$, $Q_y=0.100$ for the first and last racetrack orbits, respectively. Again in good qualitative agreement with the simple model above. The proximity to the $Q=0$ betatron resonance reveals a high sensitivity to dipole perturbations in terms of inhomogeneous dipole fields, alignment errors, and stray fields. This is the reason why corrector magnets have been installed in all racetrack orbits. Fortunately, integer resonances are not as harmful as in a circular accelerator due to the adiabatic damping and the small number of revolutions.

2.5 Mechanisms limiting the beam current

2.5.1 Beam loading

The presence of an intense electron beam in a cavity structure induces a significant voltage. This phenomenon, called *beam loading*, may impose restrictions on the maximum obtainable beam current because the beam-induced voltage perturb the accelerating rf voltage. If the rf frequency and the resonant frequency of the cavity structure coincides, the amplitude of the induced voltage is

$$V_{br} = \frac{2R_s I_b}{1 + \kappa} \exp\left(-\frac{\omega_{cav}^2 \sigma_s^2}{2c^2}\right), \quad (2.14)$$

where I_b is the average beam current of all beam recirculations, R_s is the shunt impedance of the cavity structure, κ is coupling coefficient between the rf waveguide and the cavity structure, ω_{cav} is the resonant angular frequency of the cavity structure, and σ_s is the Gaussian bunch length [18]. In case of the linac of the ANKA racetrack microtron for which $I_b \sim 300$ mA, $R_s = 18$ M Ω and $\kappa = 3.0$, the induced voltage is $I_b R_s / (1 + \kappa) \sim 1.4$ MV at resonance, using the electron bunches are much shorter than the rf wave length. Hence, the beam-induced field has a magnitude comparable to the accelerating field of the linac, clearly demonstrating the importance of beam loading. Taking into account the effect of beam loading, the required rf generator power in steady state to sustain an energy gain of $\Delta E = \Delta E_0 \cos \phi_s$ is

$$P_g = \frac{1}{\cos(\phi_L)^2} \frac{(1 + \kappa)^2}{8\kappa R_s} (\Delta E_0 / e + V_{br} \cos \phi_s)^2, \quad (2.15)$$

where ϕ_L is the loading angle describing the phase difference between the generator-in-

duced voltage at resonance and the cavity voltage [18]. Utilizing that σ_s is much shorter than the rf wave length and assuming an optimum tuning angle ($\phi_L=0$) for which the linac appears purely resistive to the rf generator, one finds from (2.15) that the generator power-limited maximum beam current of all recirculations is 825 mA for the ANKA racetrack microtron ($\phi_s=19^\circ$, $\Delta E=5.3$ MeV, $R_s=18$ M Ω , $P_g=6$ MW, and $\kappa=3$).

For an optimum tuning angle, there exist one choice of the coupling parameter κ ,

$$\kappa_{opt} = 1 + \frac{2R_s I_b}{\Delta E_0 / e} \cos \phi_s , \quad (2.16)$$

for which there is no reflected rf power from the linac [18]. According to (2.16), an increase of the beam current gives rise to a better matching of the waveguide and linac for $\kappa > \kappa_{opt}$. Hence, the beam-induced decline of the rf power in the linac is counteracted by an enhanced power transfer to the linac as a result of the improved matching. As a consequence, for $\kappa > \kappa_{opt}$ there exists a negative feedback mechanism which attempts to keep the linac field at a constant value in presence of any beam current fluctuation. The same is true for rf power fluctuations in the linac since the rf power is intimately linked to the beam current via the longitudinal acceptance. An abrupt change of the beam current or rf power thus induces damped oscillations of the beam current and rf power in the linac for $\kappa > \kappa_{opt}$. For $\kappa < \kappa_{opt}$ the situation is reversed to a positive feedback mechanism: the matching is enhanced if the beam current decreases, leading to a higher linac voltage which results in a reduced longitudinal acceptance and accordingly further beam current decline etc. As a consequence, the longitudinal dynamics is unstable for $\kappa < \kappa_{opt}$.

The characteristic time scale for building up the instability is partly given by the time constant of the linac as this quantity determines the time scale for correcting the rf power level after a change of the waveguide-linac matching. For the ANKA racetrack microtron, the 1/e time constant of the linac field is $2Q/(\omega_{rf}(1+\kappa))=0.29$ μ s, where Q is the quality factor of the linac and ω_{rf} is the angular rf frequency. In addition, the instability is governed by the time scale for developing beam losses after a change of the longitudinal acceptance resulting from a modification of the linac voltage. The time constant for appearance of beam loss is approximately given by half of the total recirculation time of ~ 50 ns. However, the combined build-up time of the instability is expected to be only about 100 ns as rather small changes of the linac voltage change the longitudinal acceptance considerably. Therefore, the build-up time is significantly smaller than the duration of the microtron pulse, suggesting that the total beam current through the linac of the ANKA racetrack microtron is limited by the constraint $\kappa \geq \kappa_{opt}$. According to (2.16), the corresponding maximum beam current is 329 mA for the parameters $\phi_s=19^\circ$, $\Delta E=5.3$ MeV, $R_s=18$ M Ω and $\kappa=3$. Ideally a total beam current of 329 mA corresponds to an output beam current of 31 mA for the 10 beam passages of the linac, but in practice significant beam loss at low energy is expected to reduce the output beam current significantly below 31 mA.

2.5.2 Beam breakup

The interaction between the beam and the electromagnetic field of the accelerating structure may also lead to an amplification of transverse modes which can be harmful for the beam, the so-called *regenerative beam breakup* [3^{chap. 9},19]. The mechanism of regenerative beam breakup is the following: A beam, initially on axis, is deflected in the accelerating structure by the transverse magnetic field of a HEM₁₁ mode, a mode with mixed TM₁₁ and TE₁₁ properties due to small deviations of the cavities from the simple cylindrical geometry. The deflection results in a displacement of the beam during the next passage of the accelerating structure which causes a transfer of energy into the HEM₁₁ mode, via interaction with its longitudinal electrical field component, provided the relative phase of the beam modulation and the HEM₁₁ field is appropriate. If the exchange of energy to the HEM₁₁ mode exceeds its resistive loss in the accelerating structure, the amplitude of the HEM₁₁ mode will increase exponentially until beam loss occur. The time constant of the exponential growth is $2Q_L/\omega$, where Q_L is the loaded quality factor of the HEM₁₁ mode and ω is the angular frequency of the HEM₁₁ mode [3^{chap. 9}].

It can be shown that the threshold current for regenerative beam breakup by a particular HEM₁₁ mode approximately is given by

$$I_{bbu} = \frac{E_{inj}}{KQ_L} \left(\sum_{s=2}^N \sum_{r=1}^{s-1} (R_{12})_{rs} \left(\frac{E_{inj}}{E_{inj} + (r-1)\Delta E} \right) \sin(\psi_{s-1} - \psi_{r-1}) \right)^{-1}, \quad (2.17)$$

where $K=eF_1^2/(4\lambda\epsilon_0c)$, F_1 can be calculated from a detailed knowledge of the HEM₁₁ mode, E_{inj} is the energy of the injected beam in the center of the first cavity, N is the number of passages of the accelerating structure, $(R_{12})_{rs}$ is the transport matrix from the r^{th} to the s^{th} passage of the accelerating structure, and ψ_{j-1} is the accumulated phase of the HEM₁₁ mode from the first to the j^{th} passage of the accelerating structure [3^{p. 177},19]. It follows that the threshold is a rather complex function of the recirculating lattice elements and the properties of the transverse HEM₁₁ mode. Unfortunately, the threshold cannot be calculated for the ANKA racetrack microtron since no information about HEM₁₁ modes of the linac is available. A detailed knowledge of the HEM₁₁ modes is essential as only a small shift of the frequency of the HEM₁₁ mode may change the threshold dramatically due to the dependence on the accumulated phase in (2.17). However, equation (2.17) show that the threshold for regenerative beam breakup can be increased by choosing a high injection energy and by designing a beam recirculation with small $(R_{12})_{rs}$ entries in the transport matrix. Actually, the simple transport matrix for one racetrack orbit in (2.12) shows that the ANKA racetrack microtron has small $(R_{12})_{rs}$ matrix entries owing to the long transverse focal length. This is a general property of racetrack microtrons with small transverse tunes.

References:

- [1] H. A. Grunder, B. K. Hartline, and S. T. Corneliussen, *Electron Accelerators for Research at the Frontiers of Nuclear Physics*, AIP Conf. Proc. **161**, p. 100 (1987)
- [2] M. Eriksson, Nucl. Instr. and Meth. **196**, p. 331 (1982)
- [3] R. E. Rand, *Recirculating Electron Accelerators*, Harwood Academic Publishers, London, 1984
- [4] H. Herminghaus *et al.*, Nucl. Instr. and Meth. **138**, p. 1 (1976)
- [5] A. A. Alimov *et al.*, Nucl. Instr. and Meth. **B139**, p. 511 (1998)
- [6] G. J. Ernst *et al.*, Infrared Phys. and Tech. **36**, p. 81 (1995)
- [7] T. Hori, J. Yang, and M. Washio, in Proc. European Part. Acc. Conf., Stockholm, 1998, p. 517
- [8] P. G. Archer *et al.*, Medical Dosimetry **24**, p. 13 (1999)
- [9] M. Karlsson, H. Nyström, and H. Svensson, Medical Physics **19**, p. 307 (1992)
- [10] S. P. Møller, in Proc. Part. Acc. Conf., San Francisco, 1991, p. 2811
- [11] R. Alvinsson and M. Eriksson, Report TRITA-EPP-76-07/LUSY-7601, Royal Institute of Technology, Stockholm, 1976
- [12] E. A. Knapp, B. C. Knapp, and J. M. Potter, Rev. Sci. Instrum. **39**, p. 979 (1968)
- [13] H. Herminghaus *et al.*, Nucl. Instr. and Meth. **138**, p. 1 (1976)
- [14] H. Babic and M. Sedlacek, Nucl. Instr. and Meth. **56**, p. 170 (1967)
- [15] M. Eriksson, Nucl. Instr. and Meth. **196**, p. 331 (1982)
- [16] M. Eriksson, Nucl. Instr. and Meth. **A261**, p. 39 (1987)
- [17] J. Rossbach and P. Schmüser, *Basic Course on Accelerator Optics*, in Proc. of Fifth General Accelerator Physics Course, CERN Accelerator School, Jyväskylä, Finland, 1992, edited by S. Turner (CERN, Geneva, 1994), p. 17
- [18] K. Akai, *Overview of RF Systems for Storage Rings and their Diagnostics*, in *Beam Measurement*, Proc. of the Joint US-CERN-Japan-Russia School on Particle Accelerators, edited by S-i. Kurokawa *et al.*, Montreux 1998 (World Scientific, Singapore, 1999), p. 378
- [19] C. M. Lyneis *et al.*, Nucl. Instr. and Meth. **204**, p. 269 (1983)

Chapter 3

The ANKA booster synchrotron

3.1 Introduction

The preliminary design of the ANKA booster synchrotron was performed in collaboration between Danfysik A/S, Forschungszentrum Karlsruhe, and the Institute for Storage Ring Facilities at the University of Aarhus (ISA) in the spring of 1997 following the invitation for tenders for the 500-MeV ANKA injector. From the very beginning, a synchrotron was chosen to bring the electron energy up to 500 MeV because linacs and racetrack microtrons for this energy are rather large and expensive. In addition, a synchrotron produces a beam with excellent beam properties as a result of the synchrotron light damping of the beam in the bending magnets. After Danfysik was awarded the order for the ANKA injector in August 1997, the design of the ANKA booster synchrotron was completed by Danfysik and ISA the following year.

3.2 The design of the ANKA booster synchrotron

3.2.1 The booster synchrotron lattice

The four-fold symmetric ANKA booster synchrotron is shown in figure 1.1 and a detailed drawing with component names is found in appendix A. In addition, the main design parameters of the booster synchrotron are presented in table 3.1. The booster synchrotron has eight 45° rectangular dipole magnets, defining a 26.4-m circumference with four short and four long straight sections. One family of eight horizontally-focusing quadrupole magnets is located symmetrically in each of the long straight sections while vertical focusing is provided by the fringe fields at the entrance and exit of the dipole magnets. The focusing properties of the fringe field can be represented by a thin lens with a focal length of

$$\frac{1}{f_{face}} = \frac{\tan(\theta/2)}{\rho} - \frac{gK(1 + \sin(\theta/2)^2)}{\rho^2 \cos(\theta/2)^3}, \quad K = \frac{1}{g} \int_{fringe\ field} \frac{B}{B_0} \left(1 - \frac{B}{B_0}\right) ds, \quad (3.1)$$

Chapter 3

Table 3.1: Design parameters and the corresponding achieved parameters of the ANKA booster synchrotron.

		Design	Achieved	
Lattice	Periodicity	4	4	
	Circumference	26.4 m	26.4 m	
	Revolution period	88 ns	88 ns	
	Bending field at 500 MeV	1.00 T	1.00 T	
	Rf frequency	499.65 MHz	499.65 MHz	
	Horizontal tune	1.775	1.83	
	Vertical tune	1.173	1.22	
	Horizontal chromaticity (53 MeV)	-0.3	2.27±0.17	
	Vertical chromaticity (53 MeV)	-2.7	-11±1	
	Momentum compaction factor	0.27	0.246±0.018	
	Max. booster energy	500 MeV	500 MeV	
	Repetition frequency	1 Hz	1 Hz	
	53 MeV beam	Circulating current	>15 mA	35 mA
	500 MeV beam	Circulating current	>7.5 mA	12 mA
Horizontal emittance		150 nm	165±22 nm	
Vertical emittance			2.3±0.8 nm	
Relative momentum spread		$3.4 \cdot 10^{-4}$	$(3.6 \pm 0.4) \cdot 10^{-4}$	
Extracted beam		Extracted current	>7.5 mA	9.5 mA
	Pulse length	56 ns	52 ns	
	Horizontal emittance	<200 nm	153±12 nm	
	Vertical emittance		11±2 nm	
	Relative momentum spread	<0.001	$(3.0 \pm 0.6) \cdot 10^{-4}$	

where ρ is the bending radius of the beam trajectory in the dipole magnets, θ is the bending angle of the dipole magnets, g is the height of the dipole magnet gap, and B and B_0 are the field strengths of the dipole magnets in the fringe field region and in the homogeneous region, respectively [1]. The defocusing second term in (3.1) is identical to the first term in (2.10) for a perpendicular entrance of the beam. For the parameters of the dipole magnets, $\rho=1.67$ m, $\theta=22.5^\circ$, $g=30$ mm, and $K=0.61$ (according to the field mapping of the dipole magnets), the vertical focal length is 4.2 m, and the first term in (3.1) dominates completely over the second term since $gK \ll \rho$. The resulting proportionality of f_{face} on ρ demonstrates that vertical edge focusing only is feasible in small synchrotrons, having dipole magnets with rather small bending radii. No sextupoles are included in the lattice for chromaticity correction because the natural chromaticities are not large enough to cause a serious tune

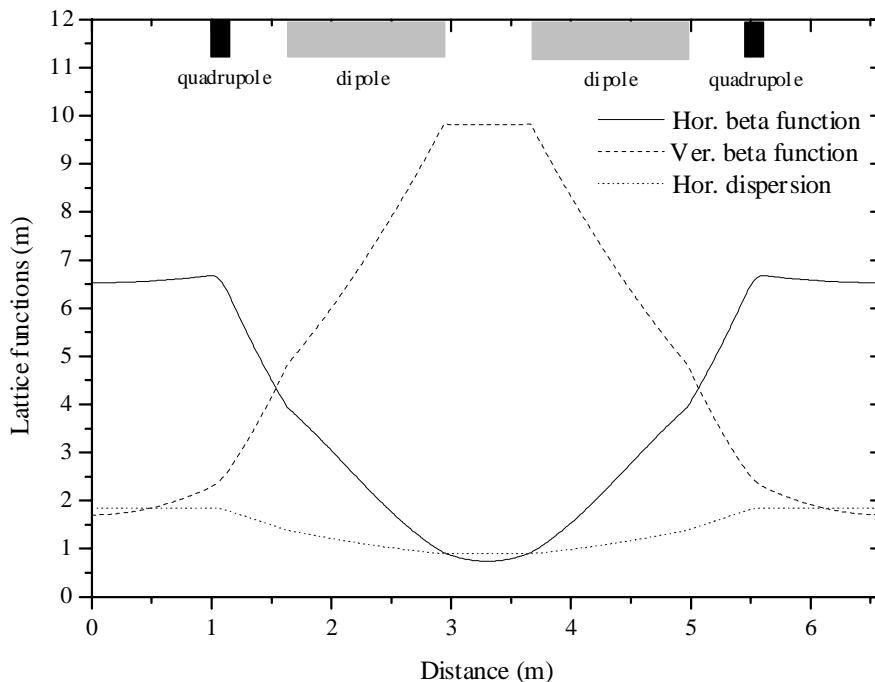


Figure 3.1: Beta and dispersion functions in one super-period of the lattice of the ANKA booster synchrotron (1/4 of the circumference).

spread. In addition, there is no need for positive chromaticities since operational experience at ISA suggests that the head-tail instability should not cause problems for beam currents below 40 mA. Finally, the booster synchrotron has four window frame x/y corrector magnets which can be ramped for correction of the closed orbit at all beam energies (these are not shown in figure A.1 since they were not foreseen in the original design).

The length of the long straight sections is selected with the aim of locating the horizontal and vertical betatron tunes, Q_x and Q_y , between the systematic resonances $3Q_x+2Q_y=8$ and $Q_x+2Q_y=4$. This choice of length also ensures clearance between the transfer lines and the nearby quadrupole magnets. For this working point one obtains $Q_x=1.775$ and $Q_y=1.216$, the horizontal and vertical chromaticities $\xi_x=-0.32$ and $\xi_y=-2.80$, a momentum compaction factor of 0.265, and the lattice functions shown in figure 3.1^a. A disadvantage of the lattice is the limited tune flexibility arising from only one family of quadrupole

^aThese lattice parameters deviate from the original design in table 3.1 because the actual properties of the magnetic elements and their actual position in the lattice are taken into account.

magnets, constraining the working point to a single curve in the tune diagram. If the lattice elements deviate from the design, it may therefore be difficult to avoid a resonance line in the tune diagram. In particular, if the resonance line is almost parallel with the working line, an adjustment of the horizontal quadrupole magnet will not move the working point away from the resonance. Hence, the limited tune flexibility calls for strict machining and alignment tolerances of the magnetic elements, requiring a detailed characterization of the magnetic elements in the production phase in order to verify the magnetic properties. For example, the vertical tune changes significantly even for small changes of the field boundary angle of the dipole magnets (a change of 1° results in a vertical tune shift of 0.13), giving rise to a tolerance of the effective field boundary angle of only $\sim 0.3^\circ$. Unfortunately, it is difficult to manufacture the field boundary angle with this high precision without a re-machining of the end-poles of the dipole magnets after a field mapping in an iterative process, making the production of the end-poles the most critical component of the lattice.

The vacuum system of the booster synchrotron consist of all-metal vacuum chambers with conflat flanges which is evacuated by 12 ion pumps distributed uniformly over the circumference. The capacity of each ion pumps is 75 liter/s, facilitating a vacuum level below 10^{-7} mbar, which is enough to achieve a residual gas-induced beam lifetime above one second. No bake-out of the vacuum system is thus required.

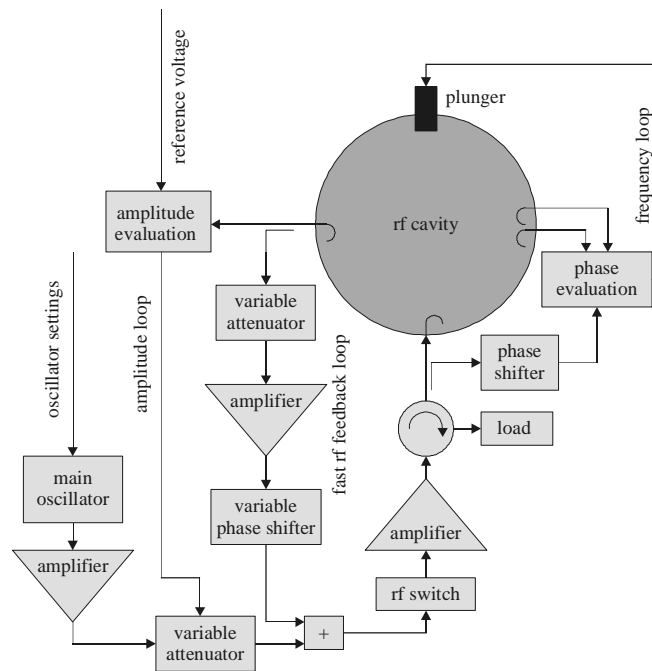


Figure 3.2: Block diagram of the booster synchrotron's rf system.

3.2.2 The rf system

The main features of the rf system of the booster synchrotron are presented in figure 3.2 (see ref. 2 for more details). The cavity is a single-cell bell-shaped cavity which was manufactured by Elettra in Trieste. The resonant frequency of the cavity is 499.65 MHz in order to produce a bunch structure of the beam which fits to the 499.65-MHz rf system of the ANKA storage ring. In addition, the cavity has a shunt impedance of 3.4 M Ω , an unloaded quality factor of 39500, and a coupling factor between the rf transmission line and the rf cavity of 1.04. The cavity is powered by a 200-W solid-state amplifier producing a maximum cavity voltage of 36 kV which is sufficient to achieve a good quantum life time at full energy and counteract the energy loss due to synchrotron radiation. In order to maintain a stable voltage in the cavity, a pickup signal from the cavity is compared with a reference voltage set by the control system, and the resulting error signal is utilized to control a variable attenuator which regulate the low level drive power. This is the so-called *amplitude loop*. In addition, the resonant frequency of the cavity is controlled by a *frequency loop* which compare two pickups signals from the cavity (180° out of phase) with a small fraction of the rf signal transmitted to the cavity. The error signal of the comparison is amplified and sent to the control unit of the plunger which controls the frequency and phase shift of the cavity. In case of interlocks due to a high cavity pressure, large cavity reflections etc, the rf switch will disable the rf power.

During the commissioning of the rf system, an additional *fast rf feedback loop* was installed in order to reduce the beam-induced voltage in the cavity [3,4]. The loop combines an amplified pickup signal from the cavity with the low-level drive signal coming from the main oscillator. The phase of the pickup signal is adjusted by means of a phase shifter in such a way that the two signals are 180° out of phase at the combiner. In this case, the voltage at the input of main the amplifier is given by

$$V_{in}^{loop} = V_{in} - e^{-i\Delta\omega T_{in}} \alpha V_{cav} , \quad (3.2)$$

where all actual voltages are the real part of the corresponding complex quantity, V_{in} is the voltage at the input of the main amplifier without fast rf feedback loop, $\Delta\omega$ is the angular frequency deviation from the resonant angular frequency ω_{cav} of the cavity, T_{in} is the transmission delay from the cavity to the input of the main amplifier, and α is the attenuation factor of the pickup signal relative to the cavity voltage V_{cav} . Assuming that $\Delta\omega \ll \omega_{cav}$, the cavity voltage with fast rf feedback becomes

$$V_{cav} = \frac{KV_{in} - V_b}{1 + 2iQ_L \Delta\omega/\omega_{cav} + e^{-i\Delta\omega T} \alpha K} , \quad (3.3)$$

where K is the amplification factor of the main amplifier, V_b is the beam-induced voltage in the cavity, $Q_L=Q/(1+\kappa)$ is the loaded quality factor of the cavity (κ is the coupling coeffi-

cient between the cavity and the transmission line), and T is the total delay of the loop (the delay of the cavity is not included) [5]. Hence, the effect of the fast rf feedback loop is to reduce the beam induced voltage by $1+\alpha K$ at resonance, equivalent to a similar reduction of the shunt impedance seen by the beam. Another consequence of the fast rf feedback loop is that the voltage of the low-level drive signal from the main oscillator, V_{in} , has to be increased by a factor $1+K\alpha$ in order to produce the same cavity voltage as without the loop. However, this is a minor disadvantage because the low-level drive power usually can be enhanced significantly for only a very moderate investment. According to the Nyquist criterion, the loop becomes unstable if the loop gain is larger than unity for a frequency component in the pickup signal with a phase shift, relative to the low level drive signal, which deviates more than $\sim 135^\circ$ from the nominal value of 180° [6]. As the cavity itself produces a phase shift of $\pm 90^\circ$ for even a very modest frequency shift, loop stability requires that the loop gain is less than unity for an additional phase shift of $T\Delta\omega = 45^\circ$, produced by the a frequency shift $\Delta\omega$ and the total loop delay T :

$$\text{loop gain} = \left| \frac{\alpha K}{1 + 2iQ_L \frac{1}{4} \pi / T\omega_{cav}} \right| \approx \left| \frac{2\alpha K}{Q_L \pi / T\omega_{cav}} \right| \leq 1 . \quad (3.4)$$

Hence, the finite delay of the fast rf feedback loop constrains αK below $Q_L/(4f_{cav}T)$.

3.2.3 Diagnostics

During the first roundtrip of the electron beam in the booster synchrotron, three chromium-doped Al_2O_3 beam viewers are employed for beam positioning and monitoring of the beam profile. The image of each viewer is recorded by a CCD camera and the viewers can be moved in and out of the beam by pneumatically-operated actuators. Subsequently, the beam current is monitored by the stripline units DSL_B.01 and DSL_B.02 (see figure A.1), each with four striplines, in order to complete the storage of the beam. Once the beam is stored in the booster synchrotron, a dc current transformer is employed for optimization of the circulating current since it provides the absolute beam current. In addition, the transverse position of the beam can be determined at eight positions by a unit of four button pickups. Finally, the beam position and the transverse profile of the circulating beam can be inferred from the synchrotron light extracted through windows in the vacuum chamber at two of the dipole magnets.

3.2.4 Closed orbit deviations

Field and length errors of the dipole magnets causes a horizontal displacement of the closed orbit in the booster synchrotron, the so-called *closed orbit deviation*, which is given by

$$x_{dev}(s) = \frac{\sqrt{\beta_x(s)}}{2\sin(\pi Q_x)} \sum_i \sqrt{\beta_{x,i}} K_i \cos(|\varphi_{x,i} - \varphi_x(s)| - \pi Q_x) , \quad K_i = \frac{\varepsilon_i L_d}{\rho} , \quad (3.5)$$

where

$$\varepsilon_i = \frac{1}{B_d L_d} \int_{dipole\ i} \Delta B_i ds \quad (3.6)$$

is the relative integrated field error of the i^{th} dipole magnet, $\beta_{x,i}$ is the value of the horizontal beta function at the i^{th} dipole magnet, $\varphi_x(s)$ is the horizontal betatron phase, $\varphi_{x,i}$ is the horizontal betatron phase at the i^{th} dipole magnet, ΔB_i is the absolute field error of the i^{th} dipole magnet, L_d is the effective length of the dipole magnets, and ρ is the bending radius of the beam trajectory in the dipole magnets [7^{p.} 230]. Assuming a Gaussian distribution of the relative integrated field errors with a standard deviation of σ_ε , an ensemble of random closed orbits can be calculated with the help of (3.5). According to the simulation of the multi-turn injection process in paragraph 3.3.2 below, a horizontal closed orbit deviation of 3 mm towards both the injection and extraction septa results in a ~25 percent reduction of the injected beam current. Hence, a reasonable requirement is that at maximum 10 percent of the orbits in the ensemble deviate more than 3 mm towards either of the septa, resulting in the tolerance: $\sigma_\varepsilon < 5 \cdot 10^{-4}$. Another class of dipole field errors arises from horizontal misalignment of the quadrupole magnets with a standard deviation of $\sigma_{\Delta x}$. In this case, the horizontal closed orbit deviation is given by (3.5) with $K_i = \Delta x_i k_q L_q$, where Δx_i is the horizontal misalignment error of the i^{th} quadrupole magnet, k_q is the quadrupole strength, and L_q is the effective length of the quadrupole magnets. With the same requirement to the injection efficiency as above, one obtains the tolerance: $\sigma_{\Delta x} < 0.5$ mm.

The vertical closed orbit deviation due to a vertical misalignment of the quadrupole magnets is given by the vertical analogue of (3.5) with $K_i = \Delta y_i k_q L_q$, where Δy_i is the vertical misalignment error of the i^{th} quadrupole magnet. In addition, rotational errors of the dipole magnets around the beam axis produces a vertical closed orbit deviation which is given by (3.5) with $K_i = L_d \Delta \theta_i / \rho$, where $\Delta \theta_i$ is the rotational error of the i^{th} dipole magnet. From the requirement that no more than 10 percent of the vertical closed orbits should deviate in excess of ± 10 mm from the design orbit, one obtains the following standard deviation of the tolerances of Δy and $\Delta \theta$: $\sigma_{\Delta y} < 0.6$ mm and $\sigma_{\Delta \theta} < 0.2$ mrad. The tolerance of the rotational error $\Delta \theta$ is rather strict for small rings with a small bending radius.

Actual measurements of the integrated field strength of the booster dipole magnets yield $\sigma_\varepsilon = 5.1 \cdot 10^{-4}$ and $\sigma_\varepsilon = 3.6 \cdot 10^{-4}$ for excitations of the magnets corresponding to 53 MeV and 500 MeV, respectively (average over trajectories with $x = -20$ mm, -10 mm, 0 mm, 10 mm, 20 mm). Since these values of σ_ε almost fulfil the requirement established above and magnets with low and large integrated field strengths are paired, the resulting closed orbit should not cause any problems.

3.3 The multi-turn injection process

3.3.1 The injection transfer line

The injection transfer line transports the 53-MeV electron beam from the racetrack microtron to the booster synchrotron and matches it to the lattice functions of the booster synchrotron. The design of the transfer line is shown in the drawing of the ANKA injector in figure A.1. The transfer line consists of two 45° dipole magnets, two quadrupole doublets, one quadrupole singlet, and four window frame x/y corrector magnets for adjustment of the beam position and angle. The magnetic elements facilitate a good matching of the beta functions to those of the booster synchrotron as well as a dispersion of zero at the end of the transfer line.

The transverse position and profile of the beam in the transfer line can be determined with two chromium-doped Al_2O_3 beam viewers. The viewers are monitored by CCD cameras and can be moved in and out of the beam by pneumatically-operated actuators. Finally, the absolute pulse current of the beam leaving the microtron can be measured with the help of a fast beam current transformer in the beginning of the transfer line.

3.3.2 Simulations of the injection process

In order to store as many electrons as possible in the booster synchrotron, the racetrack microtron beam is injected over several revolution periods of the booster synchrotron, a so-called *multi-turn injection process* [8]. The strategy of the multi-turn injection process is to displace the closed orbit, and thereby the transverse acceptance, beyond the injection septum sheet by one or more injection kicker magnets. If the closed orbit displacement is reduced while injecting, a significant fraction of the transverse acceptance can be filled without losing the already injected beam on the inside of the injection septum sheet. In case of the ANKA booster synchrotron, the multi-turn injection process is performed with only one injection kicker magnet located diametrically opposite to the 15° injection septum magnet which is shielded from the design orbit by a 1.5 mm thick septum blade (see figure 1.1 or A.1). The position, x_{sep} , of the inside of the septum blade facing the design orbit is -21 mm. The kicker magnet is excited by a half cosine-shaped current pulse which facilitates a *multi-turn injection* on the falling edge of the excitation pulse of the kicker magnet.

If the horizontal and vertical beta functions of the injection transfer line are not matched to those of the booster lattice, the horizontal and vertical betatron functions of the booster synchrotron will oscillate with larger amplitudes than those of the closed lattice. Eventually the modulation of the beam envelope will filament and cause an emittance blowup due to small non-linearities in the actual lattice of the booster synchrotron. As a consequence, the multi-turn injection is investigated for well-matched beta functions in which case the horizontal beam size (one standard deviation) of the injected beam becomes

$$\sigma_x(s) = \sqrt{\varepsilon_{x,m}\beta_x(s) + \left(\frac{\sigma_p}{p}D_x(s) + A\sqrt{\beta_x(s)}\cos(\varphi_x(s) - \varphi_x(s_i) + \lambda)\right)^2}, \quad (3.7)$$

$$\text{where} \quad A = \frac{1}{\sqrt{\beta_x(s_i)}\cos\lambda} \frac{\sigma_p}{p} (D_{x,bl} - D_x(s_i)), \quad (3.8)$$

$$\tan\lambda = -\beta_x(s_i) \frac{\frac{d}{ds}D_{x,bl} - \frac{d}{ds}D_x(s_i)}{D_{x,bl} - D_x(s_i)} - \alpha_x(s_i), \quad (3.9)$$

$\varepsilon_{x,m}$ is the horizontal emittance of the racetrack microtron beam, σ_p/p is the relative momentum spread of the racetrack microtron beam (one standard deviation), $\beta_x(s)$ is the horizontal beta function of the booster synchrotron lattice, $\alpha_x(s)$ is the horizontal alpha function of the booster synchrotron lattice, $D_x(s)$ is the horizontal dispersion of the booster synchrotron lattice, $D_{x,bl}$ is the horizontal dispersion at the end of the injection transfer line, $\varphi_x(s)$ is the horizontal betatron phase of the booster synchrotron lattice, and s_i is the position of the injection septum. Utilizing (3.7), the horizontal extent of the beam at the injection septum, $E_{x\pm}(n) = x(s_i + nC) \pm \sigma_x(s_i + nC)$, can be determined for all septum passages, where n is the number of septum passages after the beam enters the booster synchrotron and C is the circumference of the booster synchrotron. Defining a successful injection as one for which $E_x(n) > x_{sep} + 1$ mm for all $n \geq 1$ (1 mm contingency is added to the injection septum), the quality of the whole multi-injection process can be expressed quantitatively in terms of the following two quality parameters:

$$Q_1 \equiv \int_{E_{x-}(n,t_i) > x_{sep} + 1, n \geq 1} dt_i \quad \text{and} \quad Q_2 \equiv \int_{E_{x-}(n,t_i) > x_{sep} + 1, n \geq 1} \left(\min_{n \geq 1} (E_{x-}) - (x_{sep} + 1) \right) dt_i, \quad (3.10)$$

where t_i is the time of injection relative to the center of the excitation pulse of the injection kicker pulse magnet. Thus, Q_1 is simply the time over which the injection process is successful whereas Q_2 weights both the duration of a successful injection process and how far the injected beam is from the injection septum. Obviously, large values of Q_1 and Q_2 reflect a good injection. Using the expression (3.7), Q_1 and Q_2 can be maximized by varying the amplitude $\Delta x'_{k,max}$ of the excitation pulse of injection kicker magnet, the full width τ_k of the excitation pulse of injection kicker magnet, and the initial angle x'_i of the injected beam relative to the design orbit. It is found that the multi-turn injection process is most efficient if $D_{x,bl}$ is zero, corresponding to a non-matched dispersion at the injection. A horizontal dispersion of zero at the injection septum is advantageous since it permits an injection closer to the design orbit and results in less beam loss in the septum channel because the horizontal beam size is smaller. However, a dispersion of zero at the injection septum causes the dispersion inside the booster synchrotron to oscillate around the dispersion of the

closed lattice as demonstrated by the last term under the square root in equation (3.7). Fortunately, for the optimum choice of $\Delta x'_{k,max}$, τ_k , and x'_i , the dispersion is small when the beam is close to the injection septum resulting in an injection with less beam loss than in case of a matched dispersion. In fact, the optimum value of Q_2 is decreases by 20-50 percent (the exact value depends on the emittance and momentum spread of the racetrack microtron beam) if the dispersion is matched. The emittance blowup resulting from the dispersion mismatch do not influence the injection process significantly as the filamentation of the phase space takes place after the injection kicker magnet has relaxed the transverse oscillation of the beam.

As an example of the maximization procedure, the optimum values of Q_1 and Q_2 for $D_{x,bl}=0.2$ m are shown in figure 3.3 for several values of the horizontal tune Q_x . According to the figure, the injection is successful for more than $0.5 \mu s$ in a rather large Q_x interval, corresponding to a high injection efficiency for more than six revolution periods of the booster. The injection is best in the interval $Q_x=1.75-1.85$ whereas it declines in the vicinity of $2Q_x=3$, $3Q_x=5$, and $Q_x=2$ because the beam for these tunes returns close to the injection septum within only two or three roundtrips after injection. Typical values of the free parameters are $\Delta x'_{k,max}=5$ mrad, $\tau_k=1.5 \mu s$, and $x'_i=-1$ mrad. The associated tolerances of the kicker magnet and septum magnet power supplies are established by demanding that the values of Q_1 and Q_2 should not decrease by more than 25 percent.

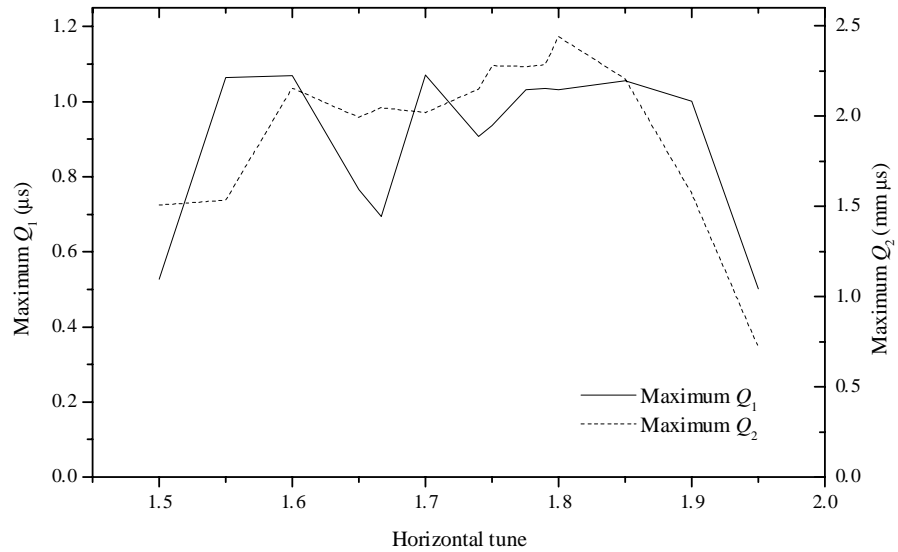


Figure 3.3: The maximum values of Q_1 and Q_2 as a function of the horizontal tune. The parameters of the injected beam are $D_{x,bl}=0.2$ m, $dD_{x,bl}/ds=0$, $\epsilon_{x,m}=0.1$ mm mrad, and $\sigma_p/p=0.002$.

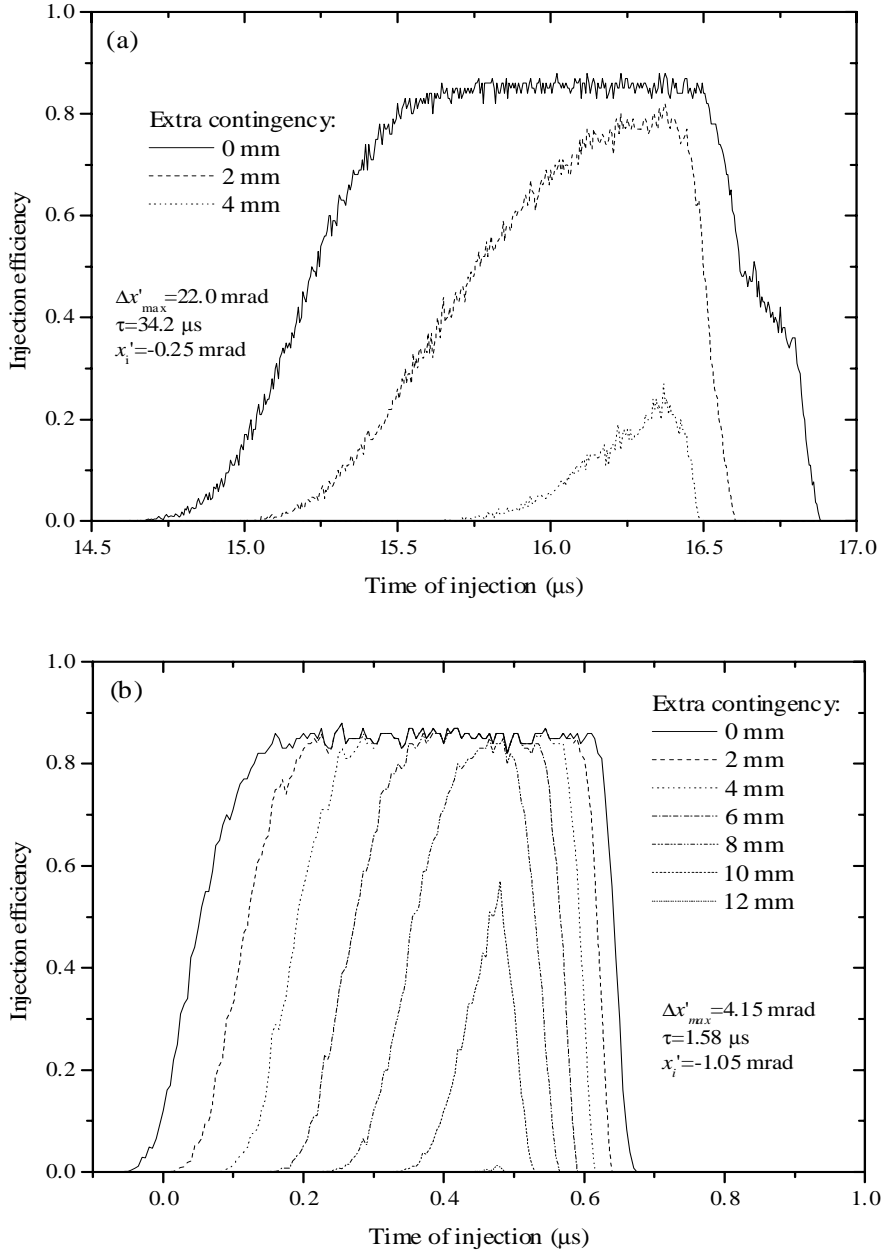


Figure 3.4: Multi-turn injection efficiency versus the time of injection (relative to the center of the excitation pulse of the injection kicker magnet) for $Q_x=1.776$ and various values of the added contingency to inner sides of the injection and extraction septa. The parameters of the injected beam are $D_{x,bl}=0.2$ m, $dD_{x,bl}/ds=0$, $\epsilon_{x,m}=0.2$ mm mrad, and $\sigma_p/p=0.001$. (a) $\Delta x'_{k,max}$, τ_k , and x'_i associated with a maximum value of Q_1 . (b) $\Delta x'_{k,max}$, τ_k , and x'_i associated with a maximum value of Q_2 .

Besides the semi-analytical investigation of the injection process above, the injection process is also studied by tracking an ensemble of 1000 electrons from the instant they leave the injection transfer line until the excitation pulse of the injection kicker magnet has ended. The initial values of the horizontal coordinate and its derivative with respect to the longitudinal position, x and x' , respectively, of each electron are assumed to have a Gaussian distribution with a standard deviation reflecting the lattice functions at the end of the transfer line. After tracking, the injection of a particular electron in the ensemble is interpreted as successful if the electron did not enter the contingency added to the inner side of both the injection and extraction septa (the inner side of the extraction septum is 25 mm from the design orbit), and the multi-turn injection efficiency is defined as the percentage of the electrons which are successfully injected. In figure 3.4 the injection efficiency is plotted as a function of the time of injection for various values of the added septum contingency and for the values of $\Delta x'_{k,max}$, τ_k , and x'_i which produce the maximum values of Q_1 and Q_2 . According to the figure, the injection efficiency in case of an optimum value of Q_1 declines considerable for an extra contingency of only 2 mm, demonstrating that the beam passes very close to the inside of the two septa during the injection process. On the other hand, the injection process associated with an optimum value of Q_2 is much less sensitive to the

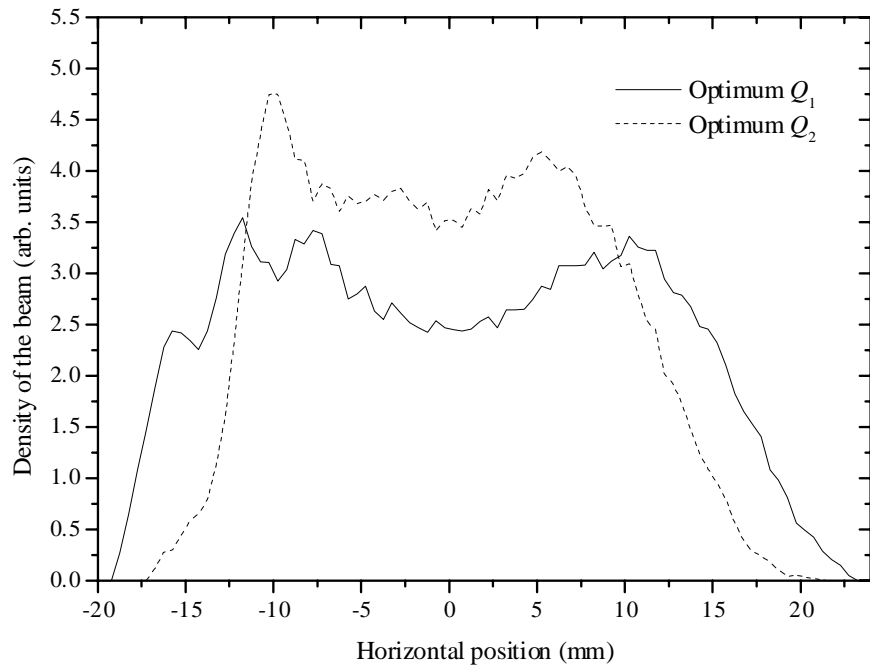


Figure 3.5: Horizontal density profile of the beam at the injection septum for optimum Q_1 and Q_2 after the excitation pulse of the injection kicker magnet has ended. The parameters of the injection process are the same as those figure 3.4 and the added contingency is 2 mm.

added contingency as expected from the definition of Q_2 which favors an injected beam far from the injection septum. Besides, the distribution of the electrons in the transverse phase space after the tracking provides the horizontal density profile of the beam resulting from the injection process, which shown in figure 3.5 for injection parameters associated with the optimum values of Q_1 and Q_2 . The figure reveals that the injection process produces a beam with a small dip in the center, reflecting a hollow distribution of electrons in the horizontal phase space (all electrons have a finite betatron amplitude). As anticipated the injected beam has the smallest horizontal size for the injection parameters associated with a maximum value of Q_2 .

The tracking simulations suggest that the Q_2 quality parameter produces injection parameters of significantly more practical relevance than those of Q_1 . In fact, figure 3.4b suggests that an injection efficiency of about 80 percent for 4-5 revolutions is feasible for values of $\Delta x'_{k,max}$, τ_k , and x'_i related to the maximum of Q_2 . For a racetrack microtron pulse with a current of 10 mA, this would yield a stored electron current of roughly 35 mA. Additional tracking simulations demonstrate that the injection efficiency is rather insensitive to the horizontal betatron functions of the injection transfer line. This is attributed to the small horizontal emittance of the racetrack microtron beam which gives rise to a modest betatron oscillation induced beam size in the booster synchrotron.

3.3.3 Capture efficiency of the rf system

The simulation of the injection process above only considers the transverse motion of the beam the first few hundred revolutions after it is injected into the ring. However, long-term storage of the beam is strongly influenced by the longitudinal acceptance of the booster synchrotron. In particular, an electron which is not injected into the longitudinal bucket will eventually be lost due to synchrotron radiation-induced energy loss. The stable longitudinal phase space within the bucket is separated from unstable regions of phase space by the *separatrix*, which is given by

$$\left(\frac{\Delta p}{p}\right)_{sep}^2 = \pm \frac{2eV_{cav}}{\pi h |\gamma^{-2} - \alpha_p| \beta c p_0} \frac{1 + \cos \phi}{2}, \quad \phi \in [-\pi, \pi] \quad (3.11)$$

for a stationary rf bucket, where $\Delta p/p$ is the relative momentum deviation, V_{cav} is the amplitude of the cavity voltage, h is the number of bunches in the booster synchrotron, γ and β are the relativistic gamma and beta factors, α_p is the momentum compaction factor of the booster synchrotron, and ϕ is the phase deviation from the synchronous phase ϕ_s which is defined as $U_0/e = V_{cav} \cos \phi_s$, where U_0 is the synchrotron radiation loss per revolution [7^{chap. 8}]. It follows from (3.11) that most electrons which are injected close to a phase deviation of $\pm\pi$ are not captured by the rf bucket.

Assuming that the 3 GHz structure of the racetrack microtron beam has disappeared

during the multi-turn injection process, the fraction of electrons which are captured in the rf bucket becomes

$$\frac{1}{2\pi} \int_{-\pi}^{\pi} \int_{-(\Delta p/p_0)_{sep}}^{(\Delta p/p_0)_{sep}} \rho_{inj}(\Delta p/p_0) d(\Delta p/p_0) d\phi, \quad (3.12)$$

where $\rho_{inj}(\Delta p/p)$ is the normalized relative momentum distribution of the injected beam. Assuming a Gaussian momentum distribution of the injected beam with a standard deviation of σ_p , one obtains the capture efficiency which is plotted in figure 3.6 as a function of V_{cav} for several values of σ_p . As expected the capture efficiency is high for a large cavity voltage and a small momentum spread of the injected beam. However, the injection process will not benefit from a too large cavity voltage because the voltage according to (3.11) produces a momentum spread and therefore an enlarged horizontal beam size via the horizontal dispersion D_x . In fact, owing to the rather large horizontal beam size following the injection process (see figure 3.5), the contribution of the momentum spread to the horizontal beam size at the injection septum should not be larger than ~ 5 mm. This is equivalent to a maximum tolerable momentum spread of $0.005 \text{ m}/D_x = 2.8 \cdot 10^{-3}$ and thus a maximum acceptable cavity voltage of 6.8 kV using (3.11). Accordingly, a good compromise between a good

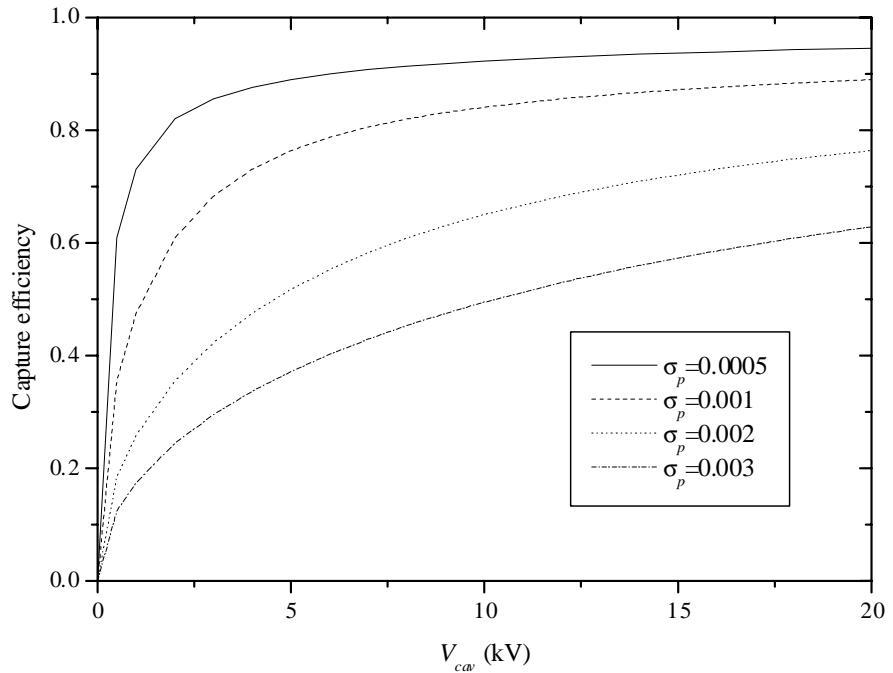


Figure 3.6: Fraction of electrons captured in the stationary rf bucket versus the amplitude of cavity voltage and the relative momentum spread of the injected beam

capture efficiency and a modest rf-induced beam loss is a cavity voltage of 5 kV (a relative momentum spread of the injected beam of 0.001 is assumed). In this case the capture efficiency is ~75 percent corresponding to a captured beam current of ~25 mA by the rf system.

3.3.4 Influence of beam loading on the injection process

In addition to the rf voltage produced by the external generator, the beam itself will also induce a 500-MHz rf voltage in the cavity once the beam starts forming a 500-MHz bunch structure. For a bunch length much shorter than the rf wave length, one obtains with the help of (2.14) a beam-induced voltage of $V_{br}=2R_s I_b/((1+\kappa)(1+\alpha K))$ for a generator frequency at the cavity resonance, where αK is the open loop gain of the fast rf feedback loop. Hence, for the expected beam current of 25 mA, the beam-induced voltage is $83/(1+K\alpha)$ kV at resonance, suggesting a strong perturbation of the longitudinal dynamics by the beam. In fact, the beam-cavity interaction only has a steady-state solution provided the equations relating the cavity voltage, the cavity detuning, and the generator power have a solution [9]:

$$V_{gr} \cos \phi_L = V_{cav} + V_{br} \cos \phi_s \quad , \quad V_{gr} = \frac{\sqrt{8\kappa}}{1+\kappa} \sqrt{R_s P_g} \quad (3.13)$$

$$2Q_L \frac{\omega_{cav} - \omega_{rf}}{\omega_{cav}} = (1 + V_{br}/V_{cav} \cos \phi_s) \tan \phi_L - \frac{V_{br}}{V_{cav}} \cos \phi_s \quad , \quad (3.14)$$

where V_{gr} is the amplitude of the generator-induced voltage in the cavity at resonance, ϕ_L is the phase between the generator-induced voltage at resonance and the cavity voltage, R_s is the shunt impedance of the cavity, P_g is the power delivered by the generator to the cavity, $Q_L=Q/(1+\kappa)$ is the loaded quality factor of the cavity, κ is the coupling coefficient between the transmission line and the cavity, ω_{rf} is the angular rf frequency, and ω_{cav} is the resonant angular frequency of the cavity. Combining (3.13) and (3.14), the condition for stable steady-state operation at injection can be formulated as

$$1 - \frac{V_{br}^2}{V_{gr}^2} + 4Q_L^2 \frac{(\omega_{cav} - \omega_{rf})^2}{\omega_{cav}^2} \geq 0 \quad (\omega_{cav} \leq \omega_{rf}) \quad (3.15)$$

$$V_{br} \leq V_{gr} \quad (\omega_{cav} > \omega_{rf}) \quad , \quad (3.16)$$

where it has been employed that the synchronous phase is very close to $\pi/2$ at injection because the synchrotron radiation loss per revolution only is 0.435 eV. It follows that the beam-cavity interaction for the maximum generator power of 200 W only is stable at resonance if $V_{br} \leq V_{gr}$, corresponding to $I_b \leq 11.1(1+\alpha K)$ mA. Alternatively, stability can be achieved without fast rf feedback by detuning the cavity resonance sufficiently far below

the rf frequency.

Although the beam-cavity interaction is stable, the generator may not be able to produce a sufficiently high cavity voltage. The required generator power to produce a cavity voltage of V_{cav} for an arbitrary detuning and synchronous phase is according to (3.13) and (3.14)

$$P_g = \left(1 + \left(\frac{2Q_L (\omega_{cav} - \omega_{rf}) / \omega_{cav} + (V_{br} / V_{cav}) \sin \phi_s}{1 + (V_{br} / V_{cav}) \cos \phi_s} \right)^2 \right) \times \frac{(1 + \kappa)^2}{8\kappa R_s} (V_{cav} + V_{br} \cos \phi_s)^2 . \quad (3.17)$$

The rf system of the booster synchrotron should be able to maintain a quantum lifetime of at least one second at 500 MeV equivalent to a cavity voltage of 14 kV. Combining this condition with (3.17) at resonance, one finds that the generator only is capable of delivering enough rf power at 500 MeV provided the beam-induced voltage is less than 30.9 kV, corresponding to the condition $I_b \leq 9.3(1 + \alpha K)$ mA. If on the other hand the beam loading only is suppressed by detuning the cavity, it follows from (3.17) that a minimum detuning of 120 kHz below the rf frequency is necessary at injection (for the optimum cavity voltage of 5 kV at injection and the expected beam current of 25 mA) for the available generator power of 200 W. A large detuning is not advantageous, however, because the optimum detuning depends on the beam current, the synchronous phase and the cavity voltage which all change significantly throughout the one-second cycle of the injector. As a consequence, the required generator power increases far above the capability of the solid-state amplifier due to large reflections from the cavity. Therefore, without sufficient gain of the fast rf feedback loop, the rf system cannot provide a cavity voltage which is appropriate for an efficient capture of the beam with the result that significant beam loss will occur. However, a small detuning below resonance will reduce reflections and assist the effect of the fast rf feedback loop throughout the whole one-second cycle of the booster synchrotron. The optimum detuning decreases with the gain of the fast rf feedback loop.

Until now, the beam-cavity interaction has only been analyzed under steady-state conditions. This formalism cannot describe the abrupt increase of the beam loading at injection which causes a transient behavior of the beam-cavity interaction. In fact, if the transient behavior is not damped within less than a small fraction of a synchrotron period, beam blow-up and beam loss is likely to occur as a result of the strong distortion of the longitudinal phase space. Unfortunately, the minimum response time of 2 ms of the amplitude loop of the booster synchrotron is more than three orders of magnitude too slow to correct for the transient beam loading. However, the required generator power in (3.17) is unchanged at injection if the cavity is detuned

$$\omega_{rf} - \omega_{cav} = \frac{R_s I_b}{2(1 + \alpha K) Q V_{cav}} \omega_{cav} . \quad (3.18)$$

below resonance. Hence, for the optimum cavity voltage of 5 kV and the expected beam current of 25 mA, the transient behavior of the beam-cavity interaction do not emerge if the cavity is detuned 108/(1+ αK) kHz below the rf frequency at injection. Again, this is not possible with the available generator power without suppression of the beam loading by the fast rf feedback loop.

Besides the stability criterion (3.15) above, the derivative of the acceleration voltage $V_{cav} \cos \phi_s$ should be negative throughout the passage of the electron bunch in order to produce a restoring force for non-synchronous particles, the so-called *Robinson's phase-stability criterion* [9]:

$$2V_{cav} \sin \phi_s + V_{br} \sin(2\psi) > 0 \quad , \quad \tan \psi = 2Q_L \frac{\omega_{cav} - \omega_{rf}}{\omega_{cav}} . \quad (3.19)$$

According to the criterion, longitudinal beam instability may occur at injection ($\phi_s \approx 90^\circ$) if the beam-induced voltage is more than twice as large as the cavity voltage. The detunings for which the longitudinal dynamics is stable and unstable at injection is plotted in figure

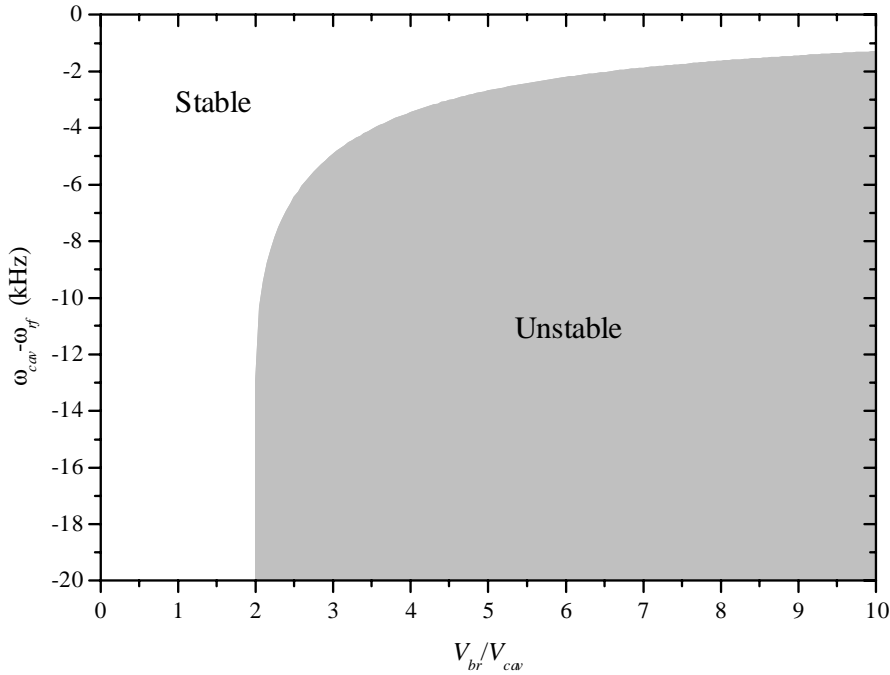


Figure 3.7: Stable and unstable detunings at injection ($\phi_s \approx 90^\circ$) according to Robinson's phase-stability criterion as a function of the amplitude of the beam-induced voltage.

3.7 as a function of the beam induced voltage. For the optimum cavity voltage of 5 kV at injection and the expected beam current of 25 mA, the criterion requires that $\omega_{rf} - \omega_{cav} < 0.78$ kHz without fast rf feedback loop. At the same time, the cavity resonance should be detuned below the rf frequency in order to avoid the Robinson instability [10]. Consequently, beam stability confines ω_{cav} within a very narrow interval.

The analysis above suggests that the rf system in steady state is capable of capturing a beam current of 25 mA and accelerating a beam current of 20 mA to 500 MeV if the beam-induced voltage is reduced by at least factor of 2.3 by means of the fast rf feedback loop, corresponding to $\alpha K = 1.25$. However, for the optimum cavity voltage of 5 kV at injection and the expected beam current of 25 mA, a much higher gain of the loop, corresponding to $\alpha K = 7.3$, is necessary to simultaneously suppress the transient beam loading and fulfill Robinson's phase-stability criterion. If the loop gain is not large enough for a stable beam-cavity interaction, the bunch length will increase or/and beam loss will occur until the beam induced voltage is small enough that stable longitudinal dynamics is feasible.

3.4 Beam acceleration

3.4.1 The ramping scheme

The ramping of the beam energy from the injection energy of 53 MeV to the extraction energy of 500 MeV is controlled by a ramping curve which sets the current of the dipole magnet power supply. The ramping curve is loaded from a computer into the control board of the dipole magnet power supply, enabling an arbitrary curve form of the ramping curve. Similarly, the ramping of the horizontally-focusing quadrupole magnet family is controlled by an another ramping curve which can be manipulated separately, facilitating an accurate control of the tunes throughout the ramping. This is necessary in order to correct for saturation effects in the dipole and quadrupole magnets during ramping. At the same time, the rf voltage is increased from its optimum value at injection with the help of a programmable function generator in order to obtain a quantum lifetime in excess of one second for all electron energies.

The maximum ramping speed of the dipole and quadrupole magnet power supplies is 0-100 percent in 400 ms, facilitating ramping of the energy from 53 MeV to 500 MeV with a smooth ramping curve in less than 600 ms. This is sufficient for achieving a repetition rate of 1 Hz for the full cycle of the injector.

3.4.2 Eddy current effects in the dipole magnet vacuum chamber

During ramping the magnetic flux through the vacuum chamber inside a dipole magnet changes with the excitation of the dipole magnet. According to Faraday's law of induction, the time-dependent magnetic flux will induce eddy currents in the walls of the vacuum chamber. In appendix D it is shown that the eddy currents produce a magnetic field at the

position of the beam with a sextupole component. If the modified boundary conditions originating from the iron yoke of the dipole magnet are neglected and the vacuum chamber walls are much thinner than the dimensions of the vacuum chamber, it is shown in appendix D that the strength of the sextupole component in the center of a rectangular vacuum chamber is

$$m_{eddy} = \frac{4}{\pi} \frac{b^3}{(h^2 + b^2)^2} \frac{\mu_0 \sigma d}{\rho} \frac{dB_y/dt}{B_y} . \quad (3.20)$$

Here σ is the conductivity of the vacuum chamber material, ρ is the bending radius of the beam trajectory in the dipole magnets, B_y is the vertical component of the dipole magnet field, d is the wall thickness of the vacuum chamber, and h and b are the half height and half width of the vacuum chamber, respectively.

If the presence of the magnetic materials in vicinity of the vacuum chamber cannot be disregarded, the problem of finding the sextupole strength becomes much more complex and one has to resort to numerical techniques. However, if the pole faces of the dipole magnet are approximated by two infinitely large iron plates with an infinite permeability, analytical properties of the sextupole strength can be established [11]. For example, it can be shown that the sextupole strength for all vacuum chamber geometries scales as $m \propto g^{-1}$ if the dipole magnet gap g and the dimensions of vacuum chamber are scaled together. In addition, it can be shown that the sextupole strength approaches the value

$$m_{eddy} = \frac{2}{g} \frac{\mu_0 \sigma d}{\rho} \frac{dB_y/dt}{B_y} \quad (3.21)$$

if the width of the vacuum chamber is much larger than the gap g [11,12]. For a wide chamber ($b \gg h$) this expression is roughly a factor of b/g larger than that in (3.20). This is attributed to an enhancement of the sextupole field by the surrounding magnetic material. Finally, the analytical investigation of the sextupole strength reveals that the sextupole strength generally is larger for a rectangular vacuum chamber than for an elliptical vacuum chamber.

The sextupole field produced by the eddy currents can be harmful to the beam because the field gives rise to a shift of the horizontal and vertical chromaticities which may induce a large tune spread. The horizontal and vertical chromaticity shifts are

$$\Delta\xi_x = \frac{1}{4\pi} \oint m_{eddy} \beta_x D_x ds = K_x m_{eddy} = 2.47 m_{eddy} \quad (3.22)$$

$$\Delta\xi_y = -\frac{1}{4\pi} \oint m_{eddy} \beta_y D_x ds = K_y m_{eddy} = -6.28 m_{eddy} , \quad (3.23)$$

where the integration is through the entire lattice, m_{eddy} is zero except in the dipole magnets, D_x is the horizontal dispersion, and β_x and β_y are the horizontal and vertical beta functions,

respectively [7^{p. 259}]. For the booster synchrotron one has $b=35$ mm, $h=13.25$ mm, $d=1.5$ mm, $g=30$ mm, $\rho=1.67$ m, $\max((dB_y/dt)/B_y)\sim 7$ s⁻¹, and $\sigma=1.45\cdot 10^6$ $\Omega^{-1}\text{m}^{-1}$, yielding maximum chromaticity shifts of $\Delta\xi_x=0.8$, $\Delta\xi_y=-2.0$ and $\Delta\xi_x=1.9$, $\Delta\xi_y=-4.8$ for expression (3.20) and (3.21) for the sextupole strength, respectively. The eddy currents in the dipole magnet vacuum chamber is thus expected to modify the chromaticities of the booster synchrotron substantially during ramping.

3.5 The extraction

3.5.1 The extraction process

Shortly after the beam has reached the final energy of 500 MeV, the electron beam is extracted from the booster synchrotron in a one-turn process in which a fast kicker magnet displaces the beam to the outside of the extraction septum sheet after 3/4 revolution (the positions of the kicker magnet and the extraction septum are indicated in figure 1.1). Subsequently, the beam is transported to the extraction transfer line by the extraction septum magnet. The demands to the kicker magnet is reduced by locating the kicker magnet and the septum at maxima of the horizontal betatron function and by choosing a phase advance from the kicker magnet to the septum which is a multiple of π plus $\pi/2$. Furthermore, the required strength of the kicker magnet is reduced by almost an order of magnitude by displacing the closed orbit to a horizontal position only 2-3 mm from the extraction septum sheet during the last 40 ms before extraction. The displacement is produced by separate windings in the four dipole magnets closest to the extraction septum. In order to extract as many electrons as possible, the kicker magnet supply is designed to provide a very short rise time of less than 30 ns and a longer flattop of more than 100 ns, facilitating an extracted electron pulse with a duration of more than 58 ns.

3.5.2 The extraction transfer line

The extraction transfer line transports the electron beam from the extraction septum of the booster synchrotron to the injection septum of the storage ring. As illustrated in figure 1.1 and A.1, the beam path is defined by two 27.5° dipole magnets while a good matching between the lattice functions of the booster synchrotron and those of the storage ring is ensured by nine quadrupole magnets. In addition, four window frame x/y corrector magnets are utilized for small adjustments of the beam position and angle.

The position and profile of the beam in the transfer line can be determined by three chromium-doped Al₂O₃ beam viewers. Each viewer is monitored by a CCD camera through a window in the vacuum chamber and can be moved in and out of the beam by means of pressurized air. Furthermore, the beam current of the electron pulse is monitored by a beam current transformer just after the extraction septum (same design as in the racetrack microtron) and a fast beam current transformer just before the injection septum of the ANKA

storage ring.

References:

- [1] Documentation of the lattice program OPTIM 2.0
- [2] A. Fabris *et al.*, in Proc. European Part. Acc. Conf., Stockholm, 1998, p. 1764
- [3] D. Boussard, IEEE Trans. Nucl. Sci. **NS-32**, p. 1852 (1985)
- [4] F. Pérez *et al.*, in Proc. European Part. Acc. Conf., Vienna, 2000, p. 1996
- [5] A. Gamp, *Servo Control of RF Cavities under Beam Loading*, in Proc. RF Engineering for Particle Accelerators, CERN Accelerator School, Oxford, 1991, edited by S. Turner (CERN, Geneva, 1992), p. 396
- [6] R. C. Dorf, *Modern Control Systems*, Addison-Wesley, Massachusetts, 1973, p. 216
- [7] H. Wiedemann, *Particle Accelerator Physics*, Springer-Verlag, Berlin, 1993
- [8] G. H. Rees, in Proc. Fifth General Accelerator Physics Course, CERN Accelerator School, Jyväskylä, Finland, 1992, edited by S. Turner (CERN, Geneva, 1994), p. 731
- [9] K. Akai, *Overview of RF Systems for Storage Rings and their Diagnostics*, in *Beam Measurement*, Proc. of the Joint US-CERN-Japan-Russia School on Particle Accelerators, edited by S-i. Kurokawa *et al.*, Montreux 1998 (World Scientific, Singapore, 1999), p. 378
- [10] A. W. Chao, *Physics of Collective Beam Instabilities in High Energy Accelerators*, John Wiley & Sons, New York, 1993, p. 162
- [11] S. Y. Lee, Nucl. Instr. and Meth. **A300**, p. 151 (1991)
- [12] D. A. Edwards and M. J. Syphers, *An Introduction to the Physics of High Energy Accelerators*, John Wiley & Sons, New York, 1993, p. 113

Chapter 4

Experimental investigation of the ANKA racetrack microtron

4.1 Introduction

The ANKA racetrack microtron was assembled at Danfysik in the autumn of 1998, and subsequently moved to the department of the Niels Bohr Institute at Risø National Laboratory for testing. Here it delivered the first output pulse with a beam current of 2 mA and a duration of 200 ns in December 1998. In February 1999, the racetrack microtron was moved to its final destination at Forschungszentrum Karlsruhe for commissioning. The commissioning ended in the beginning of March 1999 when the racetrack microtron was able to produce an electron pulse with an average current of 16 mA and a pulse duration of 1.6 μ s. Since then, the racetrack microtron has continuously been delivering an electron beam to the ANKA booster synchrotron.

4.2 Beam current

4.2.1 Characterization of the current transformers

For a step-shaped current pulse with an abrupt onset at $t=0$ s, an ideal passive current transformer produces the voltage

$$V_R(t) = \frac{I_b R}{N} e^{-(R/L)t} , \quad (4.1)$$

where I_b is the beam current, R is the impedance of the external load (typically an oscilloscope with 50 Ω termination), N is the number of turns of the secondary winding, and L is the inductance of the secondary winding [1]. As an example, the voltage signal of current transformer 1 of the racetrack microtron is shown in figure 4.1. The decline of the voltage throughout the current pulse and the subsequent decay of the negative signal towards zero beyond 5 μ s are both attributed to the exponential decay in (4.1). Fitting each decay with

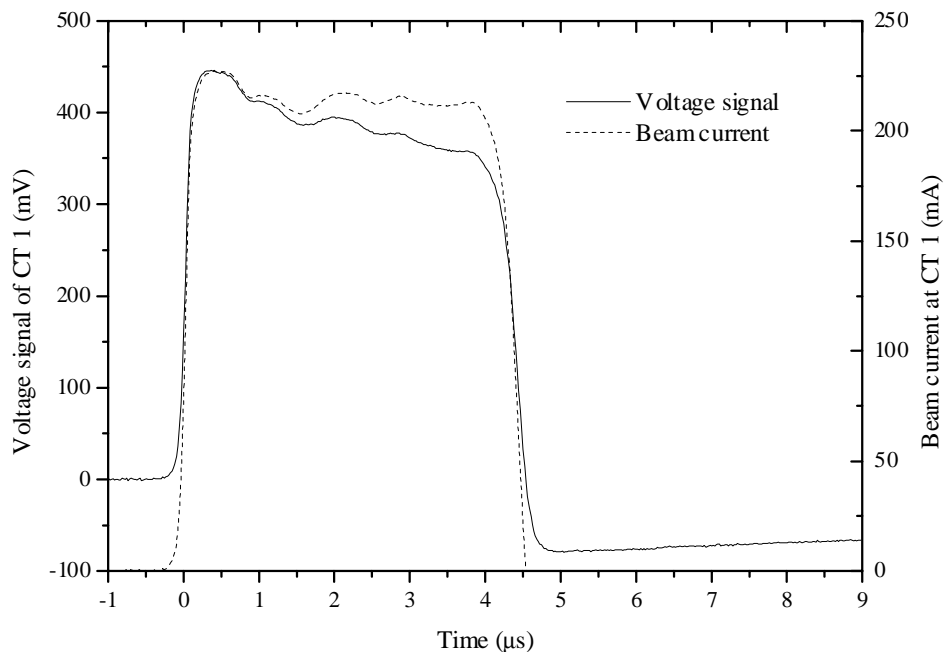


Figure 4.1: Voltage signal of current transformer 1 (CT 1 in figure 2.1). The signal is measured with an oscilloscope terminated in 50Ω ($R=50 \Omega$). In addition, the corresponding beam current is plotted.

the exponential decay of (4.1), one obtains a $1/e$ decay time of $21 \mu\text{s}$ for both decays, corresponding to an inductance of the secondary winding of 1.1 mH . Knowing the decay time, the measured voltage signal of all the current transformers of the racetrack microtron are easily converted into an absolute beam current using (4.1).

4.2.2 Beam current measurements

The beam current is the most significant property of the racetrack microtron beam because the circulating current of the booster synchrotron is proportional to the output beam current of the racetrack microtron. Therefore, the beam current of the racetrack microtron is monitored throughout the entire beam recirculation. Initially, the beam current is determined by current transformer 1 shortly after the electron gun. A typical current pulse is plotted in figure 4.1, revealing a gun current of 215 mA and a pulse duration of $4 \mu\text{s}$. Subsequently, current transformer 3 and 4 measure the total recirculating current on the linac axis. The beam currents of both current transformers are presented in figure 4.2. Current transformer 3 has one large negative contribution from the first beam passage, before the direction of recirculation is reversed, and multiple positive contributions from the subsequent nine beam passages. The signal from current transformer 4 is larger than that of current transformer 3

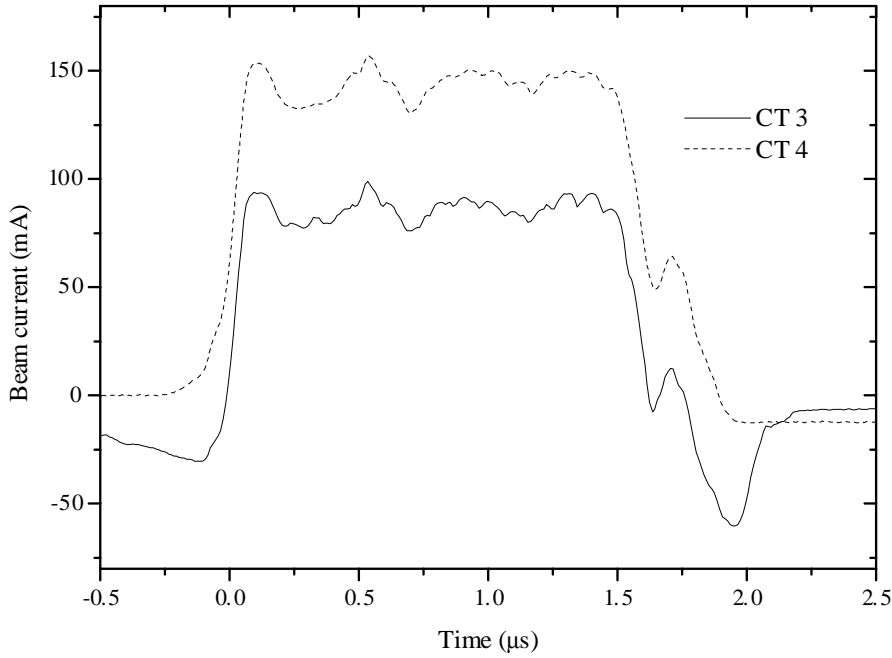


Figure 4.2: Beam current at current transformer 3 and 4 (CT 3 and CT 4 in figure 2.1).

because all nine beam passages contribute with a positive beam current. The current pulses of both current transformer 3 and 4 are significantly shorter than the initial electron pulse from the electron gun because the timing of the linac field only provides the correct acceleration voltage for $\sim 1.5 \mu\text{s}$. Furthermore, the beam currents in racetrack orbit 3 to 6 (21.2 MeV to 37.1 MeV) and the output beam current of the racetrack microtron are shown in figure 4.3, demonstrating very small beam losses from an energy of 20 MeV to the final energy of 53 MeV. In fact, a comparison of the observed output current of 14 mA with the total beam current of 143 mA at current transformer 4 (corresponds to an average beam current per beam passage of 16 mA) reveals that almost all beam loss occurs before the second linac passage is completed. The significant initial beam loss is attributed to the large fraction of the electrons which are not injected into the longitudinal acceptance.

According to energy conservation, the power delivered to the beam by the rf field is

$$I_b \Delta E/e = P_g - P_{walls} - P_r = P_g - \frac{(\Delta E/e)^2}{2R_s (\cos \phi_s)^2} - P_r , \quad (4.2)$$

where I_b is the total beam current in the linac, ΔE is the synchronous energy gain in the linac, P_g is the forward power delivered by the klystron, P_{walls} is the power dissipated in the linac walls, P_r is the reflected power from the linac, R_s is the shunt impedance of the linac,

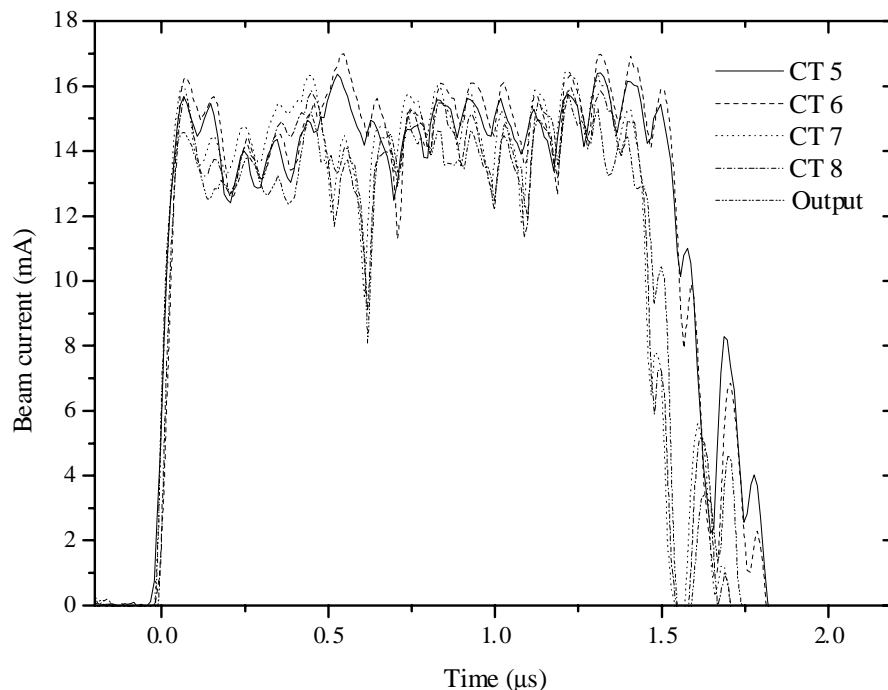


Figure 4.3: Beam current in racetrack orbit 3 to 6 (measured by current transformer CT 5-8 in figure 2.1) and the output beam current of the racetrack microtron (determined by the current transformer in the injection transfer line).

and ϕ_s is the synchronous phase. Solving (4.2) for the total beam current in the linac, one obtains a total beam current of 283 mA for a synchronous phase of 19° and measured forward and reflected powers of 2.46 MW and 0.11 MW, respectively. This is very close to the maximum beam current of 329 mA in the linac which was established by means of beam-cavity stability arguments in paragraph 2.5.1, suggesting that an output beam current significantly higher than 15 mA cannot be expected.

4.3 Momentum spread

The momentum spread of the racetrack microtron beam dominates the horizontal beam size of the output beam for a sufficient large momentum spread and horizontal dispersion. In fact, the simulation of the injection process in paragraph 3.3.2 reveals that the injection efficiency is significantly more sensitive to the momentum spread than to the horizontal emittance and beta function.

If the rf system of the booster synchrotron is turned off and the rf cavity is detuned far from resonance in order to suppress the interaction between the beam and the cavity, the momentum distribution of the output beam of the racetrack microtron can be determined by

recording the revolution frequency distribution of the beam after it is injected into the booster synchrotron. More precisely, assuming that all momentum components of the beam have the same injection efficiency, the frequency spectrum can easily be converted into a momentum distribution using the relation between a momentum deviation Δp and a revolution frequency deviation Δf_{rev} in presence of constant bending field:

$$\frac{\Delta p}{p} = -\frac{1}{\alpha_p} \frac{\Delta f_{rev}}{f_{rev}}, \quad (4.3)$$

where f_{rev} is the center revolution frequency and α_p is the momentum compaction factor of the booster synchrotron [2]. The revolution frequency spectrum of the beam is determined by a spectrum analyzer connected to the sum signal of all four striplines at the stripline unit DSL_B.02. The spectrum analyzer is operated in a time-gated mode in which the stripline signal only is analyzed from 1 ms to 2 ms after injection, allowing a good time resolution and a small resolution bandwidth of only 1 kHz (equivalent to a relative momentum resolution of $0.4 \cdot 10^{-4}$ according to (4.3)). In this mode of operation, however, only one data point of the spectrum is recorded for each injection, requiring a measurement over at least 100 injections for a satisfactory frequency spectrum. Accordingly, the momentum spectrum

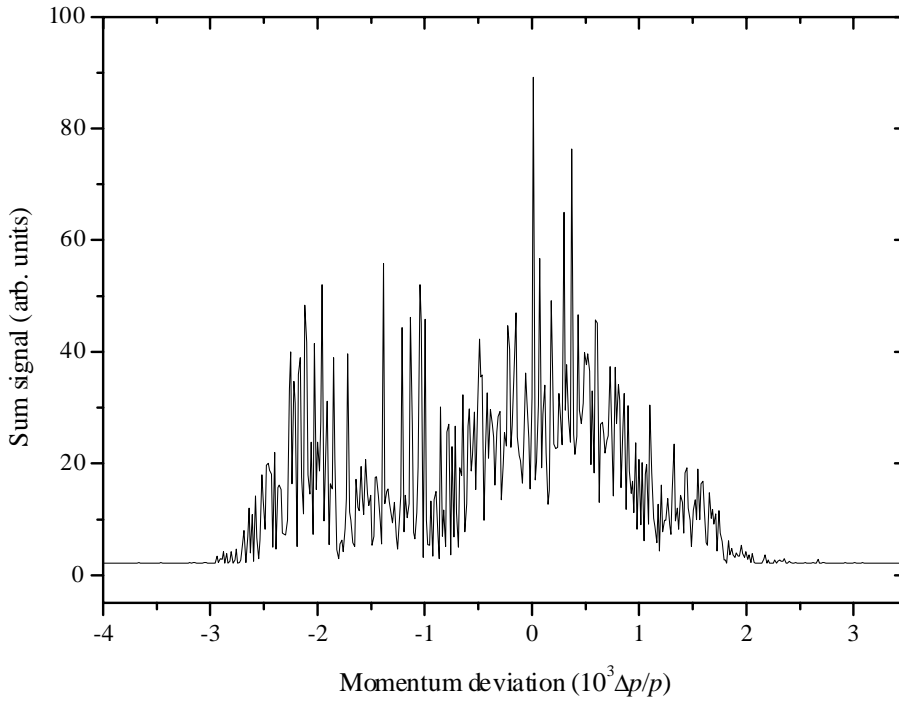


Figure 4.4: Average momentum distribution of the injected beam 1-2 ms after injection.

includes the shot-to-shot momentum variation of the microtron beam.

A typical average momentum distribution of the injected beam is shown in figure 4.4. A statistical analysis of the distribution yields a relative momentum spread of 0.0011 ± 0.0001 (one standard deviation) for the nominal setting of the racetrack microtron. Single-shot measurements of the momentum distribution with a resolution bandwidth of 3 kHz yields the same momentum spread and reveals pulse-to-pulse variations of the center momentum and the relative momentum spread of $\sim 0.2 \cdot 10^{-4}$ (likely to be dominated by measurement uncertainties).

4.4 Transverse emittances of electron beam

4.4.1 The extended variable quadrupole magnet method

Assume the beam has a Gaussian distribution of betatron amplitudes in the transverse phase space of the form

$$\rho(z, z') = \frac{N}{2\pi\sqrt{\det \boldsymbol{\sigma}}} \exp\left(-\frac{1}{2 \det \boldsymbol{\sigma}} (\sigma_{22}^2 z^2 - 2\sigma_{12} z z' - \sigma_{11} z'^2)\right), \boldsymbol{\sigma} = \begin{pmatrix} \sigma_{11} & \sigma_{12} \\ \sigma_{12} & \sigma_{22} \end{pmatrix}, \quad (4.4)$$

where N is the total number of electrons, $\boldsymbol{\sigma}$ is the symmetric *beam matrix*, and z, z' are one of the transverse coordinates and its derivative with respect to the longitudinal position, respectively [3]. In this case the *transverse emittance* of the beam is usually defined as

$$\varepsilon = \sqrt{\det \boldsymbol{\sigma}} = \sqrt{\sigma_{11}\sigma_{22} - \sigma_{12}^2}, \quad (4.5)$$

corresponding to $1/\pi$ times the area of the elliptical contour in phase space which encloses 39.3 percent of the electrons. Furthermore, the lattice functions are related to the beam matrix by the following relations:

$$\beta = \sigma_{11}/\varepsilon, \quad \alpha = -\sigma_{12}/\varepsilon \quad \text{and} \quad \gamma = (1 + \alpha^2)/\beta = \sigma_{22}/\varepsilon, \quad (4.6)$$

where β is the beta function, α is the alfa function, and γ is the gamma function [4]. Thus, the emittance and all lattice functions can be determined if the beam matrix is known.

The diagnostic tools of the racetrack microtron and the following injection transfer line only provide the means for determining the two-dimensional transverse profile of the beam at specific positions. Projecting the two-dimensional transverse profile onto the z -axis, one obtains according to (4.4) a one-dimensional Gaussian density distribution of the form

$$\rho_1(z) = \int_{-\infty}^{\infty} \rho(z, z') dz' = N(2\pi\sigma_{11})^{-\frac{1}{2}} \exp(-z^2/2\sigma_{11}) \quad (4.7)$$

which has a one standard deviation width of $\sqrt{\sigma_{11}}$. Hence, only the matrix element σ_{11} can be established directly from the measured transverse profile. According to the theory of linear beam optics, the value of σ_{11} at a specific position s_1 is given by

$$\sigma_{11}(s_1) = (\mathbf{R}\boldsymbol{\sigma}(s_0)\mathbf{R}^T)_{11} = R_{11}^2\sigma_{11}(s_0) + 2R_{11}R_{12}\sigma_{12}(s_0) + R_{12}^2\sigma_{22}(s_0) . \quad (4.8)$$

Here \mathbf{R} is the transfer matrix from a reference position s_0 to s_1 defined as

$$\begin{pmatrix} z \\ z' \\ \Delta p/p \end{pmatrix}_{s_1} = \mathbf{R} \begin{pmatrix} z \\ z' \\ \Delta p/p \end{pmatrix}_{s_0} , \quad (4.9)$$

where $\Delta p/p$ is the relative momentum deviation of the particle. All the matrix elements of the beam matrix at the reference position can therefore be inferred if σ_{11} is measured for several settings of the lattice between s_0 and s_1 with known transfer matrices. Since the beam matrix has three unknown matrix elements, at least three different lattice settings are required for a full determination of the beam matrix. For example, the lattice can easily be changed by scanning an intermediate quadrupole magnet situated between s_0 and s_1 , the so-called *variable quadrupole magnet method* [3].

So far the enlargement of the transverse beam size by a finite dispersion and momentum spread has been neglected. Including this effect and assuming a Gaussian momentum distribution, the total transverse beam size at s_1 finally becomes

$$\sigma_{tot}(s_1) = \sqrt{\sigma_{11}(s_1) + (\sigma_p/p)^2 D(s_1)^2} , \quad (4.10)$$

where σ_p/p is the one standard deviation relative momentum spread and $D(s_1)$ is the dispersion at s_1 which is given by [5]

$$D(s_1) = D(s_0)R_{11} + D'(s_0)R_{12} + R_{13} . \quad (4.11)$$

Thus, if both the beam size and the dispersion at s_1 is measured for each setting of the intermediate quadrupole magnet, both the momentum spread and the beam matrix at the reference point can be determined provided $\sigma_{tot}(s_1)$ is determined for at least four different quadrupole magnet settings. This is a rather general method for determining the quality of the beam which will be called the *extended variable quadrupole magnet method*.

4.4.2 Measurement of the transverse emittances by the extended variable quadrupole magnet method

The transverse emittances characterizes the quality of the beam in terms of beam size and divergence. For this reason, small transverse emittances of the output beam of the racetrack microtron are advantageous for the multi-turn injection process of the booster synchrotron.

According to the discussion in the previous paragraph, the transverse emittances of the output beam can be determined by utilizing the extended variable quadrupole magnet method in the injection transfer line. First, the transverse profile of the beam is measured at viewer DCCDFS_I.02 at the end of the injection transfer line for various excitations of quadrupole magnet MQ_I.01 (the positions of the viewer and the quadrupole magnet are indicated in figure A.1). The beam-induced light spot in the fluorescent material of the viewer is recorded by a CCD camera through a window in the vacuum chamber. The image of the spot is transferred to a computer by means of a frame grabber system which also synchronizes the triggering of the camera with the electron pulse. The absolute spot size is calibrated by recording the image of a ruler at the same distance from the camera as the viewer. For each quadrupole magnet excitation, the intensity distribution of the camera image is projected into both the horizontal and vertical planes, and the one-dimensional projected distributions are characterized in terms of their weighted mean and one standard deviation width.

Furthermore, for each quadrupole magnet excitation, the transverse profile is recorded for both the nominal setting of the racetrack microtron and for a setting with a reduced excitation of the 180° dipole magnets by 0.77 percent. According to (2.3), the reduced di-

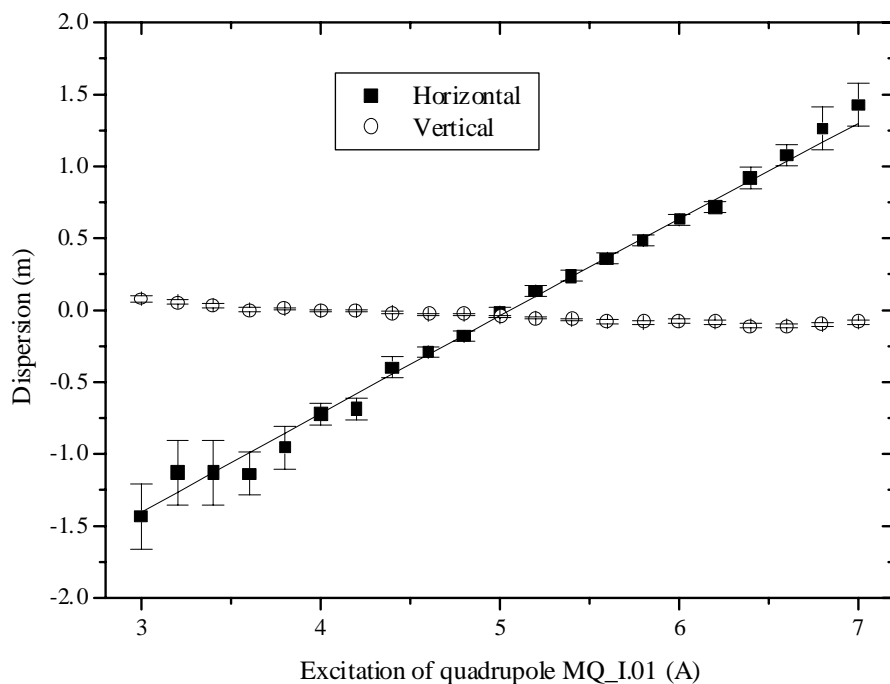


Figure 4.5: Horizontal and vertical dispersions at viewer DCCDFS_I.02 versus the excitation of the quadrupole magnet MQ_I.01. The line graph is a fit of (4.11) to the horizontal dispersion, yielding $D_x(s_0) = -0.418 \pm 0.014$ m and $D_x'(s_0) = 0.134 \pm 0.004$.

pole magnet excitation is equivalent to a reduction of the output energy of the racetrack microtron by 0.77 percent. Therefore, from the shift of the beam profile when the dipole magnet excitation is reduced, one can easily calculate the horizontal and vertical dispersions at the viewer for all excitations of the quadrupole magnet. The resulting dispersions at the viewer are shown in figure 4.5, demonstrating a much larger dispersion in the horizontal plane than in the vertical plane as expected. A fit of (4.11) to the horizontal dispersion (with a reference point at the exit of the bottom 180° dipole magnet in figure 2.1) gives a good agreement with the measured dispersion. However, the determined horizontal dispersion at the reference point is not in agreement with the lattice calculation in figure 2.5, suggesting a non-zero initial dispersion in figure 2.5.

The measured transverse beam sizes as a function of the quadrupole strength are shown in figure 4.6. Unfortunately, the data cannot be modeled satisfactory with the theoretical beam size in (4.10) because the imaging system has a significant minimum resolution which smears the measured beam profiles. Assuming a Gaussian shape of the minimum spot size with a width σ_{res} , the theoretical model (4.10) is modified to

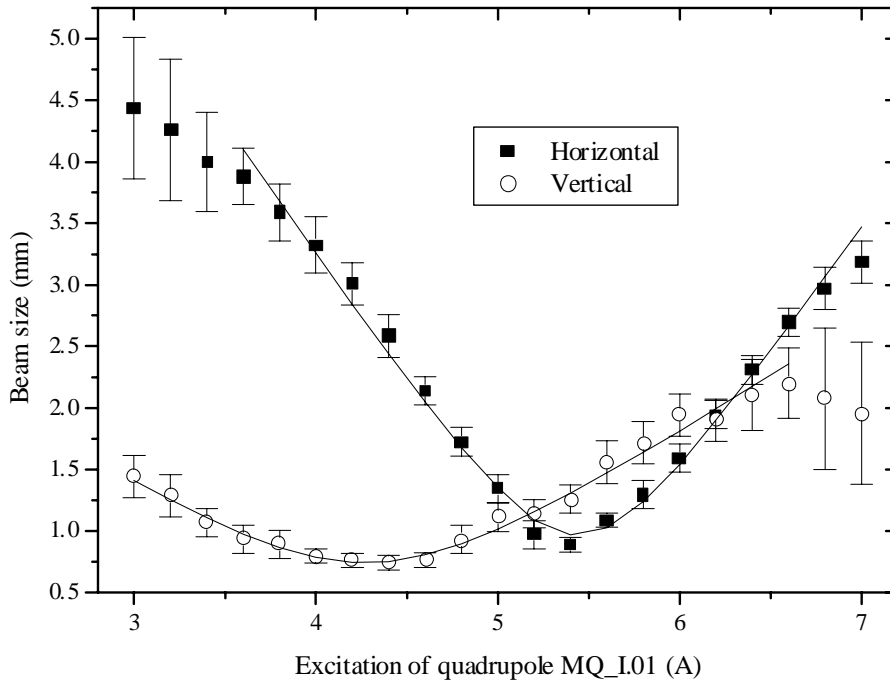


Figure 4.6: Transverse beam sizes (one standard deviation) at viewer DCCDFS_I.02 versus the excitation of the quadrupole magnet MQ_I.01. The line graphs indicate fits of (4.12) to the data for $\sigma_p/p=0.0011$ and $\sigma_{res}=0.6$ mm. The determined fit parameters are $\epsilon_x=0.4\pm0.2$ mm mrad, $\beta_x=10\pm2$ m, $\alpha_x=1.4\pm0.5$, $\epsilon_y=0.6\pm0.4$ mm mrad, $\beta_y=5\pm2$ m, and $\alpha_y=0.0\pm0.4$.

$$\sigma_{tot}(s_1) = \sqrt{\varepsilon \left(R_{11}^2 \beta(s_0) - 2R_{11}R_{12}\alpha(s_0) + R_{12}^2 \frac{1 + \alpha(s_0)^2}{\beta} \right) + (\sigma_p/p_0)^2 D(s_1)^2 + \sigma_{res}^2} \quad , \quad (4.12)$$

where $D(s_1)$ is the measured dispersion in figure 4.5. Unfortunately, the model now has five free parameters while the curve form of the data only justifies three free parameters. Therefore, σ_p/p is chosen to the momentum spread of 0.0011 found in paragraph 4.3 and the resolution of the imaging system is chosen to 0.6 mm as in paragraph 5.6.2. Using these values, the model (4.12) (with a reference point at the exit of the bottom 180° dipole magnet in figure 2.1) is fitted to the data in figure 4.6, providing a horizontal emittance of 0.4 ± 0.2 mm mrad, a vertical emittance of 0.6 ± 0.4 mm mrad, and the lattice functions listed in the caption of figure 4.6. The found vertical lattice functions are in good agreement with the lattice calculation in figure 2.5. However, the horizontal lattice functions are not consistent with those in figure 2.5, which is attributed to a non-ideal setting of the racetrack microtron. In fact, the synchrotron light imaging system which monitors the beam profile provides very limited information about the horizontal envelope of the beam because the synchrotron light is emitted close to the minima of the betatron function in the center of the 180° dipole magnets, impeding an accurate control of the horizontal beam envelope.

The uncertainties of the fit parameters are rather large because the correct value of σ_{res} is somewhat uncertain as the imaging system and the beam properties are not identical to those in paragraph 5.6.2. In addition, a large correlation between the fit parameters makes the fit sensitive to a calibration error of the quadrupole gradient and small measurement errors of the beam size. An additional scan of another quadrupole magnet between the reference point and the viewer would significantly improve the accuracy of the fit parameters because the curve form of the additional scan would provide enough constraints for an accurate determination of all fit parameters.

4.4.3 Determination of the transverse emittances using synchrotron light

Throughout the 180° bend of the main dipole magnets of the racetrack microtron, the electrons emit synchrotron light which is recorded by a CCD camera through a small window in the vacuum chamber (see figure 2.1). As described in paragraph 4.4.2, the camera images are sent to a frame grabber and stored in a computer. Utilizing the CAD drawings of the racetrack microtron, the camera is focused on the source point of the synchrotron light emission (the intersection of the racetrack orbit and the tangent of the orbit passing through the camera) for each racetrack orbit, and the size of each image is calibrated by recording the image of a ruler at the same distance from the camera. Subsequently, the recorded two-dimensional intensity distributions are projected into the horizontal and vertical planes, and the one standard deviation beam size is determined for each plane.

Assuming a Gaussian distribution of betatron amplitudes and a Gaussian momentum distribution of the beam, each transverse beam size is given by (4.10):

$$\sigma_{tot} = \sqrt{\varepsilon\beta + (\sigma_p/p)^2 D^2} \quad . \quad (4.13)$$

Hence, the normalized horizontal emittance ($\beta\gamma\epsilon$, where β and γ are the relativistic beta and gamma factors) can be established if the horizontal beta function, the horizontal dispersion, and the relative momentum spread are known. Using the horizontal beta function and dispersion of the lattice calculation in figure 2.5, the normalized horizontal emittances for the last three recirculations are determined and shown in figure 4.7 for three different absolute momentum spreads. According to the figure, the measurements are most consistent with a conserved normalized emittance (the normalized emittance represents a genuine phase space area) for a relative momentum spread of ~ 0.001 at full energy in good agreement with the value of 0.0011 found in paragraph 4.3. For an momentum spread of 0.0011, the average normalized horizontal emittance is 21 ± 8 mm mrad, equivalent to a horizontal emittance at full energy of 0.21 ± 0.08 mm mrad. Besides, the normalized vertical emittance can be inferred using only the vertical betatron function in figure 2.5 since the vertical dispersion is very close to zero. The result is plotted in figure 4.8, revealing an average normalized vertical emittance of 22 ± 5 mm mrad corresponding to a vertical emittance at full energy of 0.21 ± 0.05 mm mrad. The specified errors of the horizontal and vertical emittances take into account the estimated accuracy of the lattice functions. In particular, the

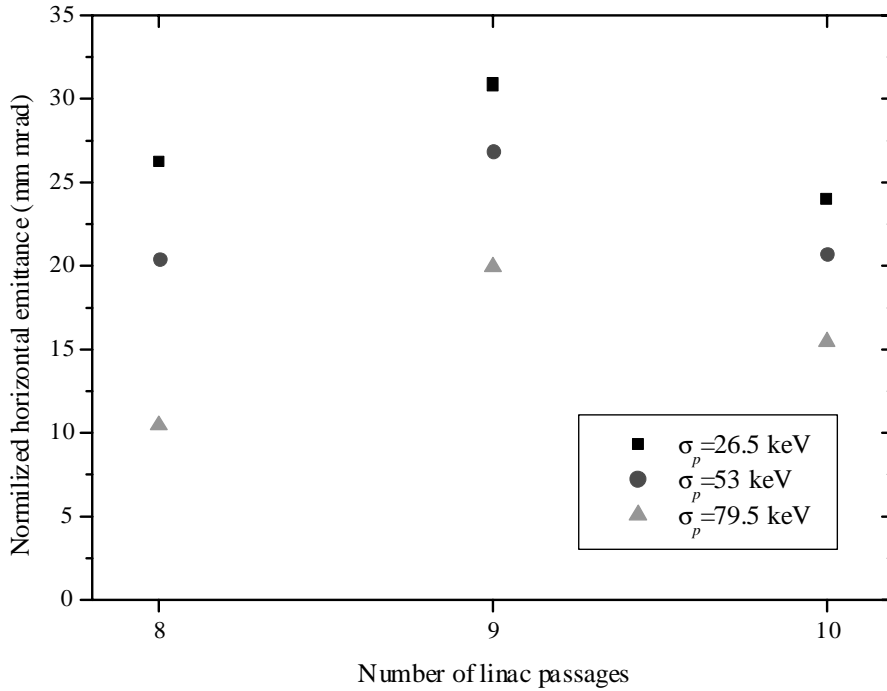


Figure 4.7: Normalized horizontal emittances for the last three recirculations assuming an absolute momentum spread of 26.5 keV/c, 53 keV/c, 79.5 keV/c (corresponds to a relative momentum spread of 0.0005, 0.001, and 0.0015 at full energy).

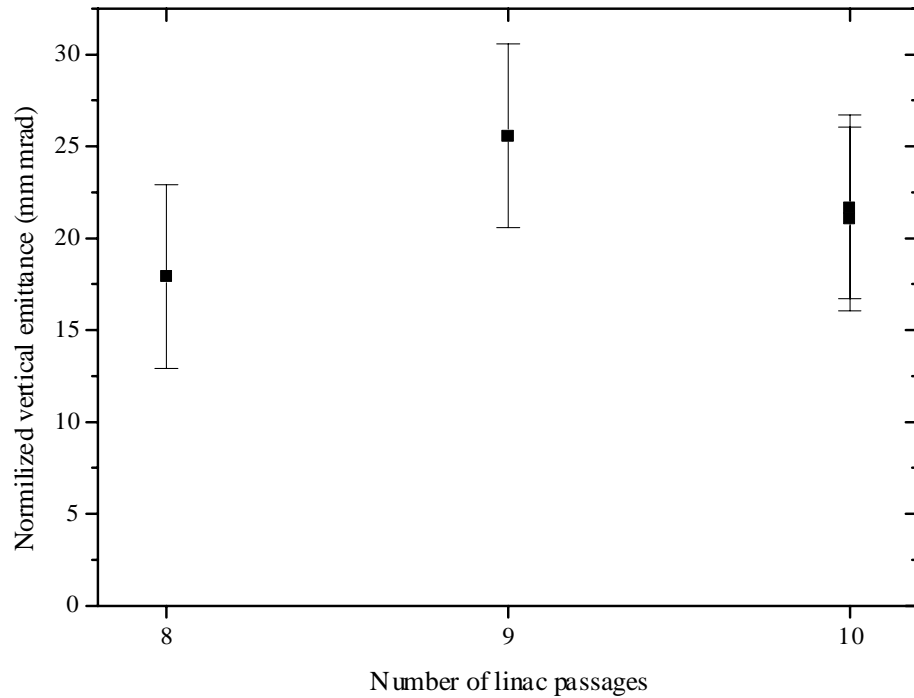


Figure 4.8: Normalized vertical emittance for the last three recirculations.

horizontal beta function is uncertain since only a small displacement of the source point will change the beta function significantly as a result of the narrow minima of the beta function in the center of the 180° dipole magnets (see figure 2.5). The horizontal smearing of the transverse beam profile due to an extended source region of synchrotron light emission can be neglected compared to the actual beam size at the source points (see paragraph E.2).

4.5 Investigation of the longitudinal dynamics

4.5.1 Dependence of the beam current on the generator power

The output beam current of the racetrack microtron is shown in figure 4.9 as a function of the forward rf power transmitted to the linac. For a given amplitude of the accelerating voltage $\Delta E_0/e$, the corresponding forward power is given by (2.15). The forward power is therefore closely linked to the synchronous phase, $\phi_s = \arccos(\Delta E/\Delta E_0)$, where ΔE is the fixed synchronous energy gain of the linac. In particular, the theoretical estimate of the total current as a function of ϕ_s in figure 2.3 suggests that the optimum forward power of 2.46 MW in figure 4.9 corresponds to a synchronous phase of 19° . In addition, the good

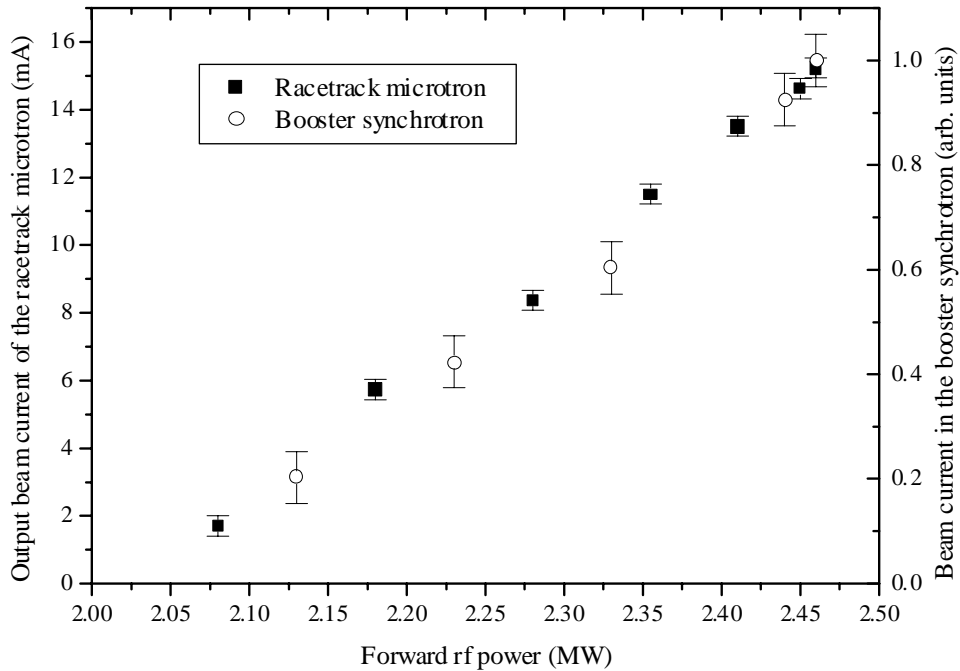


Figure 4.9: Output beam current of the racetrack microtron as a function of the forward rf power. In addition, the associated circulating beam current in the booster synchrotron 1 ms after injection is shown.

qualitative agreement between figure 2.3 and 4.9 indicates that a forward power of ~ 2.00 MW is equivalent to a synchronous phase of zero. However, the change of beam loading balances the change of forward power to some extent. Nevertheless, the effect is small because the total beam current in the linac is dominated by the first few beam passages, which are rather insensitive to the change of forward power. For a forward power exceeding 2.46 MW, the synchronous phase goes beyond the optimum value of 19° , reducing the longitudinal acceptance compared to the maximum acceptance at 19° . As a result, beam loss occurs which further increases the field in the linac due to less beam loading, producing an even larger synchronous phase etc. Consequently, the output beam of the racetrack microtron abruptly disappears for a forward power above 2.46 MW.

4.5.2 Beam current oscillations

If the forward rf power delivered by the generator is reduced with respect to its optimum value, the linac voltage will not match the beam current of the electron gun. The result is a non-stationary solution of the beam current and the linac voltage with an oscillating beha-

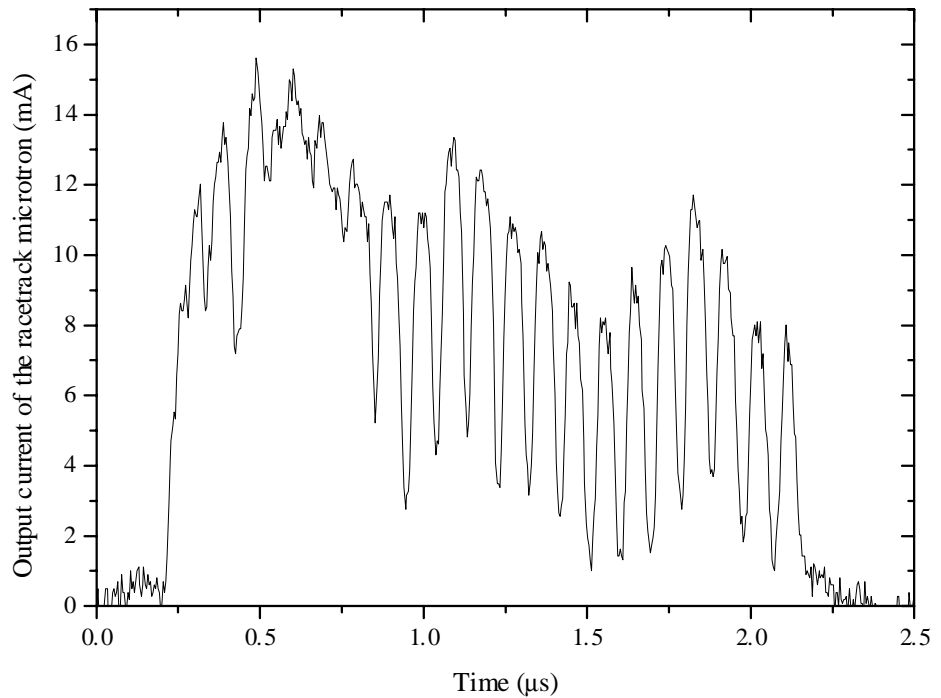


Figure 4.10: Beam current oscillations of the output beam of the racetrack microtron in presence of too low rf voltage.

behavior according to the discussion in paragraph 2.5.1 (negative feedback). An example of the beam current oscillation of the output pulse of the racetrack microtron is shown in figure 4.10. The oscillation period in the figure is 93 ns in good agreement with the discussion of the time constant of the beam-linac feedback mechanism in paragraph 2.5.1. In addition, a measurement of the oscillation period versus the forward power shows a modest increase of only 5 ns when the forward power is decreased from 2.46 MW to 2.08 MW. This is in accordance with a characteristic time scale of the oscillation which is mainly determined by the time constant of linac and the transit time of an electron in the racetrack microtron.

4.5.3 Variation of the momentum spread with the generator power

In figure 4.11 the measurement of the momentum spread, described in paragraph 4.3, is repeated for several values of the forward rf power. It is observed that the momentum spread decreases when the forward power (the synchronous phase) is reduced, in good qualitative agreement with the theoretical prediction in figure 2.4. Even an increase of the momentum spread below a synchronous phase of 10° is observed. However, the absolute size of the measured momentum spread is significantly smaller than expected from the theoretical calculation. The discrepancy is attributed to a significant loss of electrons with

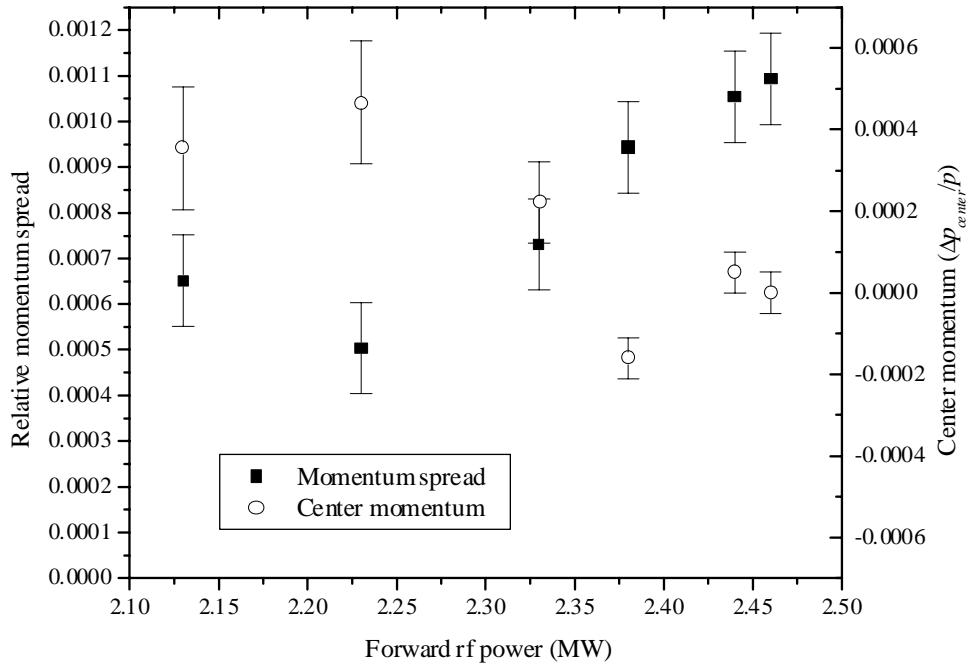


Figure 4.11: Relative momentum spread (one standard deviation) and center momentum of the racetrack microtron beam as a function of the forward rf power.

large momentum deviations during beam recirculation. In particular, beam loss occurs at low energy because the elliptical path of a particular non-synchronous electron in the longitudinal phase space is independent of energy according to (2.6), resulting in a huge relative momentum spread at low energy and therefore a very large horizontal beam size in the presence of a finite dispersion. As a consequence, electrons with large momentum deviations are lost on physical or dynamical apertures at low energy. In addition, electrons with large momentum deviations may dominate the beam loss during the injection process in the booster synchrotron due to the large horizontal displacement of the beam, resulting in an underestimation of the actual momentum spread of the racetrack microtron beam. However, the very similar dependence of the output beam current of the racetrack microtron and that of the circulating current in the booster synchrotron as a function of the forward power in figure 4.9 strongly suggests that the momentum distribution of the beam is not altered by the injection process.

Furthermore, an analysis of the momentum distribution reveals that the maximum beam current per unit momentum interval is almost independent of the forward power down to 2.20 MW since the reduction of the total beam current is balanced by the smaller momentum spread. This is in good agreement with the theoretical calculation in figure 2.3. Finally, it is observed in figure 4.11 that the center momentum of the racetrack microtron

beam only has a very moderate dependence on the forward power in reasonable accordance with the theoretical simulation in figure 2.4.

4.6 The performance of the ANKA racetrack microtron

4.6.1 Comparison with other racetrack microtrons

The most important measured beam properties of the ANKA racetrack microtron are listed in table 2.1 together with the design values, revealing that the racetrack microtron performs according to specifications or better. In addition, the beam properties of the ANKA racetrack microtron are compared with other racetrack microtrons in table 4.1. According to the table, the output current of the ANKA racetrack microtron is similar to that of the other racetrack microtrons. However, the output current of the Stockholm and Lund racetrack microtrons are somewhat higher (at 53 MeV the beam current of the Lund racetrack microtron exceeds the value specified in the table). An appropriate choice of coupling coefficient between the waveguide and the linac of the Stockholm and Lund racetrack microtrons is likely to contribute to the better performance. In addition, the output beam current of the Lund racetrack microtron has been enhanced by means of a pre-buncher working at the fundamental frequency of the rf system [6].

In the literature, there exists surprisingly few measurements of the transverse emittances and the momentum spread of the output beam of racetrack microtrons. In fact, in the table only the Lund and Scanditronix racetrack microtrons have published data for the transverse emittances and the momentum spread. The normalized horizontal emittance of the Scanditronix racetrack microtron is in good agreement with that of the ANKA racetrack microtron whereas the normalized vertical emittance of ANKA racetrack microtron is considerable smaller than those of the Lund and Scanditronix racetrack microtrons. The relative momentum spread of the ANKA racetrack microtron is also superior to that of the Scanditronix racetrack microtron as the absolute momentum spread ideally is constant during the recirculation. Finally, all racetrack microtrons are able to produce an electron pulse with a duration in excess of 1 μ s.

4.6.2 Comparison with the performance of linear accelerators

In table 4.1 are also listed the main beam parameters of selected modern linear accelerators at European synchrotron radiation facilities. All the linear accelerators are able to produce peak currents well above 100 mA in single bunch operation as a result of their large longitudinal acceptance. This is far above the capability of the ANKA racetrack microtron. However, the average output current of the linear accelerators decrease dramatically with the pulse length due to beam loading effects. In fact, for a pulse length of about 0.5 μ s, which is appropriate for the multi-turn injection process of the ANKA booster synchrotron, the average beam current of the ANKA racetrack microtron is higher than that of most of

Experimental investigation of the ANKA racetrack microtron

the linear accelerators. In addition, the table reveals that the ANKA racetrack microtron has smaller transverse emittances and momentum spread than the linear accelerators which is important in the present application since the efficiency of the multi-turn injection process decreases for a large transverse beam size of the injected beam. The rather small momentum spread of the ANKA racetrack microtron is a consequence of the recirculation of the beam which preserves the momentum spread characteristic of a single linac passage, causing the relative momentum spread to decline inversely with the number of linac passages (see paragraph 2.3.1). In addition, the recirculation of the beam makes the beam momentum insensitive to power fluctuations from the rf generator as demonstrated by the measurements in figure 4.11 for which the amplitude of the linac field is changed by almost 6 percent. On the other hand, the momentum of linear accelerators is directly linked to the amplitude of the rf field, making the momentum and the momentum spread very sensitive to the stability of the rf generator and beam loading of the accelerating field.

Table 4.1: Measured beam properties of selected racetrack microtrons (rtm) and linear accelerators.

	Max. Beam energy (MeV)	Beam current (mA)	Bunch train charge (nC)	Norm. emittance (hor./ver.) (mm mrad)	Relative momentum spread	Max. pulse length (μ s)
ANKA rtm	53	15		21/21	0.0011	1.7
Stockholm rtm [7]	50	30				5
BESSY II rtm [8]	50	15				1
Aarhus rtm	100	11				1
Lund rtm [9,10]	100	20		/45		1
Scanditronix rtm [11]	100	15		20/39	0.001	1.2
SLS linac ^a [12]	102		2.0	50	0.002	
SLS linac ^b [12]	103		2.2	40	0.003	0.5
ESRF linac ^a [13]	200	250		200	0.005	
ESRF linac ^b [13]	200	25		200	0.001	1
ELETTRA linac ^b [14]	1100	30			0.005	0.07
DELTA linac ^a [15]	75		0.36	<120	0.0021	
DELTA linac ^b [15]	75					0.09

^aSingle bunch operation.

^bMultiple bunch operation.

Besides its high quality beam properties, the racetrack microtron is also attractive because the recirculation causes the accelerator to be much smaller than a linear accelerator

with the same beam energy. In addition, the recirculation ensures an effective conversion of rf power into beam power, reducing the investment in rf power sources in comparison with linear accelerators. The construction and operation expenses of racetrack microtrons are thus usually less than those of linear accelerators. Racetrack microtrons are therefore in many respects superior to linear accelerators as injectors for booster synchrotrons.

4.6.3 Improvements of the ANKA racetrack microtron

In presence of regenerative beam breakup, the growth time of the destructive HEM_{11} mode is expected to be about $1 \mu\text{s}$ (see paragraph 2.5.2). Since no decrease of the beam current throughout the electron pulse is observed, the output beam current of the racetrack microtron is not believed to be influenced by regenerative beam breakup. On the other hand, the output beam current of the ANKA racetrack microtron is likely to be limited by a beam-linac feedback instability when the optimum coupling coefficient between the waveguide and the linac exceeds the actual coupling coefficient (see discussion in paragraph 2.5.1 and 4.2.2). As a consequence, an output beam current significantly above 15 mA cannot be expected. According to (2.16), the beam current threshold for the beam-linac feedback instability can be doubled by increasing the coupling coefficient from 3 to 5. This also increases the threshold current for regenerative beam breakup [16]. The higher coupling coefficient requires more generator power for the same beam current due to more reflected power from the linac, but this should not cause any problems since the generator is capable of producing an output power of 6 MW. At the same time, it would be advantageous to exchange the combined 3 GHz oscillator and amplifier to a more reliable design because its tubes have a limited lifetime, resulting in a decline of the output power of the klystron. In fact, more than a 50 percent decline of the output of the oscillator was observed within the first half year of operation. Alternatively, the onset current of the beam-linac feedback instability can be enlarged by increasing $\Delta E/R$, using higher generator power and lower shunt impedance.

A higher output beam current can also be realized by installing a pre-buncher, operating at the fundamental rf frequency, in the injection transfer line of the racetrack microtron. The pre-buncher would enhance the output current because more electrons are injected into the longitudinal acceptance of the rf system without increasing the average beam current in the linac which determines the beam loading and the onset of the beam-cavity instabilities. This modification of the racetrack microtron requires a new low-level rf system which can be synchronized with the pre-buncher, making the improvement somewhat expensive. In addition, the running-in of the racetrack microtron will become more complicated. However, a pre-buncher is the ideal approach for achieving a high output beam current and a low beam loss during recirculation.

At present, most vacuum chamber components of the racetrack microtron are assembled by o-ring type vacuum seals. Unfortunately, the o-rings are susceptible to radiation damage, resulting in vacuum problems. In particular, the large o-rings between the poles of

the 180° dipole magnets and the walls of the dipole magnet vacuum chambers are problematic because the magnets have to be disassembled in order to exchange the o-rings. Although, radiation resistant o-rings have increased the lifetime of the o-rings, the reliability of the racetrack microtron would profit if a separate vacuum chamber is installed inside the dipoles magnets and full-metal vacuum seals are employed everywhere. The improvements increase the cost of microtron, but they are a modest investment for obtaining a more reliable machine which needs less service. It would also be advantageous to exchange the present three beam viewers with a single horizontally-moving viewer which can be positioned in all racetrack orbits. In particular, this would improve the diagnostics of the horizontal beam envelope compared with the present synchrotron light imaging system which suffers from the minima of the horizontal betatron function in the center of the 180° dipole magnets. In addition, the running-in time of the machine can be reduced if remote controls of the linac position and the distance between the 180° dipole magnets are implemented.

References:

- [1] R. Talman, *Beam Current Monitors*, AIP Conf. Proc. **212**, p. 1 (1990)
- [2] J. Le Duff, *Longitudinal Beam Dynamics in Circular Accelerators*, in Proc. of Fifth General Accelerator Physics Course, CERN Accelerator School, Jyväskylä, Finland, 1992, edited by S. Turner (CERN, Geneva, 1994), p. 289
- [3] K. T. McDonald and D. P. Russell, *Methods of Emittance Measurement*, in Proc. Frontiers of Particle Beams; Observation, Diagnosis and Correction, Capri, 1988, edited by M. Month and S. Turner (Lecture Notes in Physics **343**, Springer-Verlag, Berlin, 1989), p. 122
- [4] J. Buon, *Beam Phase Space and Emittance*, in Proc. of Fifth General Accelerator Physics Course, CERN Accelerator School, Jyväskylä, Finland, 1992, edited by S. Turner (CERN, Geneva, 1994), p. 89
- [5] J. Rossbach and P. Schmüser, *Basic Course on Accelerator Optics*, in Proc. of Fifth General Accelerator Physics Course, CERN Accelerator School, Jyväskylä, Finland, 1992, edited by S. Turner (CERN, Geneva, 1994), p. 17
- [6] M. Eriksson, Nucl. Instr. and Meth. **196**, p. 331 (1982)
- [7] S. Rosander, M. Sedlacek and O. Wernholm, Nucl. Instr. and Meth. **204**, p. 1 (1982)
- [8] M. Abo-Bakr *et al.*, in Proc. European Part. Acc. Conf., Barcelona, 1996, p. 527
- [9] M. Eriksson, Nucl. Instr. and Meth. **A261**, p. 39 (1987)
- [10] M. Georgsson, in Proc. European Part. Acc. Conf., Stockholm, 1998, p. 1512
- [11] P. Lidbjörk and J. Åström, in Proc. Part. Acc. Conf., Washington, D. C., 1993, p. 2068
- [12] M. Pedrozzi *et al.*, in Proc. European Part. Acc. Conf., Vienna, 2000, p. 851

Chapter 4

- [13] Project team, in Proc. Part. Acc. Conf., Washington, D. C., 1993, p. 1427
- [14] G. D'Auria *et al.*, in Proc. Part. Acc. Conf., Vancouver, 1997, p. 1212
- [15] A. Jankowiak *et al.*, in Proc. European Part. Acc. Conf., Vienna, 2000, p. 634
- [16] W. J. G. M. Kleeven *et al.*, in Proc. European Part. Acc. Conf., Berlin, 1992, p. 813

Chapter 5

Experimental investigation of the ANKA booster synchrotron

5.1 Introduction

The ANKA booster synchrotron was assembled and tested at Forschungszentrum Karlsruhe in April-May 1999 following the commissioning of the ANKA racetrack microtron. Immediately hereafter, the running-in of the booster synchrotron proceeded until the beginning of December 1999 (with several stops due to the installation of the ANKA storage ring) at which point a circulating current of 10 mA routinely was accelerated to a beam energy of 500 MeV and subsequently extracted from the booster synchrotron. The final commissioning of the booster synchrotron was carried out in the end of February 2000. Here all important accelerator and beam parameters were demonstrated to fulfil or exceed the design values.

5.2 Investigation of the lattice of the booster synchrotron

5.2.1 Transverse tunes and lattice functions

The horizontal and vertical tunes, Q_x and Q_y , respectively, of the booster synchrotron are determined by measuring the frequency spectrum of the horizontal and vertical difference signals of all four striplines at the stripline unit DSL_B.02 by a spectrum analyzer, while the betatron oscillation of the beam is excited by the other stripline unit DSL_B.01. During a measurement, the excitation frequency is controlled by a swept-frequency generator which is synchronized with the spectrum analyzer. The excited coherent betatron oscillation of the beam gives rise to peaks in the recorded spectrum at

$$\begin{aligned} (pM + \mu + Q)f_{rev} & , \quad p \geq 0 \\ (pM - \mu - Q)f_{rev} & , \quad p > 0 \end{aligned} \quad (5.1)$$

where p is an integer, M is the number of bunches, $\mu=0,1,2,\dots,M-1$ is the mode index of the

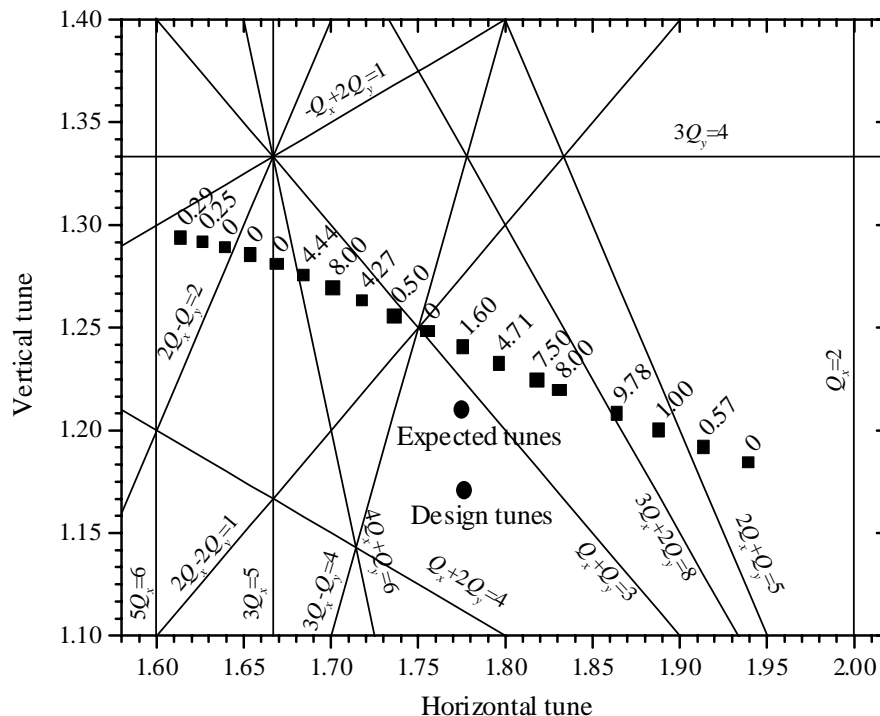


Figure 5.1: Transverse tunes of the booster synchrotron at the injection energy (53 MeV) for several different excitations of the quadrupole magnets. For each value of the excitation, the corresponding circulating current 100 ms after injection is indicated (the beam current is the maximum value after ~ 15 minutes of optimization). The design working point and the expected working point are also shown (the latter takes into account the actual position and the field mapping of all magnetic elements). Finally, all significant betatron resonance lines are indicated.

M coherent transverse modes of the beam, Q is the transverse tune, and f_{rev} is the revolution frequency of the booster synchrotron [1]. Hence, the peak positions immediately provide the fractional part of the transverse tune whereas the integer part can be inferred from the beam position at the viewers during the first roundtrip of the beam.

The measured transverse tunes at the injection energy for several different excitations of the quadrupole magnets are shown in the tune diagram in figure 5.1. It is observed that the working line is fairly close to the expected tunes while it deviates significantly from the design tunes due to an insufficient knowledge of the magnetic elements in the design phase (see paragraph 3.2.1). The deviation from the expected working point can be explained by an angle error of 0.3 degrees of the effective field boundary of the dipole magnets or a small vertically-focusing quadrupole gradient of $9.8 \cdot 10^{-4}$ T/m in the dipole magnets, again demonstrating that the limited tune flexibility causes a large sensitivity towards non-ideal

magnetic elements. In the remaining analysis of the booster synchrotron, lattice calculations assume an angle error of 0.3 degrees of the effective field boundary of the dipole magnets in order to reproduce the measured tunes (the lattice input file is provided in appendix C). At full excitation, the static working point is expected to differ from its position at the injection energy owing to the rectangular shape of the iron block of the dipole magnets which due to the relatively small bending radius of the magnet gives rise rather different widths of the two return yokes in the center of magnet and at the pole-ends. The result is a finite quadrupole component at these locations at full excitation due to a larger saturation of the thin return yoke. Fortunately, the sign of the quadrupole component is opposite in the center and at the end-poles, reducing the effective quadrupole component somewhat.

Knowing the shift ΔQ of the transverse tune for a given change of the strength of the quadrupole magnets Δk , the beta function can also determined. Adopting the thin lens approximation for the quadrupole magnets, the average beta function at the quadrupole magnets is given by

$$\beta_q = \pm \frac{2}{\Delta k L_q} \{ \cot(2\pi Q)(1 - \cos(2\pi \Delta Q)) + \sin(2\pi \Delta Q) \} , \quad (5.2)$$

where the \pm sign refers to the horizontal and vertical planes, respectively, and L_q is the length of the quadrupole magnets [2]. Applying the expression to the working point (1.827,1.223) in figure 5.1, the horizontal and vertical beta functions at the quadrupole

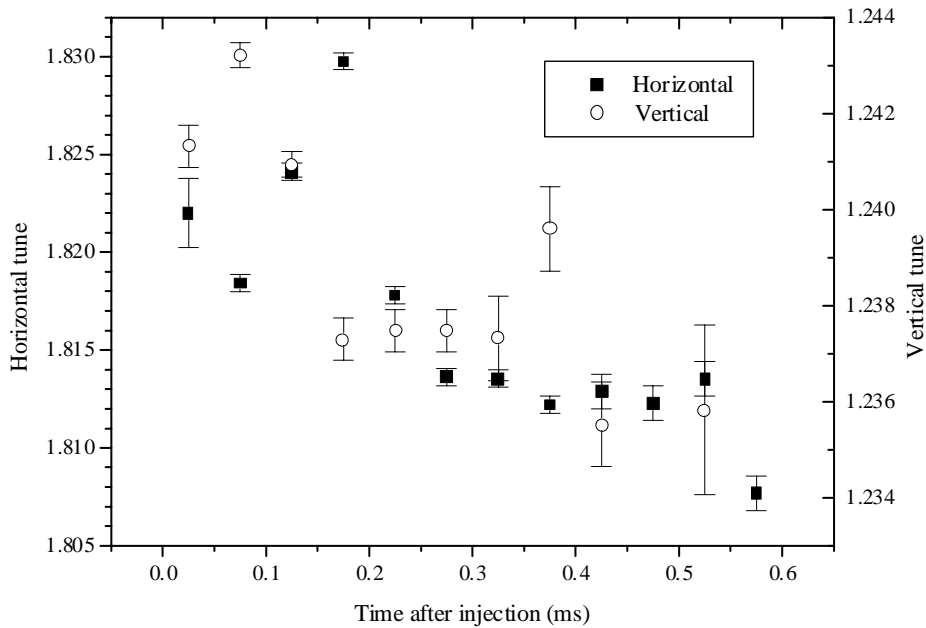


Figure 5.2: Transverse tunes during the beam acceleration.

magnets are found to be 8.5 ± 0.3 m and 2.8 ± 0.4 m, respectively. A lattice calculation yields horizontal and vertical beta functions of 8.2 m and 2.4 m at the quadrupole magnets, respectively, in good agreement with the measured values.

For each point on the working line in figure 5.1, the circulating current in the booster synchrotron 100 ms after injection is also indicated. It is observed that the second and third order resonances $2Q_x - Q_y = 2$, $3Q_x = 5$, $Q_x + Q_y = 3$, and $2Q_x + Q_y = 5$ (possibly also the fourth order resonances $2Q_x - 2Q_y = 1$ and $3Q_x - Q_y = 4$) are harmful to the beam whereas the fifth order resonances $4Q_x + Q_y = 6$ and $3Q_x + 2Q_y = 8$ do not cause any harm to the beam. Furthermore, the beam current declines above $Q_x = 1.93$ as the size of the horizontal beta function increases dramatically (the lattice is not closed in the horizontal plane for $Q_x > 2$).

The transverse tunes can also be determined at a specific time during beam acceleration by performing a spectral analysis which is much faster than the dynamic change of the tunes. The resulting transverse tunes throughout the whole beam acceleration are shown in figure 5.2, and the associated ramping curve is plotted in figure 5.3. The maximum horizontal and vertical tune variations are 0.022 and 0.007, respectively, demonstrating a good control of the transverse tunes by the individual ramping curve for the quadrupole magnets.

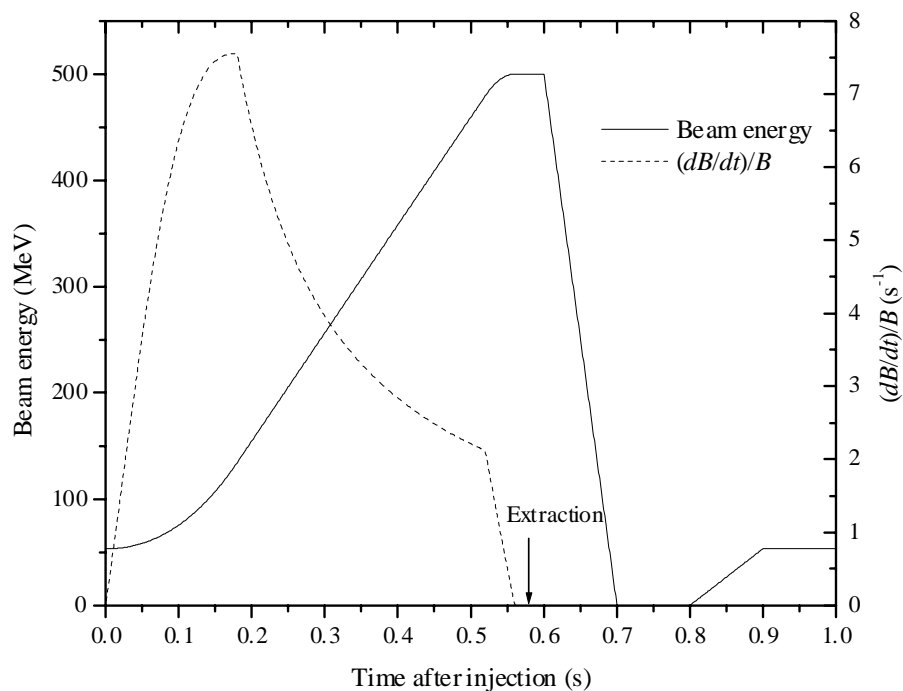


Figure 5.3: Energy ramping curve of the booster synchrotron throughout the complete one-second cycle of the injector. The relative ramping speed in terms of $(dB/dt)/B$ is also plotted, where B is the strength of the bending field.

The smooth shape of the ramping curve is necessary for an accurate control of the tunes since the dipole and quadrupole magnet power supplies do not produce well-defined currents in presence of an abrupt change of the ramping curve.

5.2.2 Closed orbit deviations

The transverse position of the beam in the booster synchrotron is determined by means of the button pickup units, each consisting of four buttons. These beam position monitors (bpms) are distributed uniformly over the circumference of the booster synchrotron (DBPM_B.01-8 in figure A.1). The bpms can be sampled at 1 kHz, providing dynamic information about the beam position. For example, the horizontal and vertical closed orbit deviations throughout the ramping of the beam energy are plotted in figure 5.4 and 5.5, respectively. It is observed that the horizontal closed orbit deviation at injection is about a factor of two larger than the expected maximum deviation of ± 3 mm, arising from the tolerance of the integrated field of the dipole magnets (see paragraph 3.2.4). The disagreement is partly caused by the shift of the working line found in paragraph 5.2.1, giving rise to both a larger horizontal tune and beta function which results in a ~ 50 percent larger maximum closed orbit deviation according to (3.5). In addition, the non-linear properties of the bpms

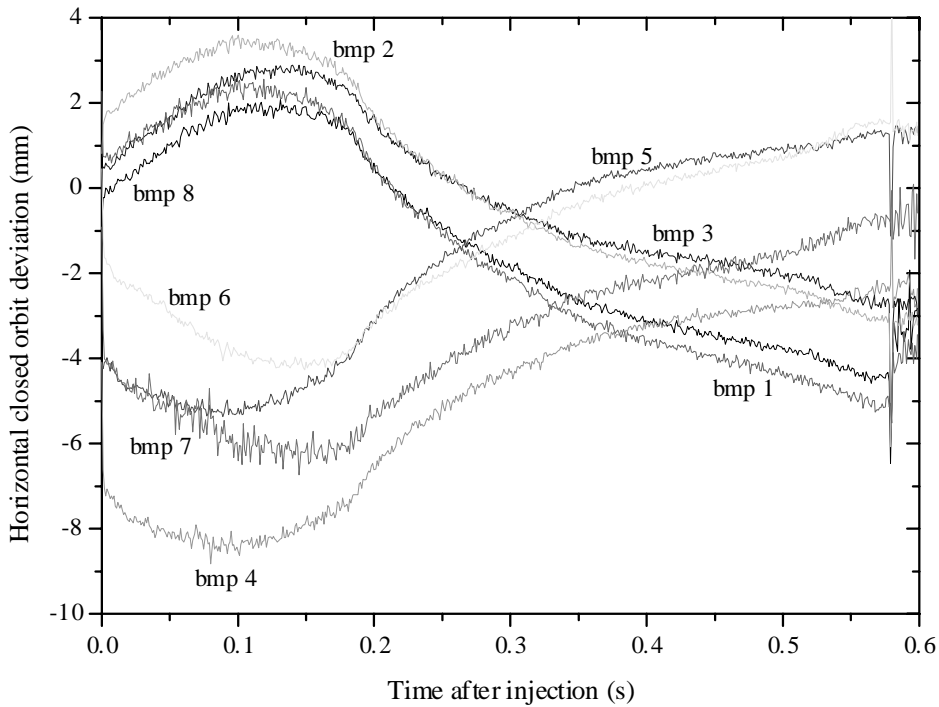


Figure 5.4: Horizontal closed orbit deviation during ramping of the beam energy (the bpm positioning tolerance is about 2 mm).

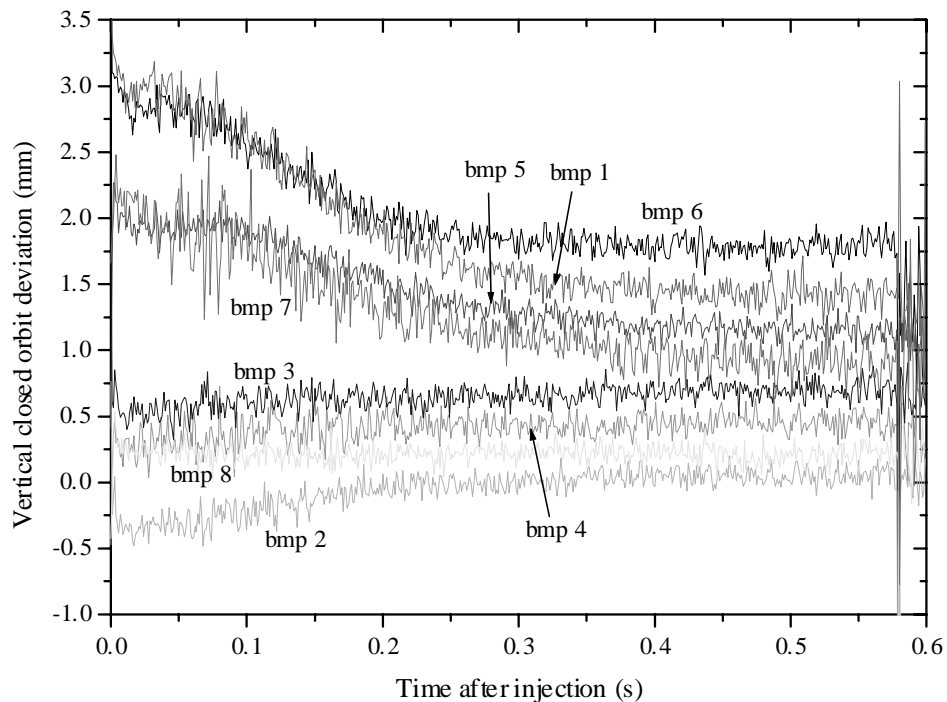


Figure 5.5: Vertical closed orbit deviation during ramping of the beam energy (the bpm positioning tolerance is about 2 mm).

may lead to an overestimation the closed orbit deviation due to the large horizontal beam size following the injection. After the injection, the horizontal closed orbit deviation increases ~ 2 mm with a maximum after ~ 150 ms. The resemblance to the relative ramping speed in figure 5.3 suggests that this behavior is caused by eddy currents in the walls of the dipole magnet vacuum chamber or in the iron yoke and coils of the dipole magnet itself. For the maximum beam energy of 500 MeV (>560 ms after injection), the horizontal closed orbit deviation is about ± 3 mm in agreement with a smaller tolerance of the integrated bending field at full excitation compared with that at 10 percent excitation. The vertical closed orbit deviation is only about ± 1.5 mm. This is far below the required ± 10 mm, demonstrating that the alignment tolerance of the rotation of the dipole magnets around the beam axis is much smaller than the required 0.2 mrad.

5.2.3 Chromaticity

For a bunched beam, the total orbit length is an integer number of rf wavelengths. According to the definition of the momentum compaction factor α_p , a shift of the rf frequency thus gives rise to a corresponding shift of the relative average beam momentum of

$$\frac{\Delta p}{p} = -\frac{1}{\alpha_p} \frac{\Delta f_{rf}}{f}, \quad (5.3)$$

where f_{rf} is the rf frequency. Therefore, the chromaticity, $\xi = \Delta Q / (\Delta p/p)$, can be determined by measuring the tune variation as a function of the rf frequency. The found horizontal and vertical static chromaticities at the injection energy are 2.27 ± 0.17 and -11 ± 1 , respectively. The corresponding values of a lattice calculation are -0.40 and -2.89 for the horizontal and vertical planes, respectively. The large disagreement is attributed to a finite curvature of the effective field boundary at the end-poles of the dipole magnets equivalent to a significant positive sextupole component. The curvature is a consequence of an optimization of the effective field boundary at full excitation, compensating the saturation of the return yokes at the end-poles of the magnet by increasing the mechanical length the magnet off-axis. In addition, the effect is amplified by the rectangular shape of the iron block which makes the inner return yoke at the end-poles more susceptible to saturation, resulting in somewhat different shapes of the effective field boundary at low and high excitation of the dipole magnets. The measured static chromaticities can almost be reproduced within the uncertainties by a lattice calculation if a sextupole with an integrated strength of 0.105 T/m is added at each end-pole of the dipole magnets. This sextupole strength corresponds to a change of the angle of the effective field boundary of only 0.3 degrees 10 mm off-axis, emphasizing the need for a very accurate field mapping of the fringe field of the dipole magnets. The small disagreement with the lattice calculation is ascribed to the significant sextupole component of the window frame corrector magnets.

The chromaticities are also determined during the ramping of the beam energy by carrying out tune measurements as those in figure 5.2 for two different rf frequencies. The horizontal and vertical chromaticities found throughout the whole ramp are shown in figure 5.6. The significant variation of the chromaticities during ramping is attributed to the variation of the static chromaticities with the excitation of the dipole magnets and the sextupole field generated by the eddy currents in walls of the dipole magnet vacuum chamber (see paragraph 3.4.2 and appendix D). Using (3.20)-(3.23) and assuming a linear dependence of the static chromaticity on the strength B of the bending field, the expected chromaticity shift is

$$\Delta \xi = \xi_{inj} + \alpha(B - B_{inj}) + \lambda K \frac{dB/dt}{B}, \quad (5.4)$$

where ξ_{inj} is the static chromaticity at the injection energy, α accounts for the linear variation of the static chromaticity as a function of the bending field, B_{inj} is the strength of the bending field at injection, and $\lambda = m_{eddy} B / (dB/dt)$. Performing fits of the model (5.4) to the measured chromaticities in figure 5.6, one obtains $\xi_{inj,x} = 1.97 \pm 0.12$, $\alpha_x = -1.52 \pm 0.14$, $\lambda = 0.0793 \pm 0.008$ and $\xi_{inj,y} = -11.6 \pm 0.6$, $\alpha_y = 8.6 \pm 1.0$, $\lambda = 0.0747 \pm 0.015$ for the horizontal and

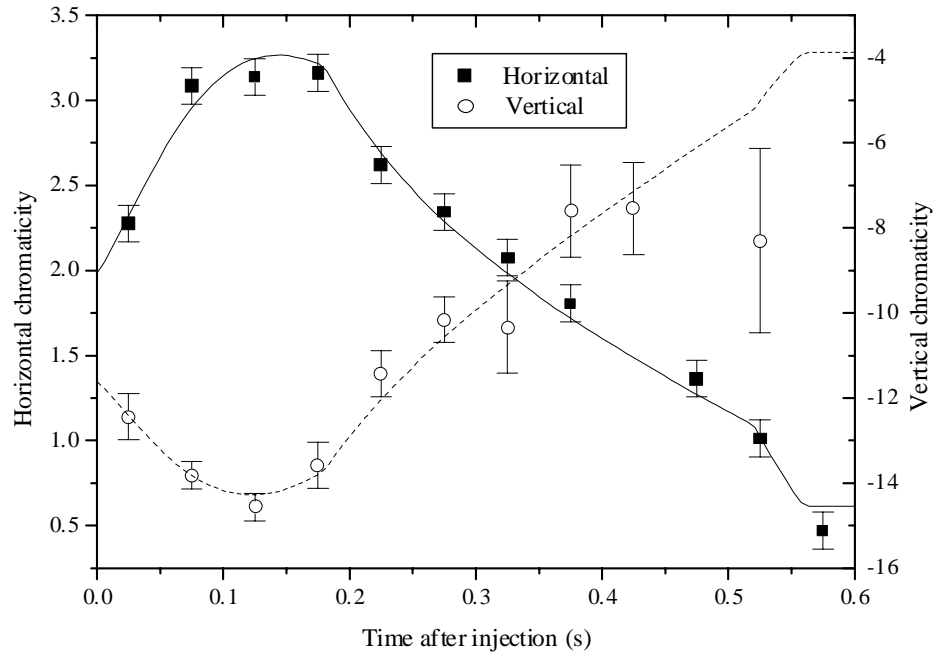


Figure 5.6: Horizontal and vertical chromaticities throughout ramping of the beam energy. The line graphs are fits of (5.4) to the measured chromaticities.

vertical planes, respectively. The good agreement between the measured chromaticities and the model demonstrates that the shifts of the chromaticities indeed are strongly influenced by eddy-currents in the walls of the dipole magnet vacuum chamber. In addition, the accurate modeling of the data suggests that a linear model for the static chromaticity is a good approximation. This is also confirmed by the good agreement with the static measurements of the chromaticity at the injection energy above. Furthermore, the horizontal and vertical static chromaticities found at full excitation of 0.61 and -3.9, respectively, reveals that the curvature of the effective field boundary at the end-poles of the dipole magnets is much smaller at full excitation than at low excitation as expected.

The values of λ associated with the horizontal and vertical chromaticities, respectively, differ more than can be justified from the uncertainties. The disagreement is ascribed to small deviations of the static chromaticity from a linear behavior, the sextupole strength of the corrector magnets, and eddy currents in the coils and iron yokes of the dipole and quadrupole magnets. Assuming that the presence of all magnetic materials nearby the rectangular vacuum chamber inside the dipole magnets can be neglected, $\lambda=0.046$ according to (3.20) (the values of all parameters in (3.20) are given in paragraph 3.4.2). On the other hand, in the limit the vacuum chamber is much wider than the pole gap, $\lambda=0.109$ according to (3.21). A comparison with the experimental value of λ reveals that λ is underesti-

mated if the presence of the magnetic materials is neglected. This is not surprising since the iron yoke of the dipole magnet is expected to amplify the eddy current-induced sextupole field. In contrast, λ is overestimated if the vacuum chamber is assumed to be much wider than the pole gap. In fact, the average value of (3.20) and (3.21) is very close to the measured value of λ . This interpretation of (3.20) and (3.21) is a general behavior which is applicable for all rectangular vacuum chambers.

5.2.4 Momentum compaction factor

If the rf system of the booster synchrotron is turned off and the cavity is detuned far from the 44th harmonic of the revolution frequency, the circulating beam will not interact with the cavity. In this case, a small change of the bending field produces a shift of the revolution frequency which is given by

$$\frac{\Delta f_{rev}}{f_{rev}} = \alpha_p \left(\frac{\Delta B}{B} - \frac{\Delta p}{p} \right) = \alpha_p \left(\frac{\Delta I}{I} - \frac{\Delta p}{p} \right), \quad (5.5)$$

where the last term assumes an ideal linear dependence of the bending field B on the excitation current I , f_{rev} is the average revolution frequency, p is the average electron momentum,

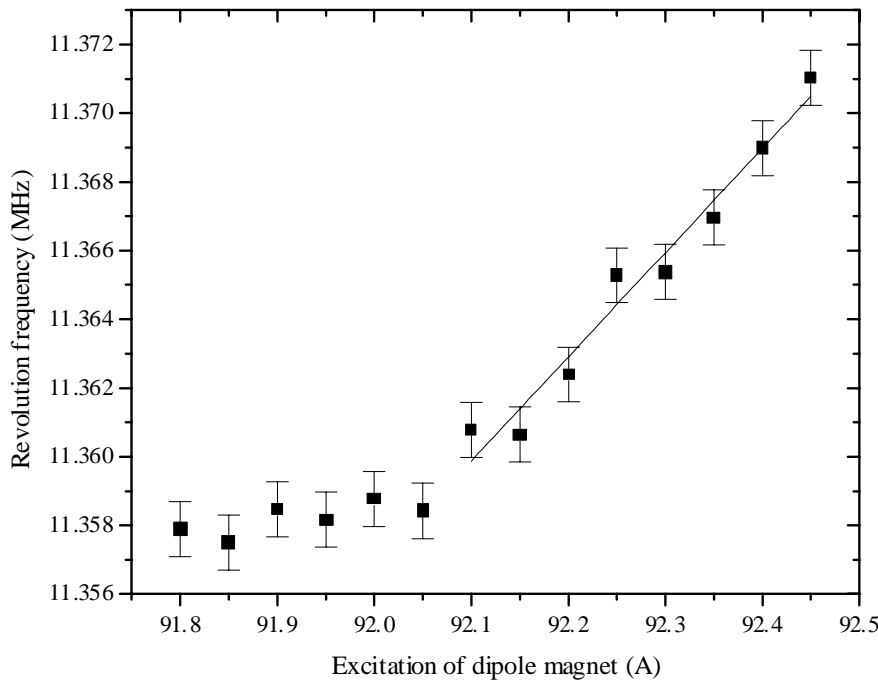


Figure 5.7: Revolution frequency 10 ms after injection (no ramping) as a function of the excitation of the dipole magnets. The line graph is a fit of (5.5) with $\Delta p/p=0$ to the data.

and α_p is the momentum compaction factor [3]. Hence, if the average electron momentum is fixed, the momentum compaction factor can be determined by measuring the revolution frequency as a function of the excitation of the bending magnets. In order to implement this technique for the booster synchrotron, a stripline signal from the stripline unit DSL_B.02 is feed into a spectrum analyzer and the revolution frequency of the circulating beam is determined only 10 ms after injection since the beam rapidly is lost owing to the synchrotron radiation-induced energy loss. The resulting dependence of the revolution frequency on the dipole magnet excitation is shown in figure 5.7. The deviation from the expected linear behavior for excitations below 92.1 A is attributed to a significant loss of electrons with large momenta during injection (the decrease of B is balanced by a decrease of p). A fit of (5.5) with $\Delta p/p=0$ to the data above an excitation of 92.1 A yields a momentum compaction factor of 0.246 ± 0.018 in good agreement with a lattice calculation which produces a value of 0.252. Figure 5.7 displays a linear behavior of the revolution frequency over at least ~ 12 kHz which is equivalent to a span of relative momentum of $\sim 4 \cdot 10^{-3}$ in which all electrons experience the same injection efficiency. This suggests that the measurement of the momentum spread in paragraph 4.3 is not influenced by the limited momentum acceptance of the booster synchrotron.

The technique for measuring the momentum compaction factor presented above can also be utilized for circular electrons accelerators with considerable higher injection energies if the beam signal is recorded with an oscilloscope shortly after the injection, before the beam is lost due to synchrotron light emission. Subsequently, the revolution frequency can be determined from a harmonic of the revolution frequency in the FFT spectrum of the beam signal.

5.3 Properties of the electron beam

5.3.1 Beam current and lifetime

Figure 5.8 shows the circulating beam current for both normal and dc operation of the booster synchrotron. According to the figure, it is possible to inject a beam current of more than 30 mA and subsequently accelerate a beam current of more than 10 mA to the full beam energy of 500 MeV, exceeding the design goals in table 3.1.

The beam current traces in figure 5.8 also provide information about the lifetime of the beam. In fact, the decay constant of the beam is $-(dI_b/dt)/I_b$, where I_b is the beam current. The found decay constants for both normal and dc operation of the booster synchrotron are shown in figure 5.9. After a substantial beam loss the first ~ 100 ms after the injection process, the decay constant associated with dc operation approaches an asymptotic value of $\sim 1.6 \text{ s}^{-1}$ equivalent to a lifetime of ~ 0.6 s. Measurements of the asymptotic lifetime for various residual gas pressures demonstrates that the asymptotic lifetime is approximately proportional to the residual gas pressure, suggesting that the asymptotic lifetime is domi-

nated by elastic scattering of the electrons on the residual gas (the cross section for inelastic scattering can be neglected). For a relativistic electron beam, the elastic scattering decay constant is approximately given by

$$\tau^{-1} = 2\pi n \frac{r_e^2 Z^2 c}{\gamma^2} \frac{\langle \beta \rangle}{(A^2/\beta_A)_{\min}}, \quad (5.6)$$

where $n=7.24 \cdot 10^{24} n_Z \cdot P(\text{mbar})/T(\text{K})$ is the density of scattering centers in the residual gas, n_Z is the number of atoms per gas molecule, P is the residual gas pressure, T is the temperature, r_e is the classical radius of the electron, Z is the charge of the scattering nucleus, γ is the relativistic gamma factor for the electron beam, $\langle \beta \rangle$ is the average beta function, A is the limiting transverse aperture, and β_A is the beta function at the position of the limiting aperture [4] (in the horizontal plane, the injection septum is the limiting aperture while the dipole magnet vacuum chamber is the limiting aperture in the vertical plane). For the measured residual gas pressure of $\sim 5 \cdot 10^{-8}$ mbar of two-atomic nitrogen ($n_Z=2$ and $Z=7$), the horizontal and vertical elastic scattering lifetimes become ~ 66 s and ~ 20 s, respectively, which both are significantly longer than the measured lifetime. The disagreement can partly be explained by the closed orbit deviation observed in figure 5.4 and 5.5 which reduces the

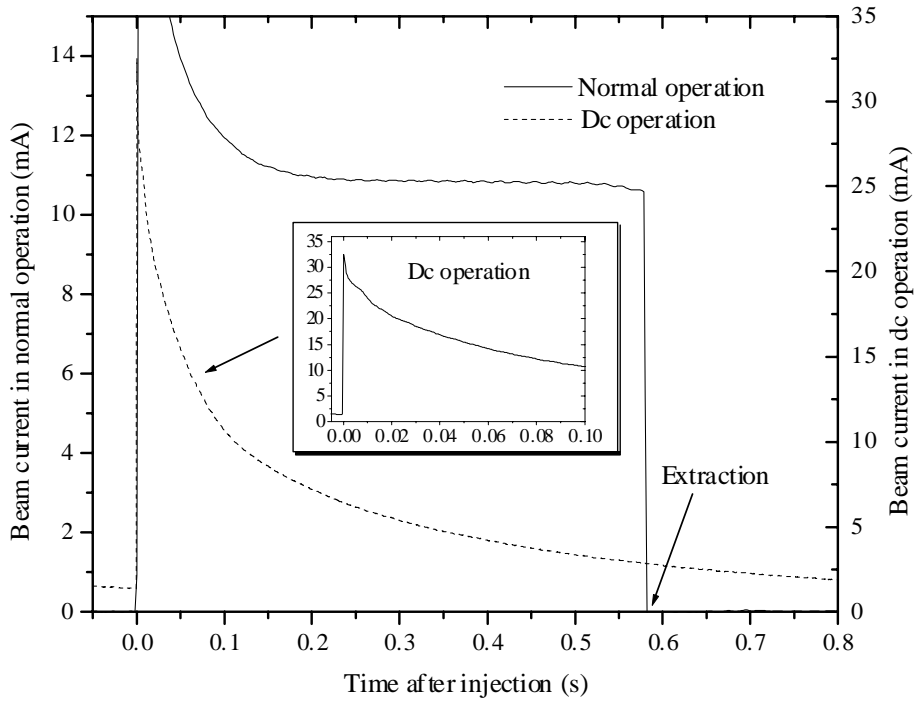


Figure 5.8: Circulating beam current in the booster synchrotron for both normal operation (ramping of the beam energy) and dc operation (53 MeV) as a function of time after the injection.

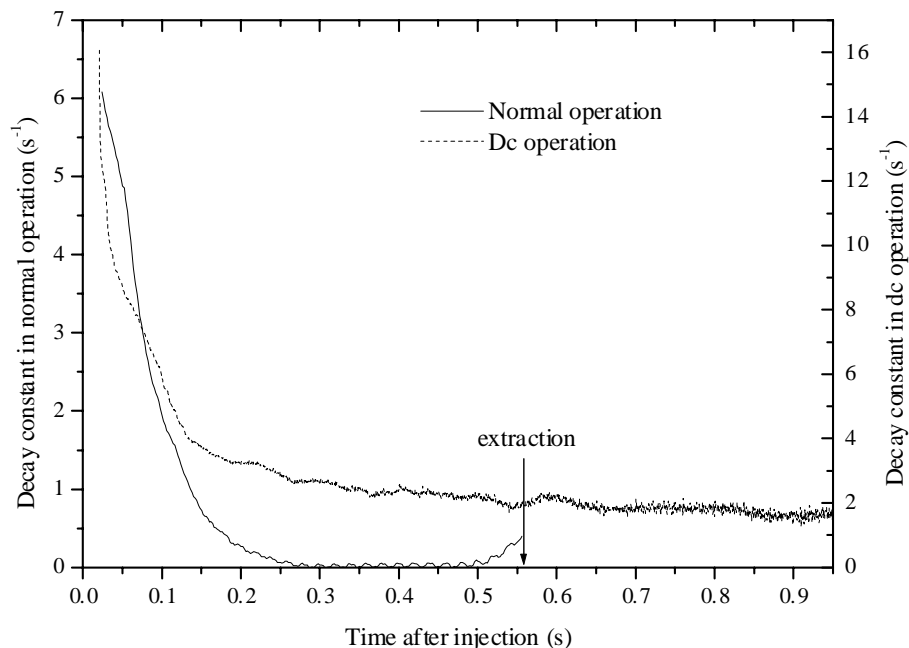


Figure 5.9: Decay constant of the circulating beam for both normal operation (ramping of the beam energy) and dc operation (53 MeV) as a function of time after the injection.

effective transverse aperture. However, the observed closed orbit deviation cannot account for a decrease of the lifetime by more than a factor of ~ 2 . The residual gas pressure is therefore believed to be somewhat higher than anticipated. The reason for the underestimation of the pressure is ascribed to the position of the vacuum gauges directly above the ion pumps. In addition, the lifetime would decrease by a factor 1.5 if CO_2 dominates the residual gas. Trapping of ions in the negative potential of the beam is not believed to affect the lifetime because the maximum density of trapped ions (the density cannot exceed the electron density) is at least two orders of magnitude lower than the residual gas pressure for a circulating beam current of 10 mA.

As suggested by (5.6), the lifetime in normal operation of the booster synchrotron, increases dramatically during ramping due to the increase of the beam energy and the decrease of the transverse beam size which enhances the effective aperture. According to figure 5.9, the lifetime reaches a maximum of ~ 50 s 300 ms after injection (257 MeV). For a beam energy above 450 MeV (490 ms after injection), the lifetime starts to decrease owing to a decline of the quantum lifetime, resulting from an insufficient cavity voltage. Unfortunately, the cavity voltage cannot be increased further owing to inadequate low-level drive power. This is a consequence of the need for additional low-level rf power after the installation of the fast rf feedback loop (see paragraph 3.2.2).

5.3.2 Bunch length

The time structure of the circulating beam in the booster synchrotron provides information about the longitudinal properties of the beam. Assuming a uniform filling pattern in the booster synchrotron and bunches with a Gaussian longitudinal density distribution, the beam current has the following form in frequency domain [5]:

$$I_b(\omega) = Q\omega_{rf}\delta(\omega) + 2Q\omega_{rf}\exp\left(-\frac{1}{2}(\omega\sigma_s)^2\right)\sum_{n=1}^{\infty}\delta(\omega - n\omega_{rf}) , \quad (5.7)$$

where the synchrotron sidebands have been omitted, ω is the angular frequency, Q the total charge of a single bunch, ω_{rf} is the angular rf frequency, and σ_s is the bunch length (one standard deviation). Hence, the bunch length can be determined if the relative amplitude of all rf harmonics up to a frequency well above $1/(2\pi\sigma_s)$ are measured. Utilizing a spectrum analyzer, the amplitude of a given rf harmonic can be inferred from the button pickup or the stripline signals. In particular, the observed signal by the spectrum analyzer is $T(\omega)Z_p(\omega)I_b(\omega)+B(\omega)$, where $T(\omega)$ is the overall transmission coefficient of the vacuum feedthrough (only the striplines) and the cable connecting the pickup and the spectrum analyzer, Z_p is the transfer impedance of the pickup, and B is the background noise of signal. The transmission coefficient of the cable is characterized up to a frequency of 5 GHz by measuring the transmitted power from an oscillator versus frequency, and the properties of the stripline feedthrough is specified by the manufacturer. In addition, the frequency dependence of the transfer impedance of a single button pickup and stripline is given by

$$Z_p \propto \frac{\omega}{1 + j\omega Z_L C} \quad (\text{single button pickup}) \quad (5.8)$$

$$Z_p \propto \exp(i(\pi/2 - l\omega/c))\sin(l\omega/c) \quad (\text{single stripline pickup}) , \quad (5.9)$$

where Z_L is the impedance of the output line, C is the capacitance of the button pickup, and l is the length of the stripline [6]. Finally, the background noise for the high frequency rf harmonics is determined at injection at which point the bunch length is large.

Having determined Z_p , T , and B , the relative amplitude of all rf harmonics up to 5 GHz are readily established by a spectrum analysis of the signal of a single button pickup or the sum signal of all four striplines at the stripline unit DSL_B.02. The resulting bunch length during ramping of the beam energy is shown in figure 5.10. It is observed that the bunch length the first 200 ms after injection, corresponding to a beam energy below 150 MeV, approximately follows the bunch length dictated by adiabatic damping according to which $\sigma_s \propto V_{rf}^{-1/4} \cos\phi_s^{-1/4} p^{-1/4}$, where V_{rf} is the amplitude of the rf voltage, ϕ_s is synchronous phase, and p is the electron momentum. Subsequently, the synchrotron light damping is strong enough to reduce the bunch length below what is expected of adiabatic damping. In fact,

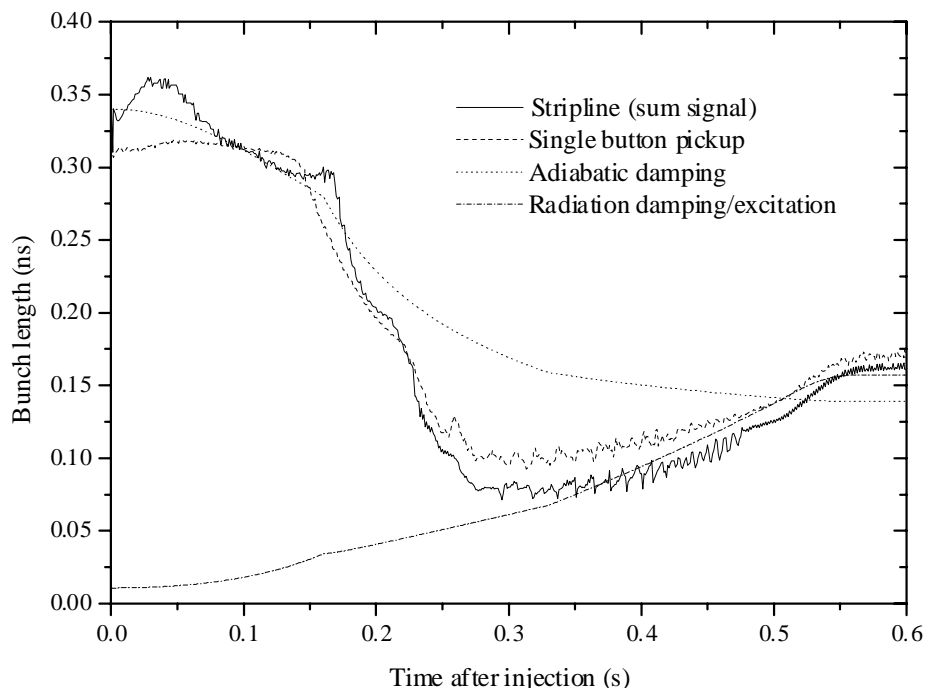


Figure 5.10: Bunch length (one standard deviation) of the individual electron bunches in the booster synchrotron throughout the ramping of the beam energy. The bunch length given by adiabatic damping and synchrotron radiation damping/excitation are also indicated.

beyond 350 ms after injection (above 300 MeV), the bunch length is in good agreement with the equilibrium between synchrotron light damping and excitation. This behavior fits well with the theoretical longitudinal damping time of 0.12 s for a beam energy of 300 MeV. The measured bunch length at full beam energy is 0.170 ± 0.017 ns.

The button pickup measurement is believed to be more accurate than the stripline measurement because the transfer impedance (5.9) of a stripline is zero for all equal multiples of the rf frequency ($l=150$ mm), reducing the available rf harmonics by a factor of two (in practice, however, the amplitude the rf harmonics at equal multiples of the rf frequency are only reduced about a factor of two due to a non-perfect matching of the impedance of the striplines to the output line). The small discrepancy between of the button pickup measurement and the theoretical bunch length given by synchrotron light damping and excitation is likely to be due to a non-ideal transfer impedance of the button pickup. In addition, the button pickup is more sensitive to the electrons with large transverse amplitudes because it covers a rather small space angle, resulting in a higher sensitivity towards off-momentum particles due to a finite horizontal dispersion. This effect could explain why the button pickup measurement at high energy is slightly larger than the theoretical bunch length.

5.3.3 Momentum spread

Assuming the electrons only occupy the linear region of the longitudinal phase space, the relative momentum spread is related to the bunch length by the relation

$$\frac{\sigma_p}{p} = \omega_{rev} \sqrt{\frac{heV_{rf} \cos \phi_s}{2\pi|\gamma^2 - \alpha_p|\beta cp}} \sigma_s, \quad (5.10)$$

where ω_{rev} is the angular revolution frequency, h is the number of electron bunches, γ and β are the relativistic gamma and beta factors, and p is the electron momentum [7]. The measurement of the bunch length in figure 5.10 can therefore be transformed into a relative momentum spread, which is plotted in figure 5.11 throughout the ramping of the beam energy. The behavior of the relative momentum spread versus time after injection is the same as that discussed in paragraph 5.3.2. The measured relative momentum spread at full energy is $(3.6 \pm 0.4) \cdot 10^{-4}$.

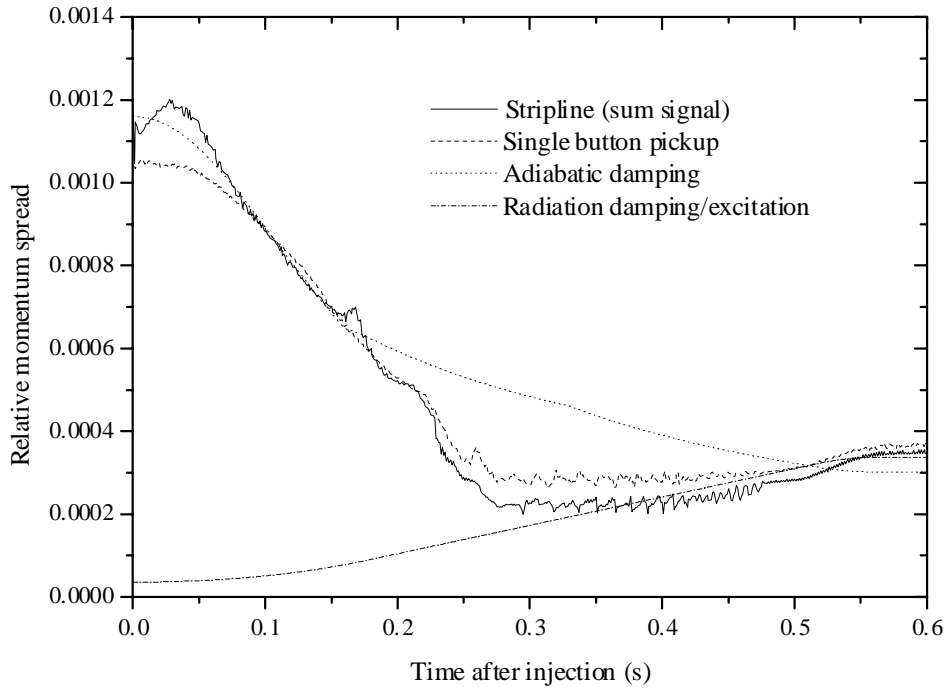


Figure 5.11: Relative momentum spread (one standard deviation) of the circulating beam in the booster synchrotron during ramping of the beam energy. The relative momentum spread given by adiabatic damping and synchrotron radiation damping/excitation are also indicated.

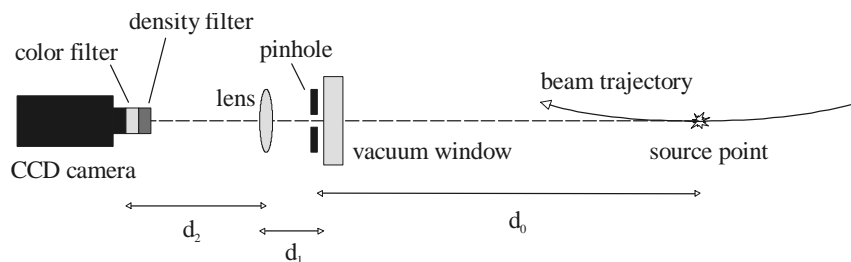


Figure 5.12: Schematic of the synchrotron light imaging system of the booster synchrotron ($d_0=689$ mm and $d_1=51$ mm).

5.3.4 Transverse emittances

In analogy with the determination of the transverse emittances of the racetrack microtron beam utilizing synchrotron light in paragraph 4.4.3, the synchrotron light emitted in the bending magnets of the booster synchrotron provides information about the transverse beam profile from which the transverse emittances can be established. The imaging system which records the synchrotron light of the booster synchrotron is illustrated in figure 5.12. It consists of a pinhole with a radius of 2 mm which reduces the transverse size of the synchrotron light cone, a CCD camera without lens equipped with a density filter and an ultraviolet color filter, and a lens with a focal length of 240 mm which focuses the synchrotron light on the CCD chip. Owing to the color filter, the imaging system only records synchrotron light in a narrow wavelength band around 384 nm. In order to determine the camera position which produces the smallest synchrotron light spot on the CCD chip, images of the synchrotron light are recorded for various positions of the CCD camera. For each image, the two-dimensional intensity distribution is projected into the horizontal and vertical planes, enabling a determination of the center and the transverse sizes of the synchrotron light spot at the CCD chip. The found transverse spot sizes for a beam energy of 500 MeV as a function of the camera position are plotted in figure 5.13, revealing a minimum of the transverse spot size in both planes which are separated by ~ 30 mm. The separation is ascribed to a larger region from where synchrotron light is recorded in the horizontal plane (the beam trajectory bends horizontally), causing a deviation from ideal imaging in the horizontal plane.

In order to simplify the analysis of the one-dimensional profiles of the synchrotron light spot, it is assumed that the synchrotron light cone, originating from a single electron, after the pinhole can be described by a Gaussian beam with a minimum waist of w_0 at a distance d_w behind the pinhole. In this way, the complex nature of the synchrotron light emission and the subsequent diffraction effects at the pinhole is parameterized by a Gaussian beam. Adopting this approximation, the one standard deviation transverse size of the

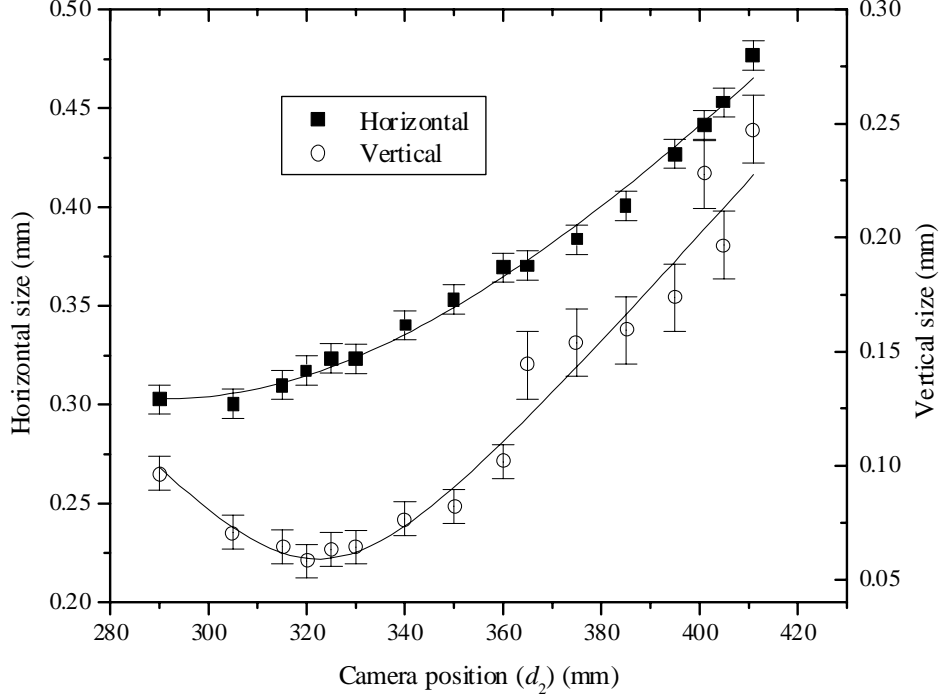


Figure 5.13: Transverse sizes (one standard deviation) of the synchrotron light spot at the CCD chip as a function of the camera position for a beam energy of 500 MeV. The line graphs are fits of (5.12) to the data.

synchrotron light spot at the CCD chip, originating from a single electron, is (see appendix E)

$$\frac{1}{2}w_{CCD} = \frac{1}{2}\sqrt{\frac{(f(d_w + d_1 + d_2) - d_2(d_w + d_1))^2 \lambda^2}{\pi^2 f^2 w_0^2} + \frac{(f - d_2)^2 w_0^2}{f^2}}, \quad (5.11)$$

where f is the focal length of the lens and λ is the wavelength of the synchrotron light (is well-defined due to the color filter). Summing over all electrons in the beam, the standard deviation transverse size of the synchrotron light spot at the CCD chip becomes

$$\sigma_{CCD} = \sqrt{\frac{1}{4}w_{CCD}^2 + \left(\sigma_{beam} \frac{d_f}{d_0 + d_1}\right)^2 + \sigma_{res,1}^2 + \sigma_{res,2}^2}, \quad (5.12)$$

where σ_{beam} is the transverse size of the electron beam, d_f is the distance from the lens to the position of the focus (the position of the minimum vertical synchrotron light spot), and $\sigma_{res,1}$ and $\sigma_{res,2}$ represent finite resolutions of the image arising from the extended source region

(see appendix E). The model (5.12) is fitted to the data in figure 5.13, providing the fit results $\sigma_{beam,x}=0.69\pm 0.04$ mm and $\sigma_{beam,y}=0.13\pm 0.02$ mm for the horizontal and vertical planes, respectively. In comparison, the minimum waist of the synchrotron light cone, originating from a single electron, at the CCD chip is 0.021 mm and 0.024 mm for the horizontal and vertical planes, respectively, demonstrating that the diffraction of the synchrotron light only has a modest influence on the vertical spot size. The same is true for the effect of the extended source region since $\sigma_{res,1}=0.0133$ mm and $\sigma_{res,2}=0.0094$ mm, indicating a resolution of the imaging system of ~ 0.01 mm in the image plane which is equivalent of a resolution of ~ 0.02 mm in the object plane. The high resolution is a result of the small detection wavelength of the imaging system, which reduces diffraction effects, and the fact that the diffraction of the synchrotron light and the extended source region have been taken into account in the analysis.

The position of the electron beam for two different rf frequencies are also measured. Employing the definition of the dispersion and the expression (5.3), one obtains a horizontal dispersion of 0.88 ± 0.09 m in reasonable agreement with a lattice calculation which yields a horizontal dispersion of 1.03 m. Combining this result with expression (4.13), relating the transverse size the electron beam and the transverse emittance, the horizontal and vertical emittances of the electron beam at 500 MeV are finally found to be 165 ± 22 nm and 2.3 ± 0.8 nm, respectively. In the computation of the emittances, the beta functions and the momentum spread are provided by a lattice calculation because the actual beta functions and momentum spread have been found to agree well with the theoretical values. The determined horizontal emittance is in good agreement with the theoretical value of 152 nm given by the equilibrium between synchrotron radiation damping and excitation. Furthermore, the rather low vertical emittance demonstrates a low coupling between the two transverse planes.

In order to determine the variation of the transverse emittances throughout the acceleration of the beam, the transverse density distribution of the beam is recorded for various delays after injection with the help of the synchrotron light imaging system. The density distributions are shown in figure 5.14, revealing a dramatic decrease of the beam size during ramping due to the synchrotron radiation damping of the betatron oscillations. Having already determined the contributions of the diffraction of the synchrotron light and the extended source region to the recorded intensity distributions, the transverse emittances are readily determined for all the images in figure 5.14. The resulting transverse emittances are shown in figure 5.15, displaying an efficient radiation damping of the emittance of both transverse planes, providing a good agreement of the horizontal emittance with the equilibrium between radiation damping and excitation beyond 0.4 s. In addition, the initial value of the vertical emittance of 175 ± 25 nm is in excellent agreement with the found vertical emittance of 0.21 ± 0.05 mm mrad of the racetrack microtron beam in paragraph 4.4.3.

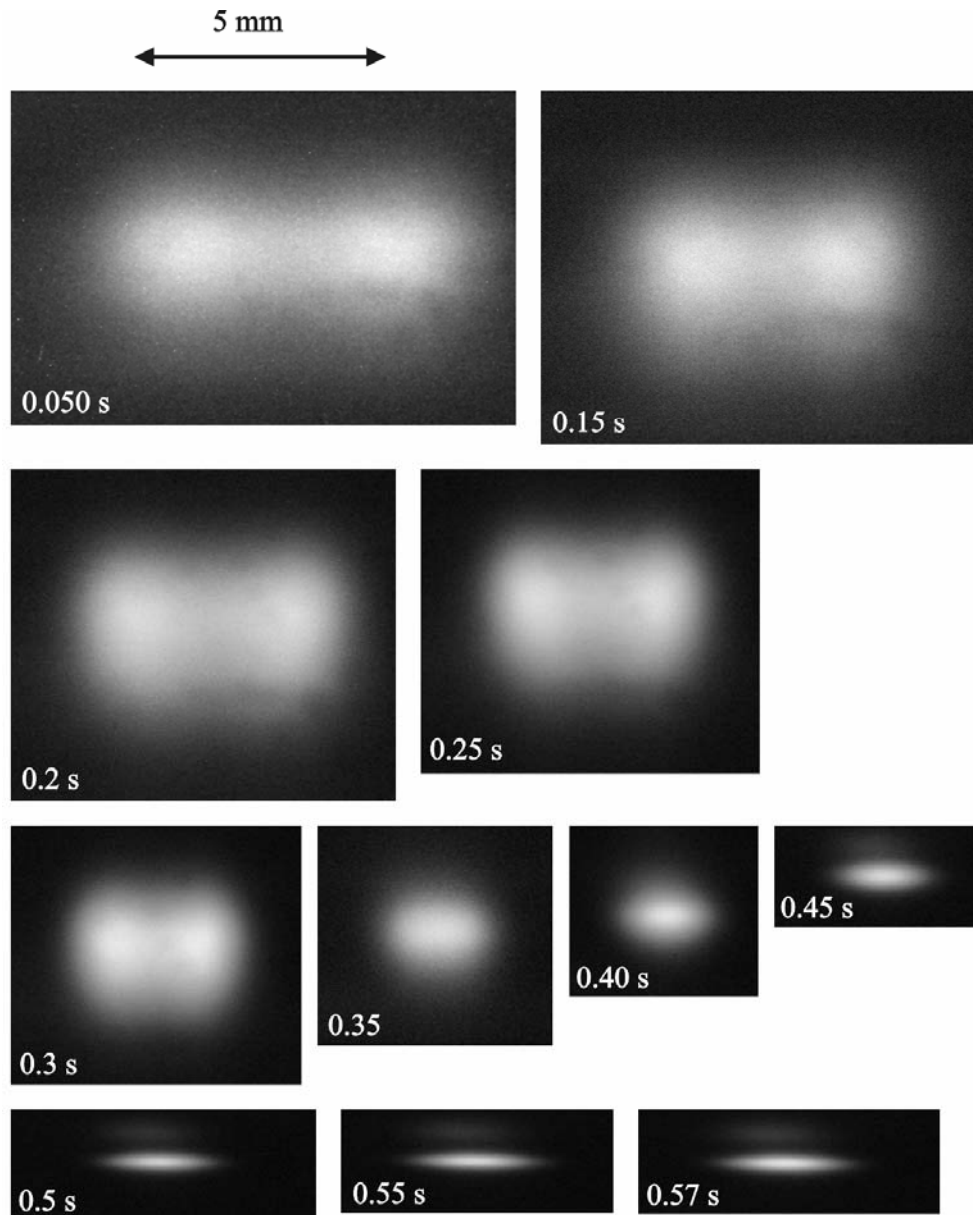


Figure 5.14: Transverse density distribution of the electron beam in the center of the dipole magnet versus time after the injection.

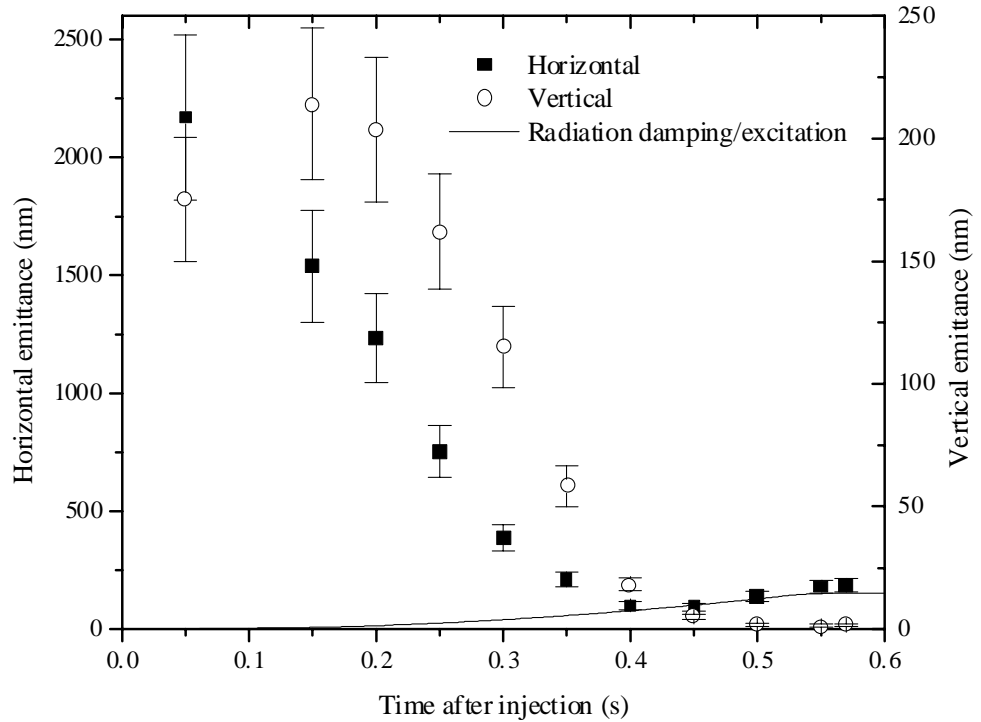


Figure 5.15: Transverse emittances of the circulating beam in the booster synchrotron as a function of time after injection. The expected horizontal emittance due to the equilibrium between synchrotron radiation damping and excitation is also plotted.

5.4 The injection process

5.4.1 Investigation of the multi-turn injection scheme

The beam current in the booster synchrotron shortly after the injection process is shown in figure 5.8 (dc operation zoom-in), demonstrating that a beam current of more than 30 mA can be injected into the booster synchrotron. Assuming an injection efficiency of ~80 percent, this corresponds to a multi-turn injection process which proceeds over 3-4 revolutions of the booster synchrotron for an output beam current of 12 mA of the racetrack microtron. The horizontal tune dependence of the injection process has also been studied by recording the circulating beam current 100 ms after the injection in dc operation as a function of the horizontal tune Q_x . The results presented in figure 5.1 resemble the behavior of the optimum Q_2 parameter in figure 3.3 if the influence of the betatron resonances is ignored. In particular, the injected beam current for $Q_x=1.85$ is slightly larger than for $Q_x=1.75$, and the injected beam current decreases abruptly above $Q_x=1.90$.

In order to determine the horizontal profile of the beam shortly after the injection pro-

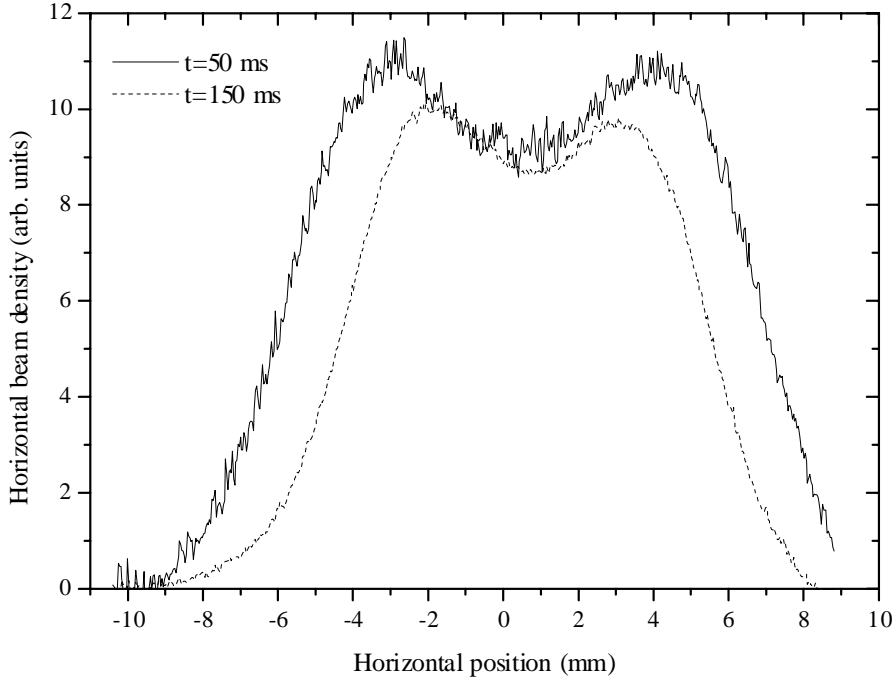


Figure 5.16: Measured horizontal profile of the beam at the injection septum 50 ms and 150 ms after injection inferred from the density distributions in figure 5.14. The profiles have been transformed from the center of the dipole magnet to the position of the injection septum by scaling the horizontal axis by a factor of 1.80. In addition, the beam densities of the two profiles have been scaled independently.

cess, the two first images in figure 5.14 are projected into the horizontal plane and the one-dimensional profiles are transformed to the position of the injection septum for a comparison with figure 3.5. The found horizontal profiles of the beam 50 ms and 150 ms after the injection are shown in figure 5.16, revealing a small dip in the center of the beam profiles similar to those in the simulations in figure 3.5. However, the width of the observed horizontal profile 50 ms after the injection is considerable smaller than those in figure 3.5. The discrepancy is partly accredited to a rather short elastic scattering lifetime of the electrons performing large betatron oscillations (small effective aperture in (5.6)), causing the horizontal width of the beam to decrease the first 50 ms after injection. In addition, the optimization of the beam current at 500 MeV is likely to favor injection parameters which produce a smaller beam size after injection than those in figure 3.5 because many of the electrons far from the center orbit will be lost due to elastic scattering at low energy before synchrotron light damping becomes effective. In fact, the quality parameters of the injection process in paragraph 3.3.2 would provide more realistic injection parameters if the added contingency of the septa was increased to ~ 10 mm. The preference for a small

horizontal beam size which requires a shorter excitation pulse of the injection kicker magnet explains why the injection process proceeds over fewer turns than anticipated in paragraph 3.3.2.

5.4.2 Capture of the beam by the rf system

In paragraph 3.3.4 it was concluded that a fast rf feedback loop with a high gain is essential for an efficient capture of the injected beam by the rf system. According to (3.3), the low-level drive signal V_{in} increases by a factor $1+K\alpha$ after installation of the fast rf feedback loop in order to produce the same voltage in the cavity (at resonance of the cavity). Hence, the phase shifter and amplifier of the loop can be optimized for the highest possible loop gain by maximizing V_{in} without beam in the booster synchrotron since the amplitude loop maintains a constant cavity voltage by changing V_{in} . Performing this measurement, the ratio between the maximum value of V_{in} and the corresponding value without fast rf feedback loop yields a maximum value of $K\alpha$ of 15.8 for the rf system of the booster synchrotron. This is somewhat less than the theoretical maximum of $Q_L/(4f_{cav}T)=41.4$ derived in paragraph 3.3.4 (the total delay T of the loop is measured to be 234 ns). The discrepancy is attributed to pick-up of noise of the loop from the surrounding environment which probably can

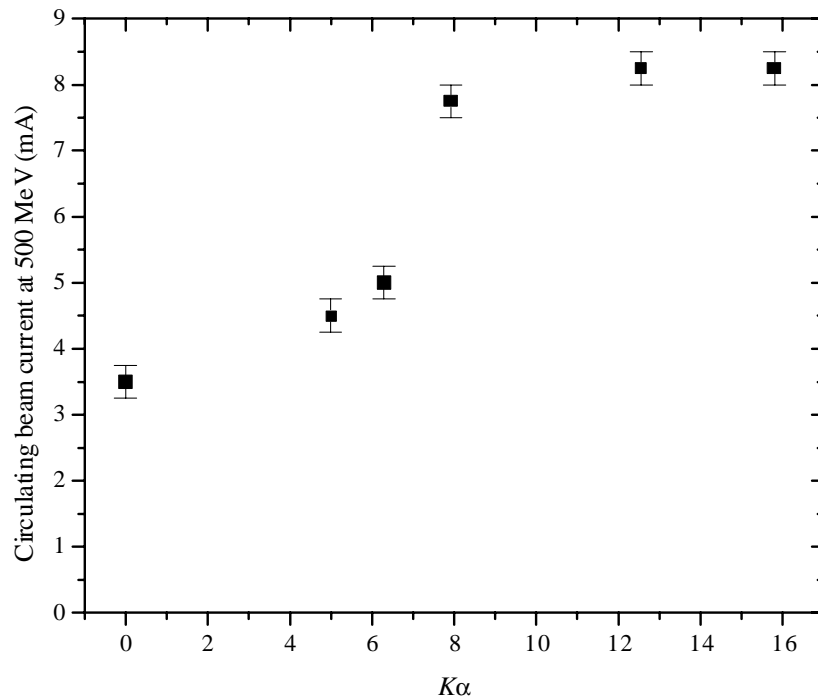


Figure 5.17: Circulating beam current at 500 MeV as a function of $K\alpha$ (the attenuation of the variable attenuator in the fast rf feedback loop is changed).

be reduced by locating the amplifier of the loop closer to the cavity.

In order to test the effect of the fast rf feedback loop, the circulating beam current in the booster synchrotron at 500 MeV is measured as a function of $K\alpha$. The result in figure 5.17 reveals an improvement of the beam current by a factor ~ 2.5 with the loop, clearly demonstrating the harmful effect of beam loading on the capture efficiency. In addition, the figure indicates that the negative effect of the beam loading disappears for $K\alpha > 8$ in excellent agreement with the analysis in paragraph 3.3.4. The capture efficiency with fast rf feedback loop versus the cavity voltage is also studied by recording the circulating beam current 100 ms after the injection as a function of the amplitude of the cavity voltage. The result of the measurement is shown in figure 5.18 (the beam current is not shown for amplitudes of the cavity voltage above 12 kV as the amplitude loop for higher voltages gets unstable at injection due to the limited low-level power). According to the figure, the captured beam current has a maximum for a cavity voltage of 8 kV which is slightly higher than the expected value of 5 kV in paragraph 3.3.3. The difference is attributed to the fact that the measured horizontal beam size in figure 5.16 is smaller than that estimated by the simulations in paragraph 3.3.2, increasing the acceptable enlargement of the horizontal beam size by the induced momentum spread of the cavity voltage.

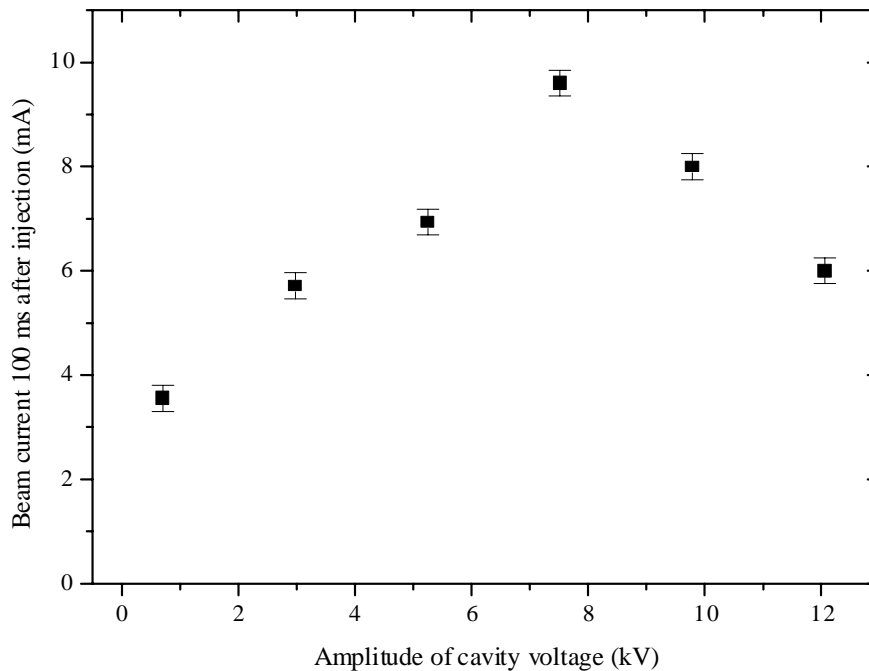


Figure 5.18: Circulating beam current 100 ms after the injection (dc operation) as a function of the amplitude of the cavity voltage.

5.4.3 Analysis of large initial beam loss after injection

According to figure 5.8, a significant beam loss occurs the first ~ 100 ms after injection. The beam loss can partly be ascribed to a large transverse beam size following the injection, resulting in a low elastic scattering lifetime according to (5.6) due to the low effective transverse aperture for the particles with large betatron amplitudes. However, elastic scattering can only account for the entire beam loss provided the effective horizontal and vertical apertures immediately after injection is about a factor of ten and six smaller, respectively, than those associated with the asymptotic lifetime discussed in paragraph 5.3.1. However, the observed transverse beam profiles in figure 5.14 and 5.16 together with the measured closed orbit deviations in figure 5.4 and 5.5 show that the effective transverse apertures following the injection are at least half of those associated with the asymptotic lifetime, suggesting that elastic scattering only is responsible for a small part of the initial beam loss. In addition, measurements reveal that the asymptotic lifetime decreases much faster for increasing residual gas pressure than the initial lifetime, also indicating that elastic scattering only accounts for a small fraction of the initial beam loss.

Those electrons which are not captured by the rf system of the booster synchrotron do also contribute to beam loss the first ~ 100 ms after injection. For the optimum cavity voltage of 8 kV in figure 5.18, ideally 80 percent of the injected electrons are captured in the longitudinal rf bucket according to figure 3.6, corresponding to a 20 percent beam loss. On the other hand, the enhanced horizontal beam size resulting from the increased momentum spread produced by the rf cavity is not expected to contribute to the beam loss owing to the small horizontal beam size observed in figure 5.16. Nevertheless, the large initial beam loss in figure 5.8 indicates that less than 50 percent of the electrons are captured by the rf system. The reason is likely to be the abrupt change of beam loading at injection which strongly perturbs the longitudinal phase space (see paragraph 3.3.4). In addition, the transient beam loading may cause the amplitude loop to overcorrect the cavity voltage with the result that the longitudinal phase space is distorted even further. In fact, the oscillating behavior of the stripline sum signal the first millisecond after injection in figure 5.19 suggests a strong perturbation of the longitudinal dynamics by the transient beam loading. This does not lead to instant beam loss because electrons which are not captured by the rf system may circulate several tens of milliseconds as a result of the rather weak synchrotron radiation emission.

As demonstrated in paragraph 3.3.4, the harmful effect of the transient beam loading can be suppressed by detuning the cavity $108/(1+\alpha K)$ kHz below the rf frequency, corresponding to an optimum detuning of 6.43 kHz for the measured gain of the fast rf feedback loop above. Unfortunately, the detuning was fixed at -10 kHz after the installation of the fast rf feedback loop, causing a transient behavior of the beam-cavity interaction as suggested by figure 5.19. Even after an optimization of the detuning, the longitudinal phase space and amplitude loop will be somewhat perturbed by the transient beam loading be-

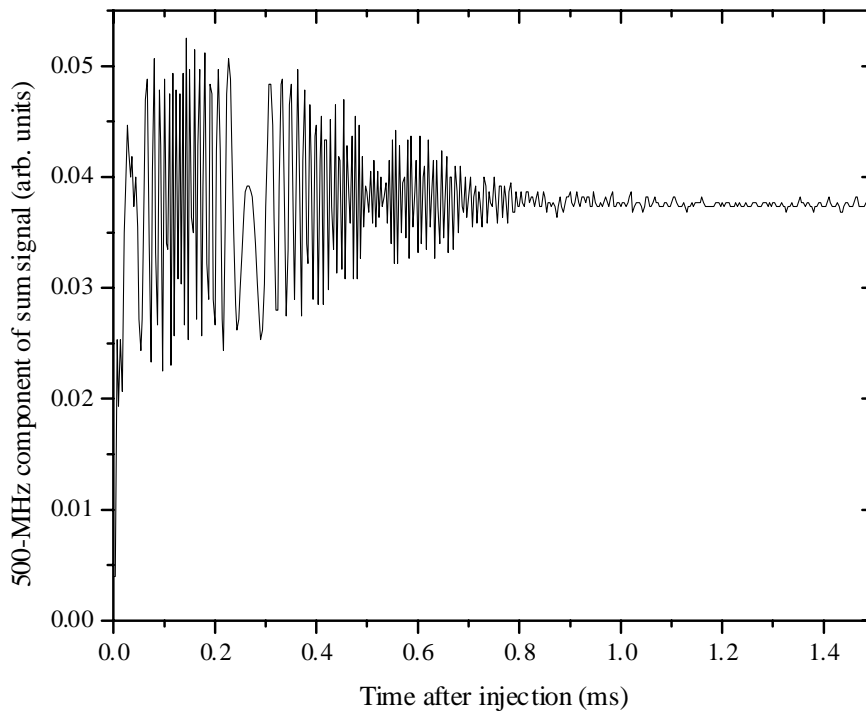


Figure 5.19: 500-MHz component of the sum signal of all striplines at DSL_B.02 the first 1.5 ms after injection.

cause the beam current and thus the optimum detuning changes considerable during the injection process.

On the other hand, collective beam instabilities are not believed to contribute to the initial beam loss since a non-uniform filling pattern of the electron bunches and abrupt beam losses resulting in large variations of the circulating beam current from injection to injection are not observed. Furthermore, a thorough search for peaks in the beam spectrum linked to coherent beam oscillations has not revealed any collective beam instabilities.

5.5 The extraction process

5.5.1 Investigation of the leak field of the extraction septum magnet

As described in paragraph 3.5.1, the beam is bumped towards the extraction septum before the extraction process in order to reduce the required strength of the extraction kicker magnet. In order to study this horizontal displacement of the beam shortly before the extraction, the horizontal difference signal of all four striplines close to the injection septum is recorded with a spectrum analyzer in zero span mode at the rf frequency. Assuming a linear

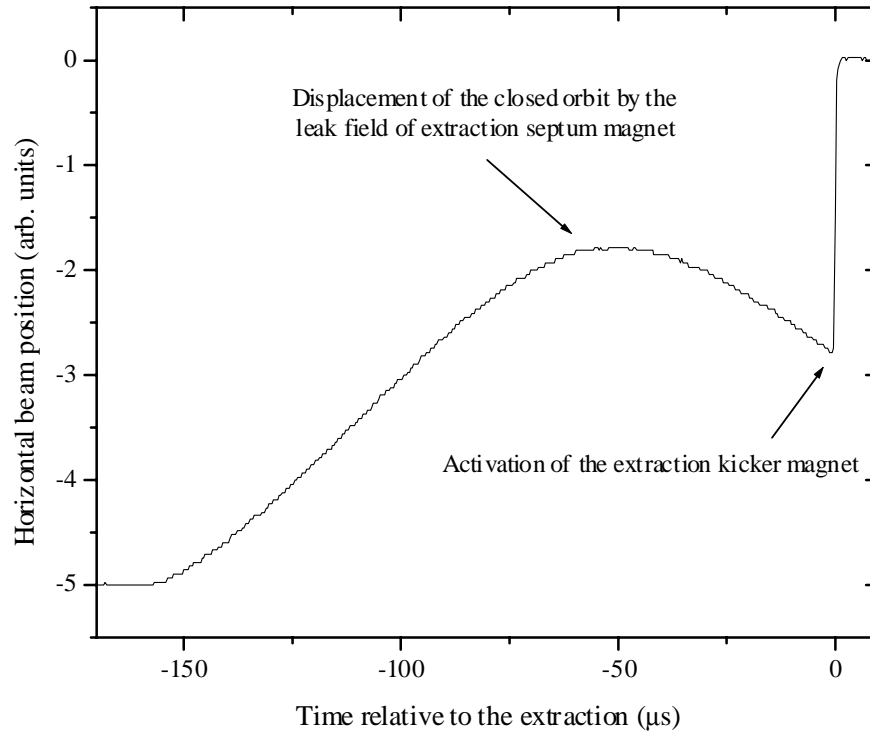


Figure 5.20: Horizontal beam position shortly before the extraction inferred from all four striplines at DSL_B.02. The corrector magnet at the extraction septum is ramped (see text).

response of the stripline signal to a transverse displacement of the beam, the resulting horizontal beam position is shown in figure 5.20, revealing a significant displacement of the beam by the leak field of the extraction septum magnet (the septum magnet is excited by a half sine-shaped current pulse with a half width of $135 \mu\text{s}$). The observed closed orbit displacement by the leak field can be modeled by a kick at the extraction septum as shown in figure 5.21. According to the figure, the leak field displaces the beam closer to the extraction septum where the leak field is larger, resulting in an even larger effect of the leak field. If the beam is sufficiently close to the extraction septum, this self-amplifying displacement of the closed orbit will produce a rapidly increasing displacement of the closed orbit. Initially, this effect caused the beam to be lost on the extraction septum sheet or the extraction kicker magnet when the beam was bumped towards the extraction (see figure 5.21), preventing an extraction of the beam because the leak field peaks $50 \mu\text{s}$ before the field of the septum magnet is appropriate for extraction (see figure 5.20). The shift of the leak field maximum with respect to the field of the septum magnet is ascribed to a large inductive contribution to the leak field.

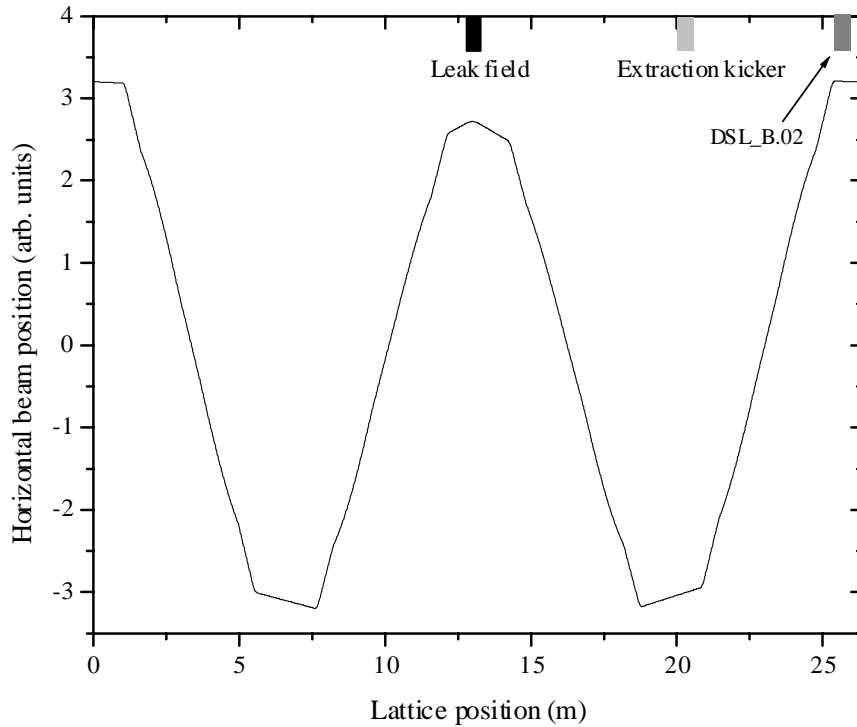


Figure 5.21: Calculated horizontal closed orbit displacement by the leak field (the field direction of the leak field is opposite of that of the extraction septum magnet).

The harmful effect of the leak field was reduced by improving the shielding of the extraction septum magnet and by ramping the horizontal corrector magnet close to the extraction septum synchronously with the bumper windings, but with a field of opposite polarity to that of the leak field. The compensation of the leak field is almost perfect at extraction if the integrated strength of the corrector magnet is the same as that of the leak field. However, the leak field peaks $50 \mu\text{s}$ before the extraction, preventing the beam from being bumped as closed to the septum sheet prior to the extraction as desired. Even with a higher excitation of the corrector magnet this is not possible as the compensation will be too large at extraction, resulting in a displacement of the beam away from the septum sheet. In addition, there exists an excitation maximum above which the corrector magnet causes beam loss before the leak field appears owing to the closed orbit deviation produced by the corrector magnet itself. Nevertheless, the corrector magnet reduces the effect of the leak field considerable, facilitating an extraction of the electron beam.

Comparing the closed orbit deviation in figure 5.21 with the horizontal apertures at the extraction septum and kicker magnet, the integrated field of the leak field with shielding is estimated to $\sim 50 \text{ Gm}$ at the center orbit.

5.5.2 Beam behavior after the activation of the extraction kicker magnet

The horizontal beam position after the extraction kicker magnet is triggered is investigated by recording the horizontal difference signal of all four striplines at the stripline unit DSL_B.02 by means of an oscilloscope with a time division of 25 ns. The recorded signal is sampled with the rf period, providing the signal amplitude for each passage of an electron bunch. Assuming a linear response of the difference signal to the transverse position of the beam, the horizontal position of each bunch passing the striplines is obtained. In figure 5.22 the measured horizontal beam position is plotted as a function of the number of revolution periods after the first beam displacement by the kicker magnet is observed. According to the figure, the beam acquires the full deflection of the extraction kicker magnet 0.32 revolution after the first displacement of the beam is observed, corresponding to a 10%-90% rise time of the field of the extraction kicker magnet of 24 ns. Subsequently, the horizontal position of the beam stays constant until the part of beam which only received at partial de-

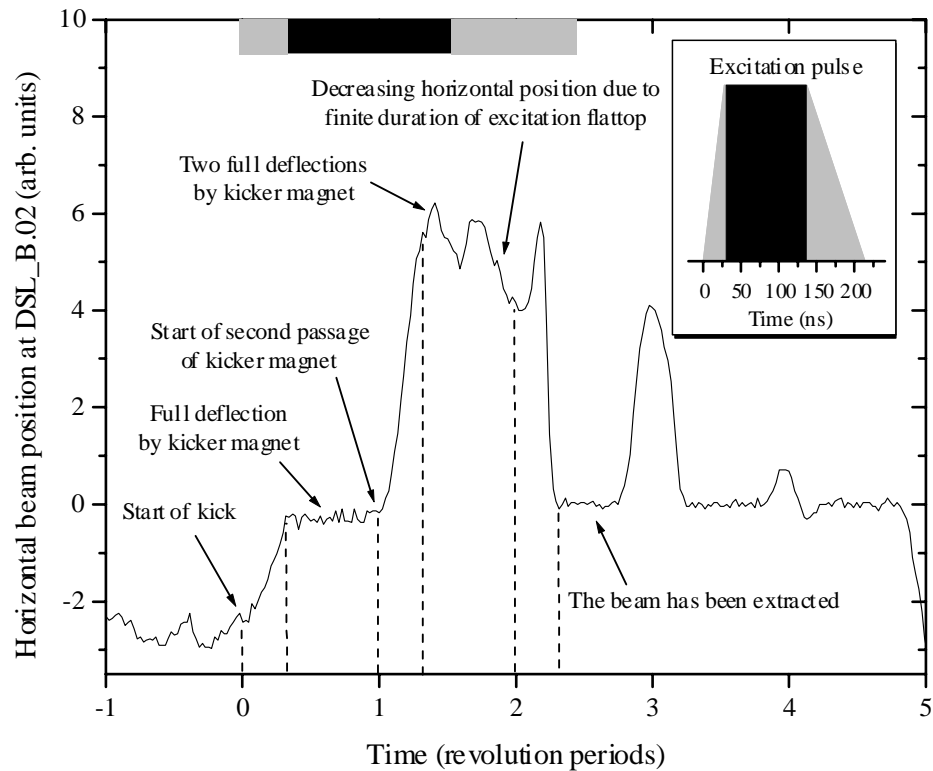


Figure 5.22: Horizontal position of each electron bunch passing the stripline unit DSL_B.02 as a function of the number of revolution periods after the first beam displacement by the extraction kicker magnet is observed. The shape of the excitation pulse of the kicker magnet is sketched in the upper right corner.

flected by kicker magnet experiences a second kick of full magnitude (1-1.32 in the figure 5.22). In contrast, the part of the beam which is subjected to a full deflection at the first passage of the kicker magnet is expected to enter the extraction septum channel and leave the booster synchrotron at the first passage of the extraction septum after the kick (see paragraph 3.5.1). Nevertheless, this part of the beam is observed at the stripline unit DSL_B.02 after two passages of the kicker magnet (1.32-2 in the figure 5.22), displaying a decreasing horizontal beam position as the length of the flattop of the excitation pulse of the kicker magnet only is ~ 110 ns. Instead, the part of the beam which experiences a full deflection at the first passage of the kicker magnet is observed to leave the booster synchrotron at its second passage of the extraction septum after the initial deflection by the kicker magnet (no beam in the interval 2.32-3 in figure 5.22), corresponding to an extraction $7/4$ revolutions after the initial kick (two-turn extraction process) in contrast to the expected $3/4$ of a revolution (one-turn extraction process). This was not recognized during the commissioning of the ANKA injector.

In order to understand the unexpected behavior of the beam during the extraction pro-

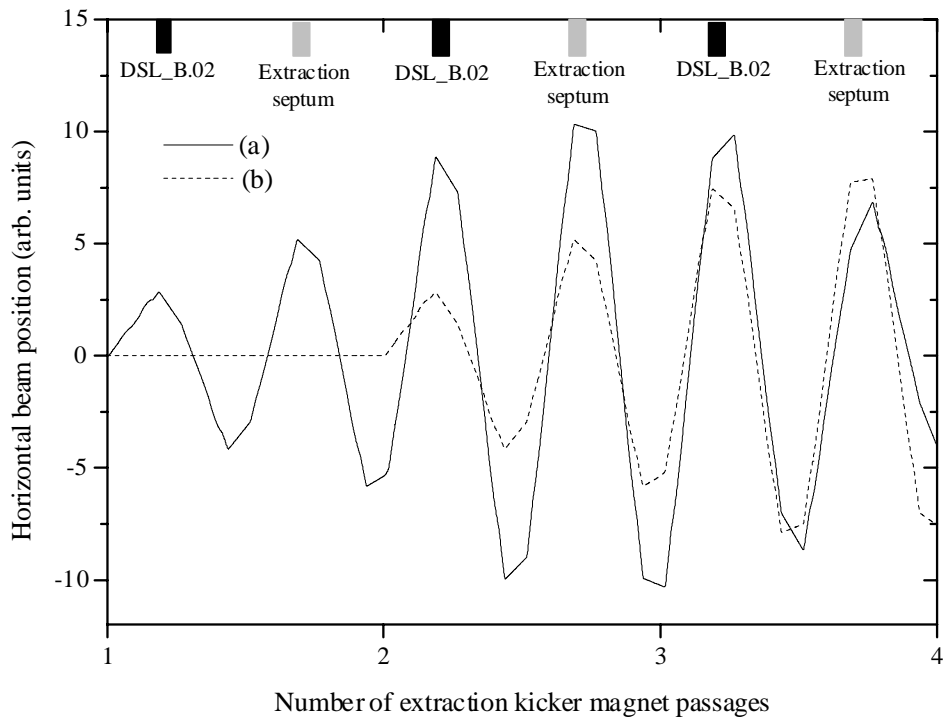


Figure 5.23: (a) Calculated horizontal position of the beam several revolutions after the kick for the part of the beam which passes the kicker magnet at the start of its excitation flattop. (b) As (a), but for part of the beam which passes the kicker magnet at the very beginning of the excitation pulse.

cess, the horizontal position of the beam is calculated for several revolutions after the kick for the part of the beam which passes the kicker magnet in the beginning of the excitation flattop (two full deflections of the beam by the kicker magnet). The result is shown in figure 5.23a, demonstrating that the horizontal displacement of the beam at the second passage of the extraction septum is a factor of two larger than that of the first passage. Hence, the two-turn extraction process is a result of a too small bump of the beam towards the extraction septum prior to the extraction, preventing a single-turn extraction due to a limited strength of the extraction kicker magnet. This finding is in good agreement with excitations of the bumper windings and the extraction kicker magnet of only 50 and 70 percent, respectively, suggesting that a one-turn extraction process is feasible, unless the bump cannot be moved closer to the extraction septum without losing the beam due to the leak field. In addition, the theoretical position of the beam in figure 5.23a is in excellent agreement with the observed horizontal position of the beam in figure 5.22. This confirms that the signal observed in the interval 1.28-2 in figure 5.22 is not produced by a tail of an already extracted beam (one-turn extraction process).

5.6 The properties of the extracted beam

5.6.1 Beam current and pulse length

The beam current of the extracted electron pulse is the single most important beam property of the ANKA injector since it to a large extent determines the filling time of the ANKA storage ring. An example of the beam current of the extracted electron pulse versus time is shown in figure 5.24, clearly displaying the 500-MHz bunch structure of the electron pulse. The average beam current of the pulse is 9.5 mA, which is better than the design value of 7.5 mA in table 3.1. In addition, a comparison with the circulating current of the booster synchrotron demonstrates that the extraction efficiency is ~90 percent. The two-turn extraction process thus does not appear to affect the extraction efficiency significantly.

According to figure 5.24, the FWHM length of the electron pulse is 52 ns which is slightly below the design value of 56 ns in table 3.1. The reason is that the part of the electron pulse which at the first beam passage is subjected to a full deflection of the kicker magnet at the second passage of the extraction kicker magnet experiences a decreasing deflection due to the finite length of the flattop of the excitation pulse (see figure 5.22), resulting in an insufficient deflection of the last part of the electron pulse to enable an extraction. In contrast, the one-turn extraction process is not influenced by the finite length of the flattop of the excitation pulse, facilitating an extracted electron pulse with a pulse length of at least 60 ns because the extraction kicker magnet reaches its maximum deflection within 28 ns and the revolution period of the booster synchrotron is 88 ns. The small beam current observed beyond 80 ns in figure 5.24 is attributed to those electrons which pass the kicker magnet in the very beginning of the excitation pulse. This is confirmed by figure 5.23b which shows that these electrons not until the third passage of the extraction

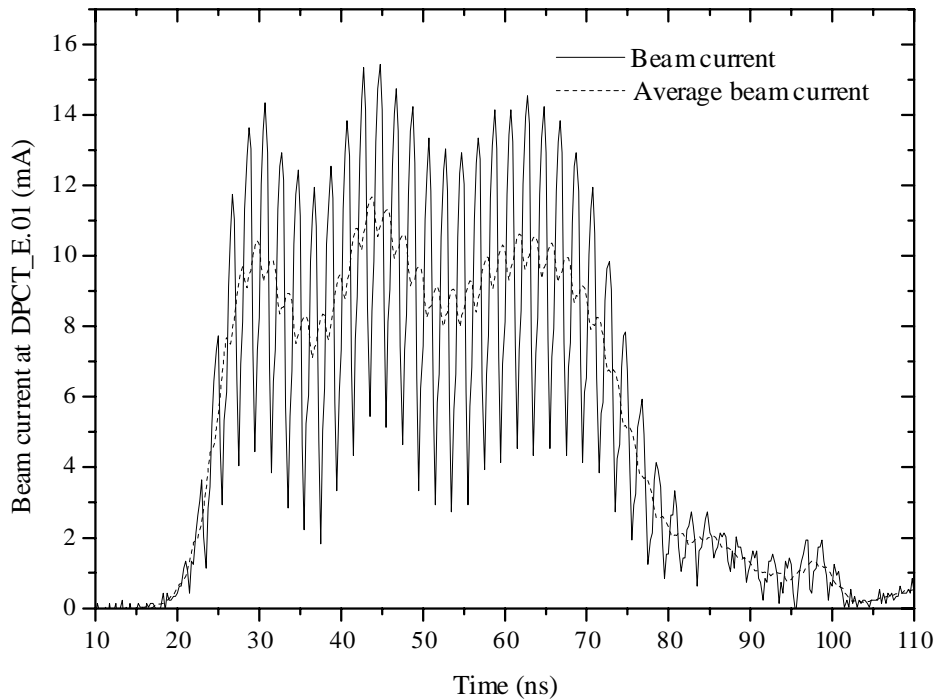


Figure 5.24: Beam current of the extracted electron pulse versus time measured with current transformer DPCT_E.01 (see figure A.1). The circulating beam current in the booster synchrotron is 10 mA at extraction.

septum experience a large enough horizontal deflection to be extracted (three-turn extraction process).

5.6.2 Transverse emittances and momentum spread

Besides the beam current of the extracted beam, its transverse emittances and momentum spread are also important for an efficient filling of the ANKA storage ring as these properties affect the transverse size of the beam in the storage ring. The transverse emittances and the momentum spread of the extracted beam are most conveniently determined by the extended variable quadrupole magnet method described in paragraph 4.4.1 and 4.4.2. First, the transverse profile of the extracted beam is recorded at viewer DFS_E.03 (see figure A.1) by means of a CCD camera synchronized with the extraction kicker magnet for three series of measurements associated with scans of the quadrupole magnets MQ_E.01, MQ_E.03, and MQ_E.06 (all other quadrupole magnets than the magnet which is being scanned has zero excitation). The intensity distribution of each camera image is projected into the horizontal and vertical planes, and the resulting one-dimensional intensity distribu-

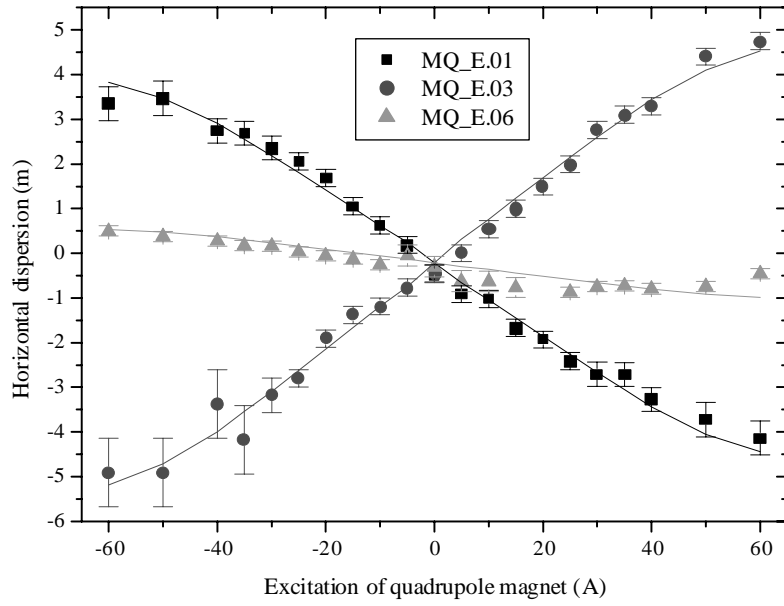


Figure 5.25: Horizontal dispersion at viewer DFS_E.03 for scans of quadrupole magnet MQ_E.01, MQ_E.03, and MQ_E.06. The line graphs indicate a single fit of the model (4.11) to the data of all three quadrupole magnet scans.

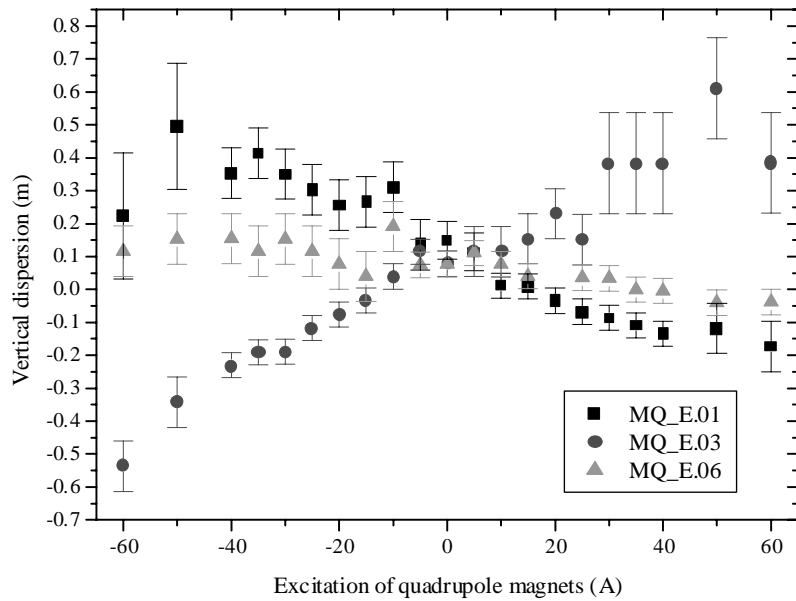


Figure 5.26: Vertical dispersion at viewer DFS_E.03 for scans of quadrupole magnet MQ_E.01, MQ_E.03, and MQ_E.06.

tions are characterized in terms of their weighted means and one standard deviation widths.

In addition, for each quadrupole magnet setting, the transverse profile of the beam is recorded for a reduced final excitation of the dipole magnets of the booster synchrotron of 2 A, equivalent to a beam momentum which is 1.16 MeV/c lower than that of the nominal setting. The associated displacement of the transverse beam profile readily provides the horizontal and vertical dispersions of the extracted beam at viewer DFS_E.03 for the each setting of the quadrupole magnets. The found transverse dispersions at viewer DFS_E.03 for all three quadrupole magnet scans are presented in figure 5.25 and 5.26, revealing that the vertical dispersion is much smaller than the horizontal dispersion as expected. The line graphs in figure 5.25 represent a single fit of the model (4.11) to the horizontal dispersion of all three quadrupole magnet scans with a reference point at the exit of the extraction septum magnet, yielding $D_x = -0.12 \pm 0.02$ m $D_x' = -0.175 \pm 0.005$ at the reference point. The excellent agreement of the model with all three scans for only two fit parameters demonstrates that the theoretical description of the extraction transfer line is accurate. However, the determined dispersion at the exit of the extraction septum is not in agreement with the

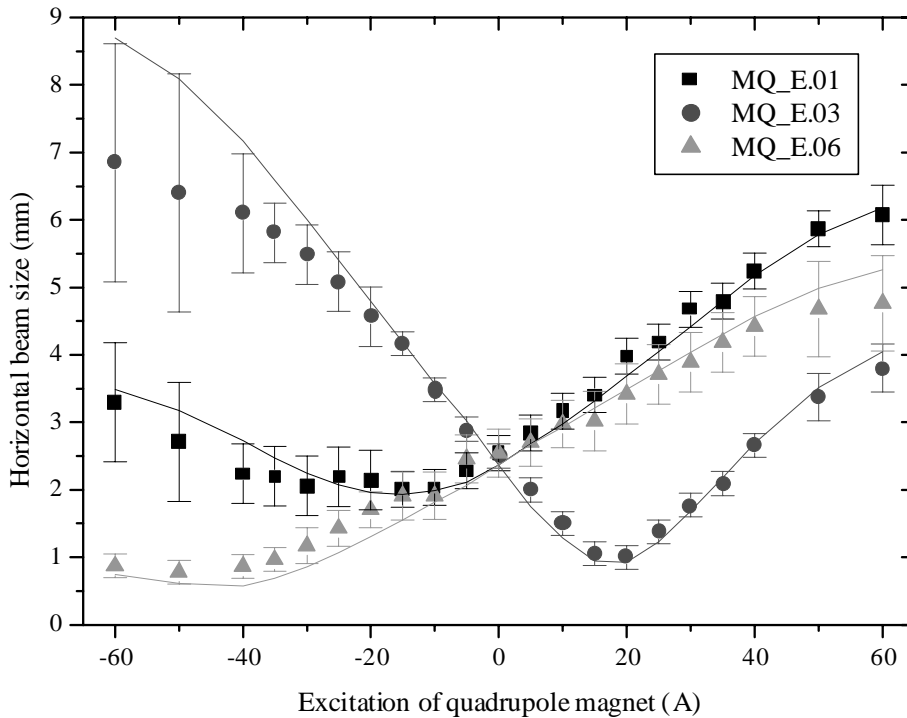


Figure 5.27: Horizontal beam size (one standard deviation) at viewer DFS_E.03 for scans of quadrupole magnet MQ_E.01, MQ_E.03, and MQ_E.06. The line graphs represent a single fit of the model (4.12) to the data of all three quadrupole magnet scans.

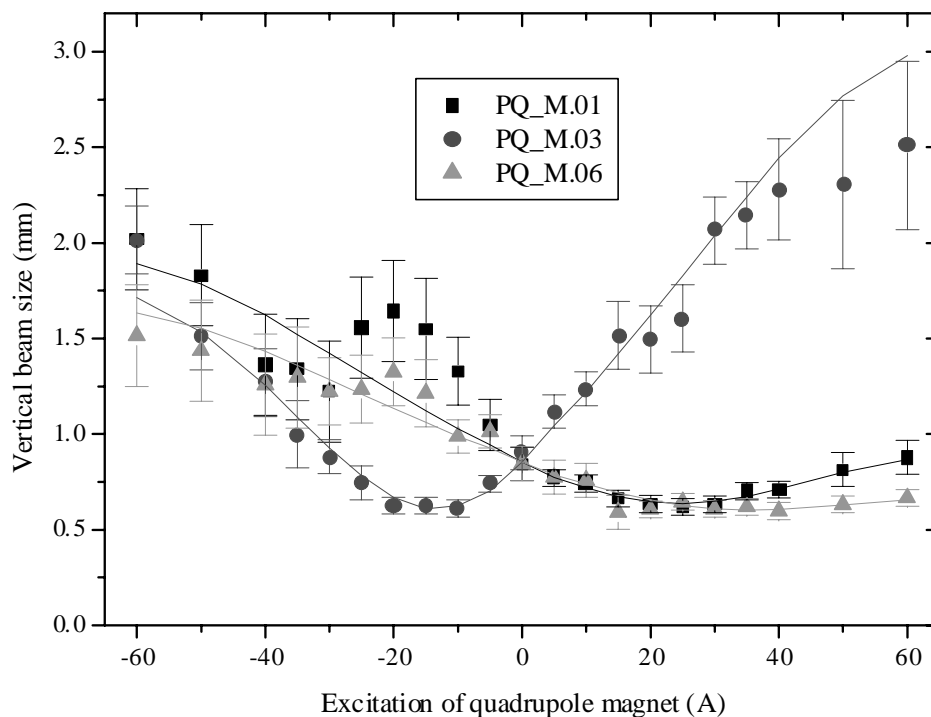


Figure 5.28: Vertical beam size (one standard deviation) at viewer DFS_E.03 for scans of quadrupole magnet MQ_E.01, MQ_E.03, and MQ_E.06. The line graphs indicate a single fit of the model (4.12) to the data of all three quadrupole magnet scans.

calculated dispersion of the booster synchrotron for unknown reasons.

In figure 5.27 and 5.28, the measured transverse beam sizes are plotted for all three quadrupole magnet scans. As in paragraph 4.4.2, it turns out that the data can only be modeled satisfactory if a finite resolution of the imaging system is built into the extended variable quadrupole magnet method. The minimum value of the vertical beam size of 0.6 mm for all three scans in figure 5.28 clearly demonstrates the effect of the finite resolution. A detailed investigation of the beam profile, for a setting of the quadrupole magnets for which the finite resolution dominates the vertical profile, reveals an asymmetric vertical intensity distribution which is attributed to the partial transparency of the fluorescent material, causing light from the interaction between the beam and the fluorescent material inside the viewer to be transmitted to the camera. As a result of the 45° rotation of the viewer with respect to the observation axis of the camera, the light emitted from inside of the fluorescent material produces a tail to the side of the viewer which is closest to the camera. The minimum vertical beam profile also has a small tail to the other side which is expected to be produced by scattering of the fluorescent light within the viewer.

For the horizontal plane, only scattering of the light within the fluorescent material contributes to resolution of the imaging system since the viewer is monitored from above by the camera, resulting in a horizontal resolution with a Gaussian width of 0.54 mm according to the minimum vertical profile. Using this result, a fit of the model (4.12) to all the three scans of the horizontal beam size in figure 5.27 yields the fit results $\epsilon_x=153\pm 12$ nm and $\sigma_p/p=(3.0\pm 0.6)\cdot 10^{-4}$. The found horizontal emittance of the extracted beam is in excellent agreement with the design value in table 3.1 and the horizontal emittance of the circulating beam determined in paragraph 5.3.4. Hence, the two-turn extraction process do not enlarge the horizontal emittance of the extracted beam notable. In addition, the imaging of the beam profile do not reveal any transverse displacement of the beam from shot to shot, demonstrating a good shot-to-shot stability of the kicker magnet. Finally, the found relative momentum spread is in good agreement with the design value in table 3.1 and the measured value for the circulating beam at 500 MeV in paragraph 5.3.3.

For the vertical plane, the Gaussian resolution is less well-defined due to the asymmetry induced by the tilt of the viewer. It is therefore considered as a free parameter of the fit of the model (4.12) to all three scans of the vertical beam size in figure 5.28. As the vertical dispersion can be neglected the fit results are $\epsilon_y=11\pm 2$ nm and $\sigma_{res}=0.602\pm 0.011$ mm. The determined vertical emittance of the extracted beam is significantly larger than that of the circulating beam established in paragraph 5.3.4. The disagreement is ascribed to a horizontal field of the extraction kicker magnet which vary throughout the passage of the extracted electron pulse, leading to a vertical emittance blowup. In fact, a horizontal field of the extraction kicker magnet has been observed by monitoring the coherent vertical oscillation of the beam in the booster synchrotron after a small excitation of the extraction kicker magnet, revealing a vertical field component of ~ 5 percent relative to the horizontal component.

5.7 Performance and improvements of the ANKA booster synchrotron

5.7.1 Comparison with other booster synchrotrons

In table 5.1, the main parameters of the ANKA booster synchrotron are compared with those of other booster synchrotrons at selected European synchrotron radiation facilities. The table reveals that the booster synchrotrons are very diverse in terms of circumference and beam energy, which makes a comparison difficult. However, it is interesting to compare the accelerated charge to full energy per second as this parameter essentially determines the filling time of the associated storage ring. The performance of the ANKA booster synchrotron with respect to this parameter is comparable to significantly larger and more expensive booster synchrotrons, as for example the SLS booster synchrotron. In fact, in terms of the accelerated charge to full energy per second per cost price, the ANKA booster synchrotron is comparable to or better than all the other booster synchrotrons. This is not only a conse-

quence of the good performance of the ANKA booster synchrotron, but also to a large extent a result of the excellent beam properties of the ANKA racetrack microtron.

Table 5.1: Main parameters of booster synchrotrons at selected European synchrotron radiation facilities.

	ANKA booster	BESSY II booster [8,9]	MAX II Booster [10,11]	ERSF Booster [12]	SLS booster [13,14]	Delta booster [15,16]
Circumference (m)	26.4	96	32.4	300	270	50.4
Injection energy (MeV)	53	50	100	200	100	75
Extraction energy (MeV)	500	1900	500	6000	2400	1500
Repetition frequency (Hz)	1	10	~0.01	10	3	~0.15
Quadrupole magnet families	1	2	3	2	3	5
Sextupole magnets	no	yes	yes	yes	yes	yes
Beam current at full energy (mA)	12	3	200 ^a	3	1.1 ^b	4
Accelerated charge to full energy per second (nC)	1.1	9.6	~0.2	30	3 ^b	~0.1
Type of pre-injector	rtm ^c	rtm	rtm	linac	linac	linac

^aThe booster synchrotron is operated in accumulation mode.

^bThe maximum charge of the extracted pulse train is 1 nC. It is assumed that the extraction efficiency is 100 percent and the length of the pulse train equals the circumference.

^c"rtm" is an abbreviation for "racetrack microtron".

5.7.2 Improvements of the lattice of the booster synchrotron

A disadvantage of the lattice of the booster synchrotron is the limited flexibility of the transverse tunes (see paragraph 3.2.1). The problem can be solved by exciting every second quadrupole magnet with two independent quadrupole supplies, facilitating an independent fine adjustment of the working point in both transverse planes without compromising the four-fold symmetry of booster synchrotron. The extra expense for this solution is rather small because the size of the two independent supplies is smaller than the present supply of all quadrupole magnets.

Another problem of the lattice is the rectangular shape of the iron block of the dipole magnets which at full excitation causes a finite quadrupole component at the center and at the end-poles of the magnet (see paragraph 5.2.1). Fortunately, the focusing effect of the quadrupole fields can to some extent be compensated by an adjustment of the ramping curve of the quadrupole magnets. The problem can be solved completely, however, if the

shape the iron block follows the curvature of the beam trajectory. Furthermore, the dipole magnets have a significant sextupole component at low excitation owing to a curvature of the effective field boundary at the end-poles which produces large static chromaticities. The problem can be reduced by adopting the curved shape of the iron block since this would reduce the saturation of the inner return yoke at the end-poles, providing a smaller variation of the effective field boundary with excitation. In addition, it would be an advantage to optimize the shape of the effective field boundary at low excitation because the beam here is much more sensitive to a small dynamic aperture and large chromaticities (the transverse beam size and the momentum spread are large at injection). Fortunately, the investigation of the booster synchrotron does not indicate that the large static chromaticities affect the performance of the machine. The eddy currents in the walls of the rectangular vacuum chamber inside the dipole magnet further increase the chromaticities during ramping (see paragraph 5.2.3). This contribution to the chromaticities can be reduced by employing an elliptical vacuum chamber which both facilitates a thinner wall thickness and has a geometry which gives rise to a smaller sextupole component at the position of the beam. Besides, the negative sextupole component of high conductivity metal strips along the sides of the vacuum chamber may balance the positive sextupole component of the vacuum chamber (see appendix D).

Finally, the alignment of the booster synchrotron would benefit from an alignment system of the magnetic components in which an adjustment in any of the three dimensions is not correlated to the two others. In addition, more bellows would provide a fully uncorrelated alignment of all magnetic elements. These improvements would facilitate a faster and more accurate alignment of all magnetic elements.

5.7.3 Improvements of the capture efficiency of the rf system

The large beam loss the first ~ 100 ms after injection, arising from a poor capture efficiency of the beam in the longitudinal rf bucket, is significantly reducing the circulating beam current in the booster synchrotron at full energy. The beam loss is likely to be reduced if the cavity is detuned according to (3.18) because this would suppress the effect of the transient beam loading at injection. In addition, the capture efficiency is expected to benefit if the amplitude loop is disabled throughout the injection process because the amplitude loop is believed to be perturbed by the large variations of the beam loading at injection which cannot be avoided even for the ideal detuning of (3.18).

In order to reach a capture efficiency close to 100 percent, the injected beam has to be pre-bunched at the rf frequency of the booster synchrotron. This can be achieved by a 499.65-MHz subharmonic pre-buncher in the injection transfer line of the racetrack microtron which longitudinally-focuses the beam in every sixth rf bucket of the rf system of the racetrack microtron (the resonance frequency of the racetrack microtron linac is exactly a factor of six larger than the rf frequency of the booster synchrotron), ideally without compromising the average output beam current of the racetrack microtron because the

beam loading is given by the average beam current in the linac. In this way, all electrons of the racetrack microtron beam can be injected into the center of the rf bucket of the booster synchrotron thus avoiding the loss of those electrons which otherwise are injected close to 180 degrees from the center of the bucket. In addition, the capture efficiency is enlarged since an electron in the center of the rf bucket is much less susceptible to small maladjustments of the injection process and perturbations of the longitudinal phase space by beam loading. This will also relax the settings of the injection process considerable, making the optimization of the injection process significantly easier. A subharmonic pre-buncher system has successfully been installed in the racetrack microtron in Lund, enhancing the capture efficiency of the MAX I synchrotron by a factor of four even though the total injected current decreased ~25 percent [17]. The only disadvantage of a subharmonic pre-buncher system is the additional cost for the pre-buncher and a new low-level rf generator for the racetrack microtron linac which can be phase-locked to the pre-buncher and the rf system of the booster synchrotron. The duration of the installation and running-in of the pre-buncher is not expected to prolong the commissioning period as the optimization of the booster synchrotron becomes easier with the pre-buncher.

The ANKA racetrack microtron has a 500-MHz electrostatic chopper in the injection transfer line which also could increase the fraction of electrons injected into the center of the rf bucket of the booster synchrotron. The chopper dumps those electrons which are not at the correct phase in the 500-MHz cycle, enabling an enhanced electron gun current for the same average beam loading of the racetrack microtron linac. This may increase the charge of every sixth rf bucket of the racetrack microtron linac by up to a factor of two, resulting in a higher capture efficiency in the booster synchrotron. However, the total captured beam current will only increase provided those electrons which are dumped by the chopper anyway are not captured by the rf system of the booster synchrotron. In practice, only a modest increase of the captured beam current is expected with the chopper. At least, a synchronization of the chopper and the linac of the racetrack microtron is foreseen for any improvements, requiring the installation of a new low-level rf generator of the linac.

Alternatively, the injection efficiency can be increased by adopting a new lattice of the booster synchrotron with a much smaller horizontal dispersion, in particular at the two septa, increasing the momentum acceptance of the lattice. As a result, the acceptable rf voltage at injection can be increased considerable according to (3.11), reducing the harmful effect of beam loading. This can most conveniently be achieved by inserting strong horizontally-focusing quadrupole magnets between the dipole magnets and including a vertically-focusing gradient in the dipole magnets, facilitating dispersion-free long straight sections without compromising the length of the long straight sections or the total length of the lattice. The lattice is similar to that of a proposal for a new booster synchrotron of MAX II [18]. It is also believed that the lattice will enhance the performance of the multi-turn injection process since a zero horizontal dispersion at the injection septum is expected to reduce the beam loss of the already injected beam on the inside of the injection septum

sheet. Finally, the new lattice has a much smaller horizontal emittance than the present lattice of the ANKA booster synchrotron. Although, the new lattice will increase the cost price of the ANKA injector owing to more magnetic elements, more complicated dipole magnets, and the requirement of two relatively large quadrupole supplies, the extra cost is modest in comparison with the benefits of the new lattice.

Finally, a higher injection energy is likely to increase the capture efficiency due to a larger rf voltage for the same longitudinal acceptance (see (3.11)) and a more effective synchrotron radiation damping of all degrees of freedom. However, the advantages are likely to be balanced by a lower output beam current of the racetrack microtron. Hence, the cost for increasing the injection energy is more effectively used for, for example, implementation of a subharmonic pre-buncher.

5.7.4 Improvements of the extraction process

The main problem of the extraction process of the booster synchrotron is the large integrated leak field of the extraction septum magnet of ~ 50 Gm. A detailed simulation of the extraction septum magnet reveals that the leak field at the position of the beam can be reduced radically if the present stainless steel vacuum chamber, separating the septum magnet and the beam, is replaced by a highly permeable iron vacuum chamber because the iron effectively trap the magnetic flux of the leak field before it penetrates into the vacuum chamber. Unfortunately, the installation of iron vacuum chamber requires a difficult rebuilding of the septum magnet and the associated vacuum chambers. Alternatively, the closed orbit deviation produced by the leak field can be reduced by a factor 3.5 without any hardware modifications by decreasing the horizontal tune to 1.7 because the leak field is a dipole field error of the lattice (see (3.5)). For this working point, a beam current comparable to that of the nominal working point can be stored according to figure 5.1.

As a consequence of the leak field, the beam cannot be bumped as close to the extraction septum sheet as desired, even with the compensation of the leak field by the ramped corrector magnet. This could be the reason why the two-turn extraction process was first observed to provide an extracted beam. However, the large extra reserve of the power supplies of the bumper windings and the extraction kicker magnet in case of the two-turn extraction process suggests that a one-turn extraction process is feasible. At least, the one-turn extraction process is possible if the shielding of the leak field is improved or the horizontal tune is decreased to 1.70. The one-turn extraction process is preferable because it is less sensitive to variations of the magnet field of the kicker magnet during the passage of the electron pulse (see paragraph 5.5.2) and produces a longer extracted electron pulse. In addition, the constant flattop of the excitation pulse of the kicker magnet throughout the passage of the part of the beam which is extracted may increase the extraction efficiency to 100 percent.

Finally, the extracted current can be enlarged ~ 5 percent by increasing the low-level drive power which at present is too low to produce a sufficient quantum lifetime at full beam

energy. In particular, a higher low-level drive power is important if the capture efficiency is improved, resulting in a higher beam current at full energy. The available generator power can also be enlarged by increasing the coupling coefficient κ between the rf transmission line and the rf cavity from 1.04 to 1.4 which is the optimum value for a beam current of 10 mA and a cavity voltage of 25 kV.

References:

- [1] A. W. Chao, *Physics of Collective Beam Instabilities in High Energy Accelerators*, John Wiley & Sons, New York, 1993, p. 206
- [2] F. Zimmermann, *Measurement and Correction of Accelerator Optics*, in *Beam Measurement*, Proc. of the Joint US-CERN-Japan-Russia School on Particle Accelerators, edited by S-i. Kurokawa *et al.*, Montreux 1998 (World Scientific, Singapore, 1999), p. 21
- [3] L. Rinolfi, *Longitudinal Beam Dynamics*, in Proc. Joint Universities Accelerator School, 1998, Geneva (unpublished)
- [4] A. Wrulich, *Single-Beam Lifetime*, in Proc. of Fifth General Accelerator Physics Course, CERN Accelerator School, Jyväskylä, Finland, 1992, edited by S. Turner (CERN, Geneva, 1994), p. 409
- [5] R. H. Riemann, *Bunched Beam Diagnostics*, AIP Conf. Proc. **184**, p. 431 (1989)
- [6] G. R. Lambertson, *Electromagnetic Detectors*, in Proc. Frontiers of Particle Beams; Observation, Diagnosis and Correction, Capri, 1988, edited by M. Month and S. Turner (Lecture Notes in Physics **343**, Springer-Verlag, Berlin, 1989), p. 380
- [7] H. Wiedemann, *Particle Accelerator Physics*, Springer-Verlag, Berlin, 1993, p. 276
- [8] M. Abo-Bakr *et al.*, in Proc. European Part. Acc. Conf., Barcelona, 1996, p. 527
- [9] M. Abo-Bakr *et al.*, in Proc. European Part. Acc. Conf., Stockholm, 1998, p. 436
- [10] M. Eriksson, Nucl. Instr. and Meth. **196**, p. 331 (1982)
- [11] Å. Andersson and L.-J. Lindgren, in Proc. European Part. Acc. Conf., Barcelona, 1996, p. 2494
- [12] Project team, in Proc. Part. Acc. Conf., Washington, D. C., 1993, p. 1427
- [13] W. Joho *et al.*, in Proc. European Part. Acc. Conf., Stockholm, 1998, p. 584
- [14] The internet site <http://slsbd.psi.ch/pub/comm/>.
- [15] K. Wille and DELTA group, in Proc. European Part. Acc. Conf., Barcelona, 1996, p. 95
- [16] J. Friedl and DELTA group, in Proc. Part. Acc. Conf., Vancouver, 1997, p. 724
- [17] Peter Röjssel, Nucl. Instr. and Meth. **A304**, p. 258 (1991)
- [18] M. Eriksson *et al.*, in Proc. European Part. Acc. Conf., Stockholm, 1998, p. 1468

Chapter 6

Summary

The 500-MeV ANKA injector is the pre-accelerator of the 2.5-GeV ANKA synchrotron radiation source at Forschungszentrum Karlsruhe. The injector consists of a 53-MeV racetrack microtron, a 500-MeV booster synchrotron, and associated transfer lines.

A 53-MeV racetrack microtron has been chosen as injector of the booster synchrotron because it is a compact design which produces an electron beam of very high quality. The most significant design parameters of the ANKA racetrack microtron and the corresponding achieved parameters are listed in table 2.1, demonstrating that the racetrack microtron performs according to specifications or better. For example, the observed output beam current of the ANKA racetrack microtron of 16 mA is significantly beyond the associated design value of 10 mA. According to table 4.1, the output beam current is comparable to that of other racetrack microtrons, and even matches that of most of the modern linear accelerators in table 4.1, except for very short electron pulses. The theoretical analysis of the beam-linac interaction suggests that the total beam current in the linac of the ANKA racetrack microtron cannot exceed 329 mA as a result of a positive feedback mechanism between the electron beam and the linac field, causing beam instability. The observed beam current in the linac is slightly below 300 mA for an output beam current of 14 mA, indicating that an output beam current significantly above 16 mA cannot be expected. However, it should be possible to increase the output beam current if the threshold for the beam instability is enlarged by a larger coupling coefficient between the waveguide and the linac. Besides, the output beam current can be increased substantially by longitudinally focusing the cw beam of the electron gun into the longitudinal acceptance of the rf system by a fundamental-frequency pre-buncher in the injection transfer line of the racetrack microtron. This will reduce the large loss of electrons outside the longitudinal acceptance at low energy, providing more output beam current for the same total beam current in the linac. Nevertheless, this modification of the racetrack microtron requires a new low-level rf system which can be synchronized with the pre-buncher.

According to table 4.1, the measured momentum spread and transverse emittances of the output beam are smaller than those of other selected racetrack microtrons, and significantly smaller than those of selected modern linear accelerators. For the present application,

this is a considerable advantage as the injection efficiency of the multi-turn injection process in the booster synchrotron strongly favors a small momentum spread and small transverse emittances of the output beam of the pre-injector. A theoretical study of the longitudinal dynamics of the racetrack microtron reveals that the small momentum spread is a result of the recirculation of the beam which preserves the characteristic momentum spread of a single linac passage, causing the relative momentum spread to decrease inversely with the number of recirculations. In addition, the recirculation facilitates a more efficient conversion of rf power into beam power than that of linear accelerators. Therefore, the ANKA racetrack microtron is superior to linear accelerators of comparable cost as an injector for synchrotrons.

The lattice of the 500-MeV booster synchrotron is different from that of all existing booster synchrotrons. In comparison with other booster synchrotrons, the lattice is relatively simple with only one quadrupole magnet family and no sextupole magnets (see table 5.1), reflecting a compromise between flexibility and cost price. The limited tune flexibility resulting from only one family of quadrupole magnets gives rise to very strict tolerances of the magnetic components, in particular, the dipole magnets. In fact, small deviations of the present dipole magnets from the design have shifted the working point, fortunately without any significant decline of the performance of the booster synchrotron. The problem can be solved by a fine-tuning of the working point by means of two independent quadrupole supplies, exciting every second quadrupole magnet, considerably improving the tune flexibility of the lattice. In addition, a curvature of the effective field boundaries at the end-poles of the dipole magnets produce large static chromaticities at the injection energy which cannot be corrected (no sextupole magnets), but fortunately no significant negative effect on the beam quality is observed. The curvature of the effective field boundary can be reduced considerable if the rectangular shape iron yokes of dipole magnets is changed to a curved design which follows the curvature of the beam trajectory. In addition, the field boundary should be optimized at the injection energy at which point the momentum spread and size of the beam are largest.

All the measured lattice and beam properties of the ANKA booster synchrotron and the associated design values are summarized in table 3.1. The observed horizontal emittance and momentum spread of the circulating beam in the booster synchrotron are in excellent agreement with lattice calculations. In addition, the beam current at full beam energy exceeds the design value by ~60 percent. A comparison with the other booster synchrotrons in table 5.1 reveals that the charge accelerated to full energy per second is comparable to or better than that of more expensive booster synchrotrons. The impressive performance of the ANKA booster synchrotron is to a large extent a consequence of the excellent beam properties of the ANKA racetrack microtron.

An investigation of the substantial beam loss the first ~100 ms after injection, resulting from a poor capture efficiency, indicates that the output beam current of the ANKA injector can be increased by a careful adjustment of the detuning of the cavity, reducing the harmful

Summary

effect of transient beam loading at injection. Disabling the amplitude loop during the injection is also likely to bring down the negative influence of transient beam loading. Nevertheless, in order to achieve a capture efficiency close to 100 percent, a subharmonic pre-buncher operating at the rf frequency of the booster synchrotron should be installed in the injection transfer line of the racetrack microtron. The pre-buncher would facilitate an injection of all electrons of the racetrack microtron beam in the center of the longitudinal bucket of the booster synchrotron (ideally without compromising the output beam current of the racetrack microtron), resulting in a capture of all electrons and a lower sensitivity of the electrons towards perturbations of the longitudinal phase space by beam loading effects. However, the pre-buncher necessitates a new low-level rf system of the racetrack microtron which can be synchronized with the rf system of the booster synchrotron. Although this increases the cost price of the subharmonic pre-buncher considerably, the expense is modest relative to that of the whole injector considering the significant enhancement of both the performance and the reliability of the injector.

The leak field of the extraction septum magnet is observed to produce a large closed orbit displacement prior to the extraction of the beam from the booster synchrotron. At first, this hindered an extraction of the beam because the leak field peaks before the septum magnet field is appropriate for beam extraction. The problem was reduced by additional shielding the septum magnet and by exciting a corrector magnet close to the leak field, making an extraction of the beam possible. However, a detailed analysis of the beam behavior after the activation of the extraction kicker magnet reveals that the beam is extracted $7/4$ revolutions after the first deflection by the kicker magnet (two-turn extraction process) as opposed to the expected $3/4$ revolution (one-turn extraction process). The reason is a combination of a too small displacement of the beam towards the extraction septum prior to the extraction process and an additive effect of two successive deflections by the extraction kicker magnet. Fortunately, even for the two-turn extraction process, the extraction efficiency is about 90 percent, and measurements of the horizontal emittance and the momentum spread of the extracted beam agree with the those of the circulating beam, demonstrating that the two-turn extraction process does not deteriorate the beam quality. Only the vertical emittance increases during the extraction process due to a finite horizontal component of the magnet field of the extraction kicker magnet. Nevertheless, the one-turn extraction process is more advantageous because it produces a longer extracted electron pulse and reduces the sensitivity of the electron pulse towards a variation of the kicker magnet field. Owing to the large excitation reserve of both the bumper windings and the kicker magnet supply, the one-turn extraction process should be feasible, unless the leak field impedes the beam from being displaced close enough to the extraction septum. At least, the one-turn extraction process can be accomplished if the shielding of the septum magnet is improved by a highly permeable iron vacuum chamber or the horizontal tune is decreased to 1.7 for which the closed orbit displacement by the leak field is a factor 3.5 smaller.

In conclusion, although the lattice of the booster ANKA synchrotron is relatively sim-

ple, the ANKA injector provides an intense electron beam of very high quality, comparable to that of more expensive injectors. However, the simplicity has the price of a limited tune flexibility and large static chromaticities. Fortunately, these disadvantages can be reduced significantly in a future design by two independent quadrupole magnet supplies and by adopting dipole magnets with a curved shape in combination with a careful field mapping the dipole magnets in the production phase. Finally, the analysis of both the racetrack microtron and the booster synchrotron suggests that the performance and the reliability of the ANKA injector can be increased significantly for a modest extra investment. It is realistic that these revisions of the injector design will increase the output charge of the injector by a factor of two. This will make the ANKA injector an even more attractive injector for future synchrotron light sources.

Appendix A

Detailed drawing of the ANKA injector

Figure A.1: Detailed drawing of the ANKA injector, including names for all magnetic and diagnostic components (except for the racetrack microtron).

Appendix B

Storage ring synchrotron radiation sources

Location	Ring	Electron energy (GeV)	Type	Status
ARMENIA				
Yerevan	Candle	3.2	dedicated	design
AUSTRALIA				
	Boomerang	3	dedicated	design
BRAZIL				
Campinas	LNLS-1	1.35	dedicated	in operation
	LNLS-2	2	dedicated	design
CANADA				
Saskatoon	CLS	2.9	dedicated	under constr. ^a
CHINA				
Beijing	BSRF	1.5-2.8	partly dedicated	in operation
	BLS	2.2-2.5	dedicated	design
Hefei	NSRL	0.8	dedicated	in operation
Shanghai	SSRF	3.5	dedicated	design
DENMARK				
Aarhus	ASTRID	0.58	partly dedicated	in operation
	ASTRID 2000	0.8	dedicated	design
FRANCE				
Grenoble	ESRF	6	dedicated	in operation

Appendix B

Orsay	DCI	1.8	dedicated	in operation
	SuperACO	0.8	dedicated	in operation
	SOLEIL	2.5-2.75	dedicated	design
GERMANY				
Berlin	BESSY II	1.7-1.9	dedicated	in operation
Bonn	ELSA	1.5-3.5	partly dedicated	in operation
Dortmund	DELTA	1.5	dedicated	in operation
Hamburg	DORIS III	4.5	dedicated	in operation
	PETRA II	7-14	partly dedicated	in operation
Karlsruhe	ANKA	2.5	dedicated	in operation
INDIA				
Indore	INDUC-I	0.45	dedicated	in operation
	INDUC-II	2	dedicated	under constr. ^a
ITALY				
Frascati	DAFNE	0.51	parasitic	in operation
Trieste	ELETTRA	2-2.4	dedicated	in operation
JAPAN				
Hiroshima	HISOR	0.7	dedicated	under constr. ^a
Ichihara	NANO-HANA	1.5-2	dedicated	design
Kashiwa	VSX	1-1.6	dedicated	design
Kusatsu	Rits SR	0.575	dedicated	design
Kyoto	KSR	0.3	dedicated	under constr. ^a
Nishi Harima	SPring-8	8	dedicated	in operation
	NewSUBARU	1-1.5	dedicated	under constr. ^a
	NIJI III	0.6	dedicated	in operation
Okasaki	UVSOR	0.75	dedicated	in operation
	UVSOR-II	1.0	dedicated	design
Osaka	Kansai SR	1.8	dedicated	design
Sendai	TLS	1.5	dedicated	design
Tsukuba	TERAS	0.8	dedicated	in operation
	NIJI II	0.6	dedicated	in operation
	NIJI IV	0.5	dedicated	in operation
	Photon Factory (KEK)	2.5	dedicated	in operation
	Accum. Ring (KEK)	6		planned re-building

Storage ring synchrotron radiation sources

JORDAN				
Allaan	SESAME	1.0	dedicated	design
KOREA				
Pohang	Pohang Light Source	2	dedicated	in operation
Seoul	CESS	0.1	dedicated	in operation
RUSSIA				
Dubna	DELSY	1.2	dedicated	under constr. ^a
Moscow	Siberia I	0.45	dedicated	in operation
	Siberia II	2.5	dedicated	in operation
Novosibirsk	VEPP-2M	0.7	partly dedicated	in operation
	VEPP-3	2.2	partly dedicated	in operation
	VEPP-4M	5-7	partly dedicated	in operation
Zelenograd	Siberia-SM	0.8	dedicated	under constr. ^a
	TNK	1.2-1.6	dedicated	under constr. ^a
SINGAPORE				
Singapore	HELIOS 2	0.7	dedicated	under constr. ^a
SPAIN				
Barcelona	LLS	2.5	dedicated	design
SWEDEN				
Lund	MAX I	0.55	dedicated	in operation
	MAX II	1.5	partly dedicated	in operation
	MAX III	0.7	dedicated	under constr. ^a
SWITZERLAND				
Villigen	SLS	2.4	dedicated	under constr. ^a
TAIWAN				
Hsinchu	SRRC	1.3-1.5	dedicated	in operation
THAILAND				
Nakhon Ratchasima	SIAM	1-1.3	dedicated	under constr. ^a
UKRAINE				
Kharkov		0.75-2	partly dedicated	in operation
Kiev	ISI-800	0.7-1.0	dedicated	design
UK				
Daresbury	SRS	2	dedicated	in operation
	DIAMOND	3.0	dedicated	design

Appendix B

USA				
Argonne, IL	APS	7	dedicated	in operation
Baton Rouge, LA	CAMD	1.3-1.5	dedicated	in operation
Berkeley, CA	ALS	1.5-1.9	dedicated	in operation
Durham, NC	DFELL	1-1.3	dedicated	in operation
Gaithersburg, MD	SURF III	0.4	dedicated	in operation
Ithaca, NY	CESR	5.5	partly dedicated	in operation
Raleigh, NC	NC STAR	2.5	dedicated	design
Stanford, CA	SPEAR	3	dedicated	in operation
Stoughton, WI	Aladdin	0.8-1	dedicated	in operation
Upton, NY	NSLS I	0.8	dedicated	in operation
	NSLS II	2.5-2.8	dedicated	in operation

^aAs of March 2001.

Appendix C

Lattice input files

C.1 Lattice input file of the ANKA racetrack microtron (OPTIM 2.0 format)

```
OptiM
Energy[MeV]=10.67   Mass[MeV]=0.511006
Emittance: ex[cm]=1.3e-05  ey[cm]=1e-06  DP/P=0.0007
Initial:   BetaX[cm]=220  BetaY[cm]=300
          AlfaX=-0.02   AlfaY=0.42  Qx=0  Qy=0
          DispersX[cm]=0  DispersY[cm]=0
          Dsp_PrimeX=0  DspPrimeY=0
          X[cm]=0.000  Y[cm]=0.000  Z[cm]=0.000  S[cm]=0.000
          tetaX[deg]=0  tetaY[deg]=0

# Elements (from second passage of linac):
# O2: Drift from linac to solenoid
# O3: Drift from solenoid to horizontally-focusing quadrupole magnet
# O4: Drift from horizontally-focusing quadrupole magnet to main dipole magnet
# O5: Drift between main dipole magnets
# O6: Drift from main dipole magnets to linac
# AC: Linac
# CC: Solenoid (0.50 A excitation)
# QC: Horizontally-focusing quadrupole magnet (0.20 A excitation)
# D1-D10: Main dipole magnets (the field strength corresponds a 180 degrees deflection)
# XQ1: Only vertically-focusing thin lens located 30/150 degrees within the main dipole.
# XQ2: Only vertically-focusing thin lens located 90 degrees within the main dipole.

begin lattice. Number of periods=1
O2 CC O3 QC O4 D2 XQ1 D2 D2 XQ2 D2 D2 XQ1 D2 O5 D2 XQ1 D2 D2 XQ2 D2 D2 XQ1 D2 O6 AC
O2 CC O3 QC O4 D3 XQ1 D3 D3 XQ2 D3 D3 XQ1 D3 O5 D3 XQ1 D3 D3 XQ2 D3 D3 XQ1 D3 O6 AC
O2 CC O3 QC O4 D4 XQ1 D4 D4 XQ2 D4 D4 XQ1 D4 O5 D4 XQ1 D4 D4 XQ2 D4 D4 XQ1 D4 O6 AC
O2 CC O3 QC O4 D5 XQ1 D5 D5 XQ2 D5 D5 XQ1 D5 O5 D5 XQ1 D5 D5 XQ2 D5 D5 XQ1 D5 O6 AC
O2 CC O3 QC O4 D6 XQ1 D6 D6 XQ2 D6 D6 XQ1 D6 O5 D6 XQ1 D6 D6 XQ2 D6 D6 XQ1 D6 O6 AC
O2 CC O3 QC O4 D7 XQ1 D7 D7 XQ2 D7 D7 XQ1 D7 O5 D7 XQ1 D7 D7 XQ2 D7 D7 XQ1 D7 O6 AC
O2 CC O3 QC O4 D8 XQ1 D8 D8 XQ2 D8 D8 XQ1 D8 O5 D8 XQ1 D8 D8 XQ2 D8 D8 XQ1 D8 O6 AC
O2 CC O3 QC O4 D9 XQ1 D9 D9 XQ2 D9 D9 XQ1 D9 O5 D9 XQ1 D9 D9 XQ2 D9 D9 XQ1 D9 O6 AC
O2 CC O3 QC O4 D10 XQ1 D10 D10 XQ2 D10 D10 XQ1 D10
end lattice
```

Appendix C

```

begin list
O2      L[cm]=9.5225
O3      L[cm]=17.9625
O4      L[cm]=14.355
O5      L[cm]=124.4
O6      L[cm]=34.83
AC      L[cm]=40      Ncell=8  Eff_L[cm]=2.4  A[MeV]=5.5422  Phase[deg]=17  WaveL[cm]=10
CC      L[cm]=4        B[kG]=0.25
QC      L[cm]=3.73    G[kG/cm]=0.02  Tilt[deg]=0
D2      L[cm]=1.6755  B[kG]=11.6429  G[kG/cm]=0    Tilt[deg]=0
D3      L[cm]=2.5133  B[kG]=11.4474  G[kG/cm]=0    Tilt[deg]=0
D4      L[cm]=3.351   B[kG]=11.3493  G[kG/cm]=0    Tilt[deg]=0
D5      L[cm]=4.1888  B[kG]=11.2893  G[kG/cm]=0    Tilt[deg]=0
D6      L[cm]=5.0265  B[kG]=11.2503  G[kG/cm]=0    Tilt[deg]=0
D7      L[cm]=5.8643  B[kG]=11.221   G[kG/cm]=0    Tilt[deg]=0
D8      L[cm]=6.702   B[kG]=11.2004  G[kG/cm]=0    Tilt[deg]=0
D9      L[cm]=7.5398  B[kG]=11.1832  G[kG/cm]=0    Tilt[deg]=0
D10     L[cm]=8.3776  B[kG]=11.17    G[kG/cm]=0    Tilt[deg]=0
XQ1     Energy increase[MeV]=0
1  0  0  0  0  0
0  1  0  0  0  0
0  0  1  0  0  0
0  0  -0.0001786  1  0  0
0  0  0  0  1  0
0  0  0  0  0  1
XQ2     Energy increase[MeV]=0
1  0  0  0  0  0
0  1  0  0  0  0
0  0  1  0  0  0
0  0  -0.0003571  1  0  0
0  0  0  0  1  0
0  0  0  0  0  1
end list of elements

```

C.2 Lattice input file of the ANKA booster synchrotron (OPTIM 2.0 format)

```

OptiM
Energy[MeV]=500  Mass[MeV]=0.511006
Emittance: ex[cm]=1.50009e-05  ey[cm]=1e-06  DP/P=0.000337131
Initial:  BetaX[cm]=825.591  BetaY[cm]=166.916
        AlfaX=4.07631e-16  AlfaY=5.63012e-17
        DispersX[cm]=181.27  DispersY[cm]=0
        Dsp_PrimeX=7.39426e-17  DspPrimeY=0
        X[cm]=0.000  Y[cm]=0.000  Z[cm]=0.000  S[cm]=0.000
        tetaX[deg]=0  tetaY[deg]=0

```

```

# Elements:
#O1: Drift

```

Lattice input files

```
#O2: Drift
#O3: Drift
#QF: Horizontally-focusing quadrupole magnet
#D: Dipole magnet
#G: Edge field of dipole magnet

begin lattice. Number of periods=1
O1 QF O2 G D G O3 G D G O2 QF O1
O1 QF O2 G D G O3 G D G O2 QF O1
O1 QF O2 G D G O3 G D G O2 QF O1
O1 QF O2 G D G O3 G D G O2 QF O1
end lattice
begin list
O1      L[cm]=99.18
O2      L[cm]=48.3985
O3      L[cm]=72.437
QF      L[cm]=15.64   G[kG/cm]=0.497696   Tilt[deg]=0
D       L[cm]=130.724 B[kG]=10.031   G[kG/cm]=0   Tilt[deg]=0
G       B[kG]=10.031   Angle[deg]=22.74   EffLen[cm]=1.827   Tilt[deg]=0
end list of elements
```


Appendix D

Sextupole field of eddy currents in a rectangular vacuum chamber

D.1 Eddy current-induced field from top and bottom walls

Consider the infinitely long rectangular vacuum chamber of height $2h$ and width $2b$ shown in figure D.1a, which is embedded in an time-dependent homogeneous magnetic field $\mathbf{B}(t)=(0,B_y(t),0)$. According to Faraday's law of induction, the time-variation of the magnetic field will induce an eddy current density $\mathbf{j}(x,y,z)$ in the walls of the vacuum chamber. The symmetry of the vacuum chamber requires the current density to fulfil the following symmetry relations in the top and bottom walls:

$$\mathbf{j}(x, y, z) = (0, 0, j_z(x)) \quad (\text{D.1})$$

$$j_z(x) = -j_z(-x) \quad . \quad (\text{D.2})$$

Applying the symmetry relations, Faraday's law of induction, and Ohm's law on the closed

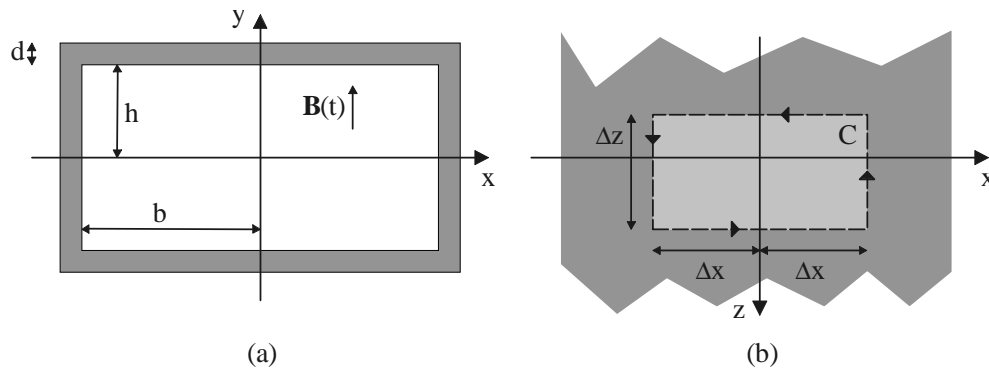


Figure D.1: Schematic of the rectangular vacuum chamber. (a) Profile. (b) Top view.

Appendix D

curve C in the top wall of the vacuum chamber (see figure D.1b), one finds

$$\begin{aligned} -\frac{d}{dt} \int_S \mathbf{B} \cdot \mathbf{n} dS &= \oint_C \mathbf{E} \cdot d\mathbf{l} = \frac{1}{\sigma} \oint_C \mathbf{j} \cdot d\mathbf{l} = \\ &= \frac{1}{\sigma} (-j_z(\Delta x)\Delta z + j_z(-\Delta x)\Delta z) = -\frac{2}{\sigma} j_z(\Delta x)\Delta z \quad , \end{aligned} \quad (\text{D.3})$$

where \mathbf{n} is a normal vector to the top wall, \mathbf{E} is the electric field in the wall, and σ is the conductivity of the wall material. Since the area within the curve C is $2\Delta x\Delta z$, the current density in the upper and lower walls becomes

$$\mathbf{j}(x, y, z) = (0, 0, \sigma x \frac{d}{dt} B_y) \quad . \quad (\text{D.4})$$

Using this result and assuming that the boundary conditions are not altered by any surrounding magnetic materials, the y component of the magnetic field produced by the eddy currents in the top wall is

$$\begin{aligned} B_y^{\text{eddy},1}(x, y, z) &= \frac{\mu_0}{4\pi} \int_{\text{wall}} \frac{(\mathbf{j}(x, y, z) \times (\mathbf{r} - \mathbf{r}'))_y}{|\mathbf{r} - \mathbf{r}'|^3} d^3 r' \\ &= \frac{\mu_0 \sigma}{4\pi} \frac{dB_y}{dt} \int_{-b-d}^{b+d} \int_h^{h+d} \int_{-\infty}^{\infty} \frac{x(x-x')}{\left((x-x')^2 + (y-y')^2 + (z-z')^2\right)^{3/2}} dz' dy' dx' \quad , \end{aligned} \quad (\text{D.5})$$

where d is the thickness of the wall [1]. Only considering $x \ll b$, one obtains

$$\begin{aligned} B_y^{\text{eddy},1}(x, y, z) &= \frac{\mu_0 \sigma}{4\pi} \frac{dB_y}{dt} \int_h^{h+d} \left(-4(b+d) + 4|y-y'| \arctan\left(\frac{b+d}{|y-y'|}\right) + \right. \\ &\quad \left. \frac{4(b+d)^3 x^2}{\left((b+d)^2 + y^2 - 2yy' + y'^2\right)^2} \right) dy' \quad . \end{aligned} \quad (\text{D.6})$$

If it also is assumed that $d \ll h$ and $d \ll b$, the magnetic field produced by eddy currents in the top wall of the rectangular vacuum chamber finally becomes

$$B_y^{\text{eddy},1}(x, y, z) = \frac{\mu_0 \sigma d}{\pi} \frac{dB_y}{dt} \left(-b + |y-h| \arctan\left(\frac{b}{|y-h|}\right) + \frac{b^3 x^2}{(b^2 + y^2 - 2hy + h^2)^2} dy \right) \quad . \quad (\text{D.7})$$

The similar expression for the bottom wall is

$$B_y^{\text{eddy},2}(x, y, z) = \frac{\mu_0 \sigma d}{\pi} \frac{dB_y}{dt} \left(-b + |y+h| \arctan\left(\frac{b}{|y+h|}\right) + \frac{b^3 x^2}{(b^2 + y^2 + 2hy + h^2)^2} dy \right) \quad . \quad (\text{D.8})$$

Sextupole field of eddy currents in a rectangular vacuum chamber

The x^2 terms in (D.7) and (D.8) demonstrate that the magnetic field produced by eddy currents in the top and bottom walls has a sextupole component in the center of the vacuum chamber.

D.2 Eddy current-induced field from sides of vacuum chamber

For the wall of the rectangular vacuum chamber at $x=b$, the symmetry relations for the current density are

$$\mathbf{j}(x, y, z) = (0, 0, j_z(x)) \quad (\text{D.9})$$

$$j_z(x) = -j_z(2b + d - x) \quad . \quad (\text{D.10})$$

In analogy with above, the eddy current density in the wall can be obtained from the symmetry relations, Faraday's law of induction, and ohm's law:

$$\mathbf{j}(x, y, z) = (0, 0, \sigma(x - b - d/2) \frac{d}{dt} B_y) \quad . \quad (\text{D.11})$$

Again assuming that the boundary conditions are not changed by any surrounding magnetic materials, the y component of the magnetic field produced by the eddy currents in the wall at $x=b$ is

$$\begin{aligned} B_y^{eddy,3}(x, 0, z) &= \frac{\mu_0}{4\pi} \int_{wall} \frac{(\mathbf{j}(x, y, z) \times ((x, 0, z) - \mathbf{r}'))_y}{|\mathbf{r} - \mathbf{r}'|^3} d^3 r' \\ &= \frac{\mu_0 \sigma}{4\pi} \frac{dB_y}{dt} \int_b^{b+d} \int_{-h}^h \int_{-\infty}^{\infty} \frac{-b^2 - bd - \frac{1}{4}d^2 - bx - \frac{1}{2}dx + (2b + d + x)x' - x'^2}{((x - x')^2 + y'^2 + (z - z')^2)^{3/2}} dz' dy' dx' \quad (\text{D.12}) \\ &= \frac{\mu_0 \sigma}{4\pi} \frac{dB_y}{dt} \int_b^{b+d} \frac{(2b + d + 2x - 2x')(-2b - d + 2x') \arctan(a/|x - x'|)}{|x - x'|} dx' \quad . \end{aligned}$$

Assuming that $d \ll b$, the magnetic field becomes

$$B_y^{eddy,3}(x, 0, z) = -\frac{\mu_0 \sigma d^3}{12\pi} \frac{dB_y}{dt} \frac{\arctan(a/|x - b|)}{|x - b|} \quad , \quad (\text{D.13})$$

and the analog expression for the wall at $x=-b$ is

$$B_y^{eddy,4}(x, 0, z) = -\frac{\mu_0 \sigma d^3}{12\pi} \frac{dB_y}{dt} \frac{\arctan(a/|x + b|)}{|x + b|} \quad . \quad (\text{D.14})$$

A series expansion of (D.13) and (D.14) with respect to x reveals that the magnetic field generated by the eddy currents in the walls at $x=\pm b$ has a non-vanishing sextupole term in the center of the rectangular vacuum chamber.

D.3 Sextupole strength of field produced by eddy currents

In general, an upright sextupole field has the form

$$B_x^{sextupol} = B\rho mxy \quad \text{and} \quad B_y^{sextupole} = \frac{B\rho}{2} m(x^2 - y^2) , \quad (\text{D.15})$$

where m is the sextupole strength, B is the strength of the dipole magnet field, and ρ is the bending radius of the beam trajectory in the dipole magnets. Hence, the total strength of the sextupole field produced by the eddy currents in the top and bottom of the rectangular vacuum chamber is

$$\begin{aligned} m_{12}(0, y, z) &= \frac{1}{B_y \rho} \left(\frac{d^2}{dx^2} (B_y^{eddy,1} + B_y^{eddy,2}) \right) \\ &= \frac{2\mu_0 \sigma d}{\pi B_y \rho} \frac{dB_y}{dt} \left(\frac{b^3}{(h^2 + b^2 - 2hy + y^2)^2} + \frac{b^3}{(h^2 + b^2 + 2hy + y^2)^2} \right) \end{aligned} \quad (\text{D.16})$$

for $x \ll b$, $d \ll b$, and $d \ll h$, which at the center of the vacuum chamber simplifies to

$$m_{12}(0,0, z) = \frac{4}{\pi} \frac{\mu_0 \sigma}{\rho} \frac{dB_y/dt}{B_y} \frac{db^3}{(h^2 + b^2)^2} . \quad (\text{D.17})$$

Similarly, for $d \ll b$ the eddy currents in the side walls of the rectangular vacuum chamber produce a sextupole field in the center of the chamber with a strength of

$$m_{34}(0,0, z) = \frac{1}{3\pi} \frac{\mu_0 \sigma}{B_y \rho} \frac{dB_y}{dt} \frac{d^3}{b^2} \left(\frac{h^3}{(h^2 + b^2)^2} - \frac{2h}{h^2 + b^2} - \frac{\arctan(h/b)}{b} \right) . \quad (\text{D.18})$$

However, this contribution to the sextupole strength can be neglected for a usual vacuum chamber design with thin walls because it is proportional to d^3 whereas the contribution from the top and bottom walls in (D.17) is proportional to d . In addition, it is observed that the sides of the vacuum chamber gives rise to a sextupole strength with the opposite sign of (D.17) as the term in brackets in (D.18) always is negative. This suggests that the total sextupole strength originating from all walls can be reduced significantly if the contributions from (D.17) and (D.18) have the same absolute size. This can be achieved by placing high conductivity metal strips along the sides of the vacuum chamber.

References:

- [1] J. D. Jackson, *Classical Electrodynamics*, John Wiley & Sons, New York, 1975, p. 173

Appendix E

Analysis of the synchrotron light imaging system

E.1 Waist of synchrotron light cone originating from a single electron

Assume that the synchrotron light cone, produced by a single electron, after the pinhole in figure 5.12 can be described by a Gaussian beam with a minimum waist of w_0 at a distance d_w behind the pinhole. The radius of curvature of the wave front and the waist of the Gaussian beam at the pinhole are thus given by

$$R_p = d_w + z_0^2/d_w \quad (\text{E.1})$$

$$w_p = w_0 \sqrt{1 + d_w^2/z_0^2} \quad , \quad (\text{E.2})$$

where $z_0 = \pi w_0^2/\lambda$ is the Rayleigh range of the Gaussian beam and λ is the wave length of the synchrotron light (is well-defined owing to the color filter in front of the CCD chip) [1]. Hence, the q parameter of the Gaussian beam at the pinhole is

$$q_p = \left(\frac{1}{R_p} + i \frac{\lambda}{\pi w_p^2} \right)^{-1} = d_w - i \frac{\pi w_0^2}{\lambda} \quad . \quad (\text{E.3})$$

Adopting the thin lens approximation, the transformation of the Gaussian beam from the pinhole to the lens, through the lens with a focal length f , and from the lens to the CCD chip is described by the matrix

$$\begin{pmatrix} A & B \\ C & D \end{pmatrix} = \begin{pmatrix} 1 & d_2 \\ 0 & 1 \end{pmatrix} \begin{pmatrix} 1 & 0 \\ -1/f & 1 \end{pmatrix} \begin{pmatrix} 1 & d_1 \\ 0 & 1 \end{pmatrix} = \begin{pmatrix} 1 - d_2/f & d_2 + d_1 - d_1 d_2/f \\ -1/f & 1 - d_1/f \end{pmatrix} \quad . \quad (\text{E.4})$$

Therefore, the q parameter at the CCD chip becomes

Appendix E

$$q_{CCD} = \left(\frac{1}{R_{CCD}} + i \frac{\lambda}{\pi w_{CCD}^2} \right)^{-1} = \frac{Aq_p + B}{Cq_p + D} \quad (\text{E.5})$$

which after some manipulations finally provides the waist of the synchrotron light cone, originating from a single electron, at the CCD chip:

$$w_{CCD} = \sqrt{\frac{(f(d_w + d_1 + d_2) - d_2(d_w + d_1))^2 \lambda^2}{\pi^2 f^2 w_0^2} + \frac{(f - d_2)^2 w_0^2}{f^2}}. \quad (\text{E.6})$$

E.2 Blur of CCD image due to an extended source region

Due to the finite size of the pinhole, the observed synchrotron light at the CCD chip originates from an extended region as illustrated in figure E.1. According to the figure, the length of the source region is approximately

$$L = \rho \theta \approx \rho(2r_p/d_0 + 2\sigma_\theta), \quad (\text{E.7})$$

where ρ is the bending radius of the beam trajectory, r_p is the radius of the pinhole, and σ_θ is the divergence of the synchrotron light cone (one standard deviation), including both the inherent divergence of the synchrotron light as well as the divergence of the electron beam.

As a result of the finite size of the source, the ends of the source region are slightly out of focus resulting in a finite resolution of the CCD image with an approximate magnitude of

$$\sigma_{res,1} = \left| L/2 \frac{dd_f}{dd_0} \frac{r_p}{d_f} \right| = L/2 \frac{f^2}{(d_0 + d_1 - f)^2} \frac{r_p}{d_f}, \quad (\text{E.8})$$

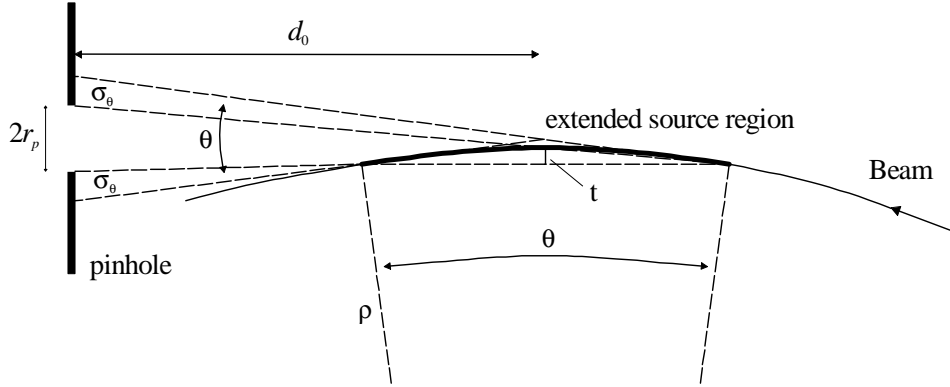


Figure E.1: Schematic of the extended source region from which the observed synchrotron light originates.

Analysis of the synchrotron light imaging system

where d_f is the distance from the lens to the focus and the relation $1/(d_0+d_1)+1/d_f=1/f$ from geometrical optics has been used. In addition, the horizontal width of the source region gives rise to a finite horizontal resolution of the CCD image which according to figure E.1 approximately is

$$\begin{aligned}\sigma_{res,2} &= \frac{1}{2}t \frac{d_f}{d_0+d_1} = \frac{1}{2}\rho(1-\cos(\theta/2)) \frac{d_f}{d_0+d_1} \\ &\approx \frac{1}{2}\rho(r_p/d_0 + \sigma_\theta)^2 \frac{d_f}{d_0+d_1} \quad ,\end{aligned}\tag{E.9}$$

where the factor $d_f/(d_0+d_1)$ accounts for the transformation from the object plane to the image plane.

References:

- [1] P. W. Milonni and J. H. Eberly, *Lasers*, John Wiley & Sons, New York, 1998, Chap. 14